UiT Norges arktiske universitet

FACULTY OF SCIENCE AND TECHNOLOGY

Department of Geoscience

Characterizing slope processes along the Piggtind mountain ridge, using 2D InSAR

Henrik Sandbakken

Master's thesis in Geology, GEO-3900, May 2021

Cover photo from Piggtind by Martina Böhme.

Abstract

Large rock slope deformations potentially evolving into catastrophic rock avalanches pose an eminent threat to the Norwegian society. A comprehensive characterization of their kinematic behavior, progressive slope development, and current deformation rates are thus required for hazard management. Njunnás and Piggtind/Skulvatindane are two adjacent rock slopes located in Troms County, Norway. Both slopes show morphological features diagnostic for rock slope deformations (RSD) and are, therefore, inventoried as unstable mountains by Geological Survey of Norway (NGU). However, a satisfying understanding of the RSDs are currently lacking. On Piggtind/Skulvatindane, the complex deformation morphology including substantial disintegration of rock and the high presence of superficial and periglacial slope processes partially obscure the deeper rock slope deformation. Hence, accomplishing a robust characterization of the RSD is not trivial and requires a detailed categorization of the slope processes.

In this study, two-dimensional satellite Interferometric Synthetic Aperture Radar (2D InSAR) is integrated with geomorphological- and structural investigations. By combining overlapping InSAR data obtained from both ascending and descending acquisition geometries, 2D InSAR surface displacements are estimated, allowing for quantification of all components of the displacement in the vertical E-W plane (horizontal, vertical, combined 2D velocity, and dip of combined 2D velocity vector). The 2D InSAR results and geological interpretations are displayed on maps and plotted along topographic profiles, allowing for detailed visualization.

Longitudinal variations in velocity and dip of combined 2D velocity vectors highlight a sliding-motion parallel to measured foliation on Njunnás, suggesting that the pre-existing, moderately inclined foliation planes are utilized as the basal rupture surface. A marked reduction in the dip of the combined 2D velocity vectors and increased brittle fracturing is observed in the lower sections of both RSDs, indicating an abrupt transition to a low-inclined basal rupture surface. Hence, both RSDs are classified as compound bi-planar slides. The RSD at Njunnás is interpreted to deform as a coherent single body due to the detected homogeneous 2D InSAR displacement rates in the order of 2–3 mm/yr. Contrary, the RSD at Piggtind/Skulvatindane generally exhibits displacement rates around 10 mm/yr but comprises large spatial variability of differential velocity. Clusters of high velocity (up to 157 mm/yr) have been interpreted to

predominantly correspond to displacement of superficial mass-wasting deposits, solifluction features, and a multi-lobate rock glacier complex superimposed on the RSD.

These results highlight the advantage of characterizing RSDs and identifying superficial slope processes with a multidisciplinary approach, combining structural geology, geomorphology, and satellite remote sensing. The utilized approach is readily applicable to other RSDs when well covered with two complementary InSAR geometries and can be exploited to attribute a failure mechanism and state-of-activity to all inventoried RSDs at a regional or national scale.

Acknowledgements

I would like to thank my supervisor at the University of Tromsø (UiT), Anne Hormes, for valuable guidance and educational days in the field. I really appreciate the feedback you have given me. I am also grateful for the patience and amount of time my co-supervisors Line Rouyet and Tom Rune Lauknes at the Norwegian Research Center (NORCE) have put into my thesis. You have truly inspired me and guided me through this exciting and challenging year. A special thanks to you, Line, for aiding me, motivating me, and sharing your knowledge.

Thanks to NORCE for letting me use their office (and coffee machine) and Jakob Grahn for helping me with the 2D InSAR software.

I would also like to thank Martina Böhme at the Geological Survey of Norway (NGU) for helpful feedback, a fun day in the field, and for sharing data with me.

Finally, I would like to thank Vilde, for being so patient and always encouraging me. Your positive energy and optimism have truly made this year easier.

Henrik Sandbakken
Tromsø, May 2021

Table of content

1 Introduction

1.1 Motivation

Steep valleys and fjords, mountainous topography, and a long coastline characterize the Norwegian scenery. This complex landscape has proven to be particularly prone for geohazards such as rockfalls and rock avalanches. Hundreds of inventoried unstable mountain parts experience rock slope deformation (RSD) that may evolve into catastrophic events in case of failure (Hermanns et al., 2012). Through time, catastrophic failures of RSDs have induced more than 175 fatalities in Norway and caused severe damage to settlements and infrastructure. The majority of casualties are related to the RSDs tsunamigenic potential, affecting coastal settlements far from the initiation area (Hermanns et al., 2013).

To mitigate hazards related to RSDs, public stakeholders such as the Geological Survey of Norway (NGU) and Norwegian Water Resources and Energy Directorate (NVE) are running a national campaign, which aims to identify, characterize and monitor RSDs (Hermanns et al., 2013; Bunkholt et al., 2013a). The required knowledge for assessing the hazard probability and the potential consequences of a catastrophic rock slope failure (risk) are usually obtained by in-field exploration, structural investigations, and evaluations of deformation rates obtained from in-field measuring techniques and/or remote sensing methods (Hermanns et al., 2012). Thanks to the open data policy of the Copernicus Sentinel-1 program, and the recent launch of the publicly available national ground motion mapping service, *InSAR Norway* (operated by NGU), the exploitation of satellite Interferometric Synthetic Aperture Radar (InSAR) for both detection and monitoring of RSD has intensified (Dehls et al., 2019; NGU, 2020d). After the launch in 2018, 100 new RSD have been identified in mainland Norway (Setså, 2021), highlighting the relevance of incorporating this tool in hazard analysis. However, displacement information available in *InSAR Norway* can be difficult to interpret for an end-user without any knowledge concerning InSAR properties and limitations, and the factors controlling the detected ground displacement. Single geometry InSAR dataset documenting the displacements projected along the radar line-of-sight (LOS) are not fully suited for a comprehensive analysis of kinematic behavior and progressive slope development (i.e., spatial extent and potential segmentation) of RSDs (Samsonov et al., 2020; Eriksen et al., 2017).

In 2020, NORCE developed a tool designed as a plugin for Geographic Information System (GIS), allowing for an efficient 2D InSAR calculation and visualization based on the data provided by *InSAR Norway*. The 2D InSAR method combines measurements from overlapping SAR geometries, allowing for detailed exploration of surface displacement in two dimensions (vertical, horizontal, and combined 2D velocity in the E-W plane). 2D displacement information has proven advantageous since it allows for a more comprehensive interpretation of the surface displacement patterns and requires less pre-knowledge on InSAR theory. Integrating 2D InSAR for evaluating the state of activity and kinematic behavior show great potential (Eriksen et al., 2017; Böhme et al., 2016; Crippa et al., 2021) and can be especially valuable when complemented by structural- and geomorphological investigations.

Njunnás and Piggtind/Skulvatindane are two adjacent mountain slopes located in central Troms, northern Norway. Both rock slopes are classified as RSDs by NGU; however, only basic investigations have been completed until now. Hence, a comprehensive understanding of the RSDs mechanisms in this area is at present date missing (Bunkholt et al., 2013b; Henderson et al., 2007). The incomplete understanding of the RSD on Piggtind/Skulvatindane can be attributed to the complex morphology and considerable disintegration of the rock. In addition, the high latitude of the site and the associated subarctic climate have favored the development and preservation of periglacial landforms such as solifluction features and rock glaciers. As a result, the mountain flank is extensively covered with multiple co-existing- and overlapping slope processes, potentially obscuring the deeper rock slope deformation. This limits the exploitation of traditional in-field investigations and adversely affects the interpretation of displacement information from InSAR, since it is difficult to determine the landform or process responsible for the surface displacement. Hence, it appears necessary to increase the understanding of the two RSDs by exploiting a multidisciplinary approach involving geomorphology, structural geology, and new, higher-order, 2D InSAR products. The presence of permafrost-dependent active rock glaciers on Piggtind/Skulvatindane also provides an opportunity to evaluate the applicability of 2D InSAR for characterizing, identifying, and delineating these fast-moving landforms. Rock glaciers kinematics, activity, and their spatial distribution are of great interest to the scientific community, as they provide valuable information concerning the present and past permafrost conditions (Sattler et al., 2016).

1.2 Objectives

The study's main aim is to combine a geological analysis, including investigations of geomorphological mapping and structural measurements, with a remote sensing analysis based on InSAR, to increase the understanding of the rock slope deformations on Njunnás and Piggtind/Skulvatindane. A multidisciplinary approach, especially emphasizing displacement information from 2D InSAR, will be utilized for interpreting the kinematic behavior and the progressive slope development of the RSDs, and for evaluating the spatial extent of the superficial slope processes. In addition, the thesis further aims to demonstrate 2D InSARs capabilities and limitations when applied on both fast (rock glaciers) and slow-moving (RSDs) landforms in a mountainous periglacial environment.

To successfully accomplish the aims of the study, the following objectives are defined:

I. Produce detailed morpho-gravitational maps and categorize the superficial land cover based on field investigations and available map resources.
II. Generate 2D InSAR displacement maps and relate displacement to specific landforms and structures based on existing inventories/maps or produced maps.
III. Exploit 2D InSAR and geomorphological- and structural observations for creating comprehensive cross-sections and interpreting slope processes in the study area.
IV. Interpret the basal rupture surfaces based on a rock slope stability assessment using kinematic analysis (with software *Dips8*) and surface displacement patterns observed with 2D InSAR.

1.3 Thesis Structure

This thesis comprises eight Chapters (excluding appendix and references). A theoretical introduction to the topics "Satellite InSAR" and "Slope processes" is given in Chapter 2. The setting of the study area, from a geological perspective, is presented in Chapter 3. The exploited methods and data are listed and explained in Chapter 4. Chapter 5 and 6 presents the results from Njunnás and Piggtind/Skulvatindane, respectively. Considering that the thesis deals with two separate localities, it is viewed as beneficial to interpret and discussed the results consecutively. Chapter 7 discuss co-jointly the results for both areas and highlight the potential and limitations of the exploited methods. The relevance of the study and the transferability of the findings and utilized method to other areas, is also discussed. Finally, I conclude by shortly summarizing the main findings from both localities in Chapter 8.

2 Theoretical background

The following chapter introduces the theoretical background considered necessary for successfully accomplish the aims of the study. Short presentations of the topics satellite Synthetic Aperture Radar (SAR) and SAR Interferometry (InSAR) are given in Subchapter 2.1. The various slope processes investigated in this thesis, including rock slope deformations (RSD), rock glaciers, and solifluction features, are defined, and the characteristic displacement behavior is described in Subchapter 2.2.

2.1 Satellite InSAR

2.1.1 Synthetic Aperture Radar imaging

Synthetic Aperture Radar (SAR) is a space-borne active imaging technique that allows for detecting surface deformation (Ferretti, 2013). Electromagnetic waves are transmitted from an active sensor as microwave pulses. These pulses are then reflected as they reach the Earth's surface, and the scattered signals are recorded by a receive antenna. The amplitude- and phase component of this backscattered signal is then analyzed and contains information about the distance between the sensor and the target (phase) along the radar line-of-sight (LOS) and the reflectivity of the target (amplitude). The sensor-target distance is expressed by a given number of wavelengths (λ) in addition to a fraction of a wavelength (phase φ). (Lauknes, 2010).

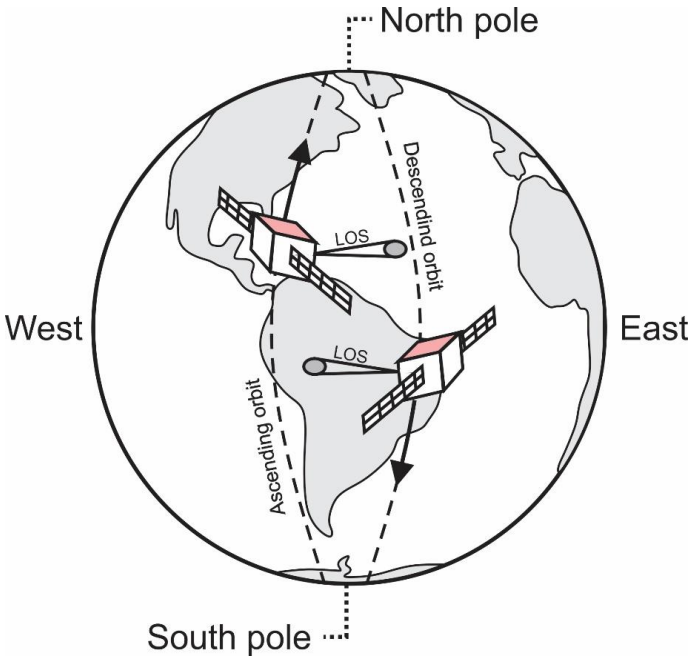

Figure 2.1: Geometry of ascending and descending satellite orbits. The figure shows two satellites moving in opposite directions. The LOS direction is displayed for right-looking satellites. Inspired by Ferretti (2013) and Lauknes (2010).

The satellite SAR instrument travel in an approximately polar orbit (from pole to pole). Consequently, the satellite travels from the south pole to the north pole (ascending pass) and then from the north pole to the south

pole (descending pass) (Fig. 2.1). The size of the illuminated ground swath for Sentinel-1 is approximately 250 km wide, and the angle between the radar LOS vector and the vertical plane is entitled the "incidence angle", and will vary within the swath (Fig. 2.3) (NGU, 2020d).

SAR geometrical considerations

Since the SAR instrument illuminates the surface with a constrained direction, significant discrepancies in the topography may cause a loss of information from certain areas (Barboux et al., 2014). Shadowing occurs when obstacles such as steep cliffs face away from the satellite (Fig. 2.2). The incidence angle controls the size of this shade; a steeper angle will reduce the shadow effect (Barboux et al., 2014). In addition, when evaluating mountainous regions, foreshortening can appear on slopes facing towards the satellite. The imaged terrain will appear shortened, i.e., the pixels are compressed, and consequently, the resolution is adversely affected (Lauknes, 2010). Therefore, it is beneficial to select slopes facing away from the radar (Rouyet et al., 2015). In the cases where ridges/summits are imaged together with the base of the mountain, layover may occur. The received signal from reflectors with a considerably altitudinal difference will be mapped into the same pixel, resulting in ambiguous radar return (Lauknes, 2010).

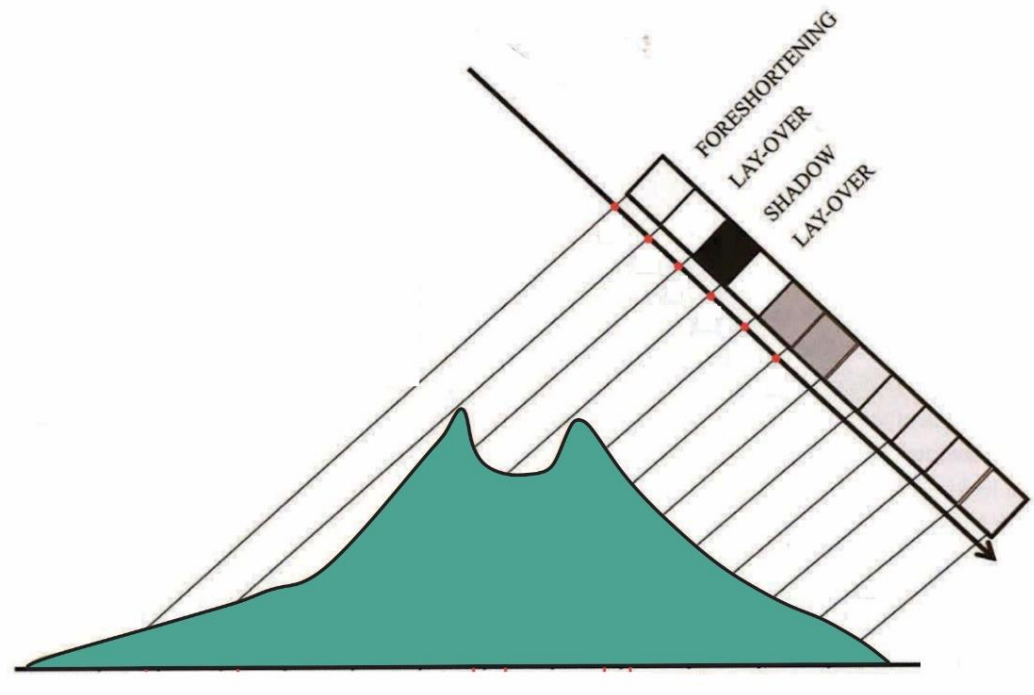

Figure 2.2: Geometrical distortions in a SAR image. Modified from Ferretti (2013).

2.1.2 SAR Interferometry (InSAR)

The phase information obtained from one single SAR acquisition is inadequate for evaluating surface displacement. Such information has no direct use since the values will be uniformly distributed between 0–360° (Rouyet et al., 2015). However, when phase information from two disparate temporal acquisitions is compared, one can create an interferogram showing the difference in phase. By exploiting this technique (termed interferometry), one can successfully deduce the surface displacement along radar LOS (Fig. 2.3) (Ferretti, 2013). InSAR is commonly exploited in a variety of scientific studies, including urban subsidence (Songbo et al., 2020), rock glacier kinematics (Liu et al., 2013), landslides (Lauknes et al., 2010), seasonal dynamics of permafrost landscapes (Rouyet et al., 2019) and volcanic activity (Massonnet et al., 1993).

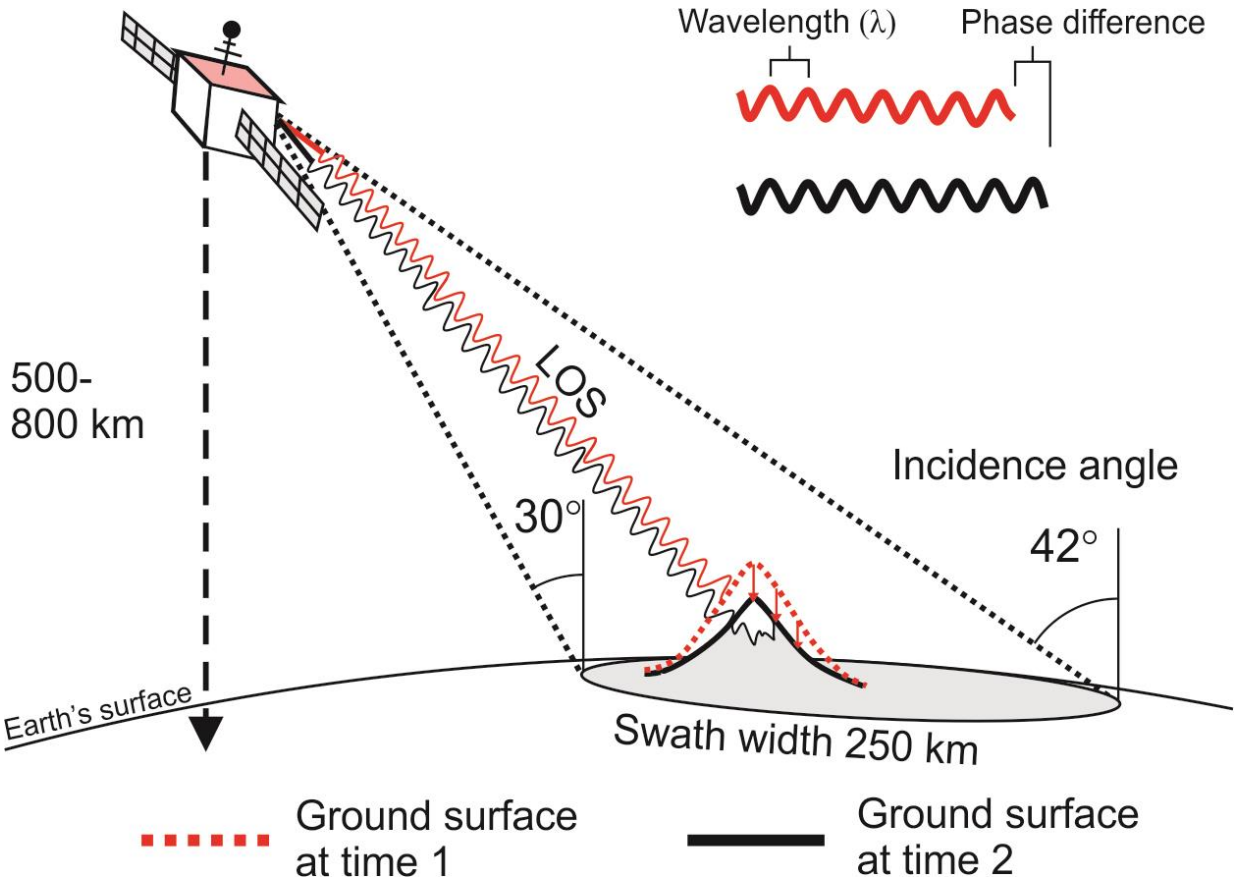

Figure 2.3: Sketch showing subsiding mountain and detected phase difference. A coherent radar pulse is transmitted towards the earth surface and reflected at time 1 (red) and 2 (black). The phase difference between the two separate temporal acquisitions are utilized to estimate the ground displacement along LOS. Inspired by Songbo et al. (2020), Lauknes (2010) and NGU (2020d)

InSAR limitations and considerations

Space-born SAR instruments, following a near-polar orbit, have a side-looking geometry that allows them to illuminate areas roughly towards the east and west. Commonly, they are right-looking, meaning that ascending satellites generally have a LOS directed towards east/northeast while descending towards west/northwest (denoted in degrees and termed azimuth angle) (Fig. 2.1) (Ferretti, 2013). Since InSAR-detected displacement corresponds to phase differences observed along radar LOS (Fig. 2.3), the SAR-equipped satellites can only detect displacement predominantly in the E-W plane. Hence, the sensitivity to detect displacement in the N-S plane is close to zero (Eriksen, 2017). Furthermore, this constrained detection capacity means that only the LOS parallel component of the three-dimensional surface displacement can be detected (Barboux et al., 2014).

The phase accuracy in SAR interferometry is influenced by decorrelation and phase noise. Decorrelation includes SAR imaging geometric effects and temporal backscattering changes (temporal decorrelation). Temporal decorrelation is related to substantial changes in electrical or geometrical properties of the reflectors within one pixel, between consecutive acquisitions, and may be caused by changes in vegetation, snow, or water (Ferretti, 2013; Eriksen, 2017). Hence, the ability to exploit InSAR in highly vegetated areas is minimal, and displacement information can only be retrieved from the snow-free season, which typically is June–October. In addition, when evaluating slope processes capable of reaching high displacement rates, phase decorrelation may adversely affect phase accuracy, resulting in little or no displacement information. This is typically expected for fast-moving rock glaciers. (Strozzi et al., 2005). To mitigate limitations connected to geometric and temporal decorrelation, multiple advanced InSAR time series methods have been developed to improve InSAR (Ferretti, 2013). One commonly utilized method is Persistent Scatterer Interferometry (PSI). The PSI method exploits a stack of interferograms, all generated with the same master image. The PSI algorithm searches for pixels that contain a dominating persistent scatterer (PS), with a consistent backscatter over time. The final product is a network of persistent scatterers with time series of deformation (Ferretti et al., 2001).

2.1.3 InSAR for slope movement

Mountainous regions in periglacial environments are constantly shaped by multiple geomorphic processes, such as permafrost creep, solifluction, rockfalls, rock glaciers, and landslides (Rouyet et al., under review; Imaizumi et al., 2018). Each process exhibits specific

characteristic morphological surface expression and a distinct kinematic pattern with spatial- and temporal variations. Traditionally, such slope processes are recognized and evaluated by geomorphological mapping based on interpretations of aerial images, LiDAR (light detection and ranging), and field investigations (Imaizumi et al., 2018). However, such methods are time-consuming, expensive, and have limited spatial coverage. Mapping and inventorying of various slope processes in alpine regions is regarded as an ever-increasing important task, both in the context of hazard management but also for understanding climate changes (Barboux et al., 2015).

During the last decades, InSAR has progressively been incorporated in Norway as an available tool for the detection and inventory of various slope processes such as landslides (Lauknes et al., 2010; Henderson et al., 2011), rock glaciers (Kääb et al., 2005; Eriksen et al., 2018; Barboux et al., 2015; Wang et al., 2017) and solifluction (Eriksen et al., 2017; Eckerstorfer et al., 2018; Rouyet et al., 2019; Eriksen, 2013). This kinematical approach has proven to be advantageous, as it is capable of covering large areas and distinguishes active landforms (moving) from inactive landforms (not moving) (Wang et al., 2017). Furthermore, since InSAR exploits microwaves for detecting surface displacement, it is independent of changes in light- or weather conditions (Ferretti, 2013). Hence, displacement information will be retrieved consistently according to the specified revisit time of the satellite.

2.2 Slope processes

This section presents short reviews of different slope processes and associated geomorphological- and kinematic characteristics. More comprehensive treatments of the topics and terminologies can be found in Agliardi et al., (2001), French, (2007), and Matsuoka et al., (2001). I focus only on the essential elements that have a major significance in exploiting InSAR to interpret ground processes.

2.2.1 Rock slope failures

Definition rock slope failure

Rock slope deformation is a terminology used on large-scale gravity-driven mass movements that potentially encompass entire mountain flanks (Crosta et al., 2013; Hungr et al., 2014). Such phenomena evolve over very long periods (potentially >10 000 years) and are characterized by

a slow continuous (mm–cm/yr) deformation by viscoplastic behavior (Pánek & Klimes, 2016; Crosta et al., 2014). Typically, they display discontinuous or weakly expressed delimitations both laterally and in the lower ends and may reach thicknesses of 200–300 m (Pánek & Klimes, 2016; Crosta et al., 2013). RSDs may pose as a precursory sign of imminent slope failure (Hungr et al., 2014; Hermanns & Longva, 2012). However, such continuous creep deformation does not necessarily culminate in a sudden single event failure. Agliardi et al., (2001) highlighted that such phenomena often result in the development of rather localized secondary instabilities that potentially form smaller rock avalanches or rock falls.

Classification of rock slope failure types

During the initiation of a gradual failure process, bounding ruptures develop lateral, at the rear, and underneath the instability. Such rupture surfaces utilize pre-existing discontinuities (joints, faults, and foliation) or propagate by forming new fractures as the deformation progresses (Stead & Eberhardt, 2013). Commonly, the geometry of the basal rupture surface, which subsequently controls the kinematic behavior, constitutes the basis for a classification (Hermanns and Longva, 2012; Braathen et al., 2004). A selection of basal rupture surfaces facilitating sliding is displayed in Fig. 2.4.

The importance of identifying the geometry of the basal rupture surface is related to the different modes/mechanisms mobility and the possibility to assess the volume of the instability. As highlighted by Crippa et al., (2021), translational slides tend to be more unstable and prone to higher mobility than rotational slides. The figure additionally shows three different pre-existing structures utilized as the rear rupture surface: foliation plane- (Fig. 2.4a), fault plane- (Fig. 2.4b), and joint plane rear rupture (Fig. 2.4c) (terminology according to Vick et al., 2020).

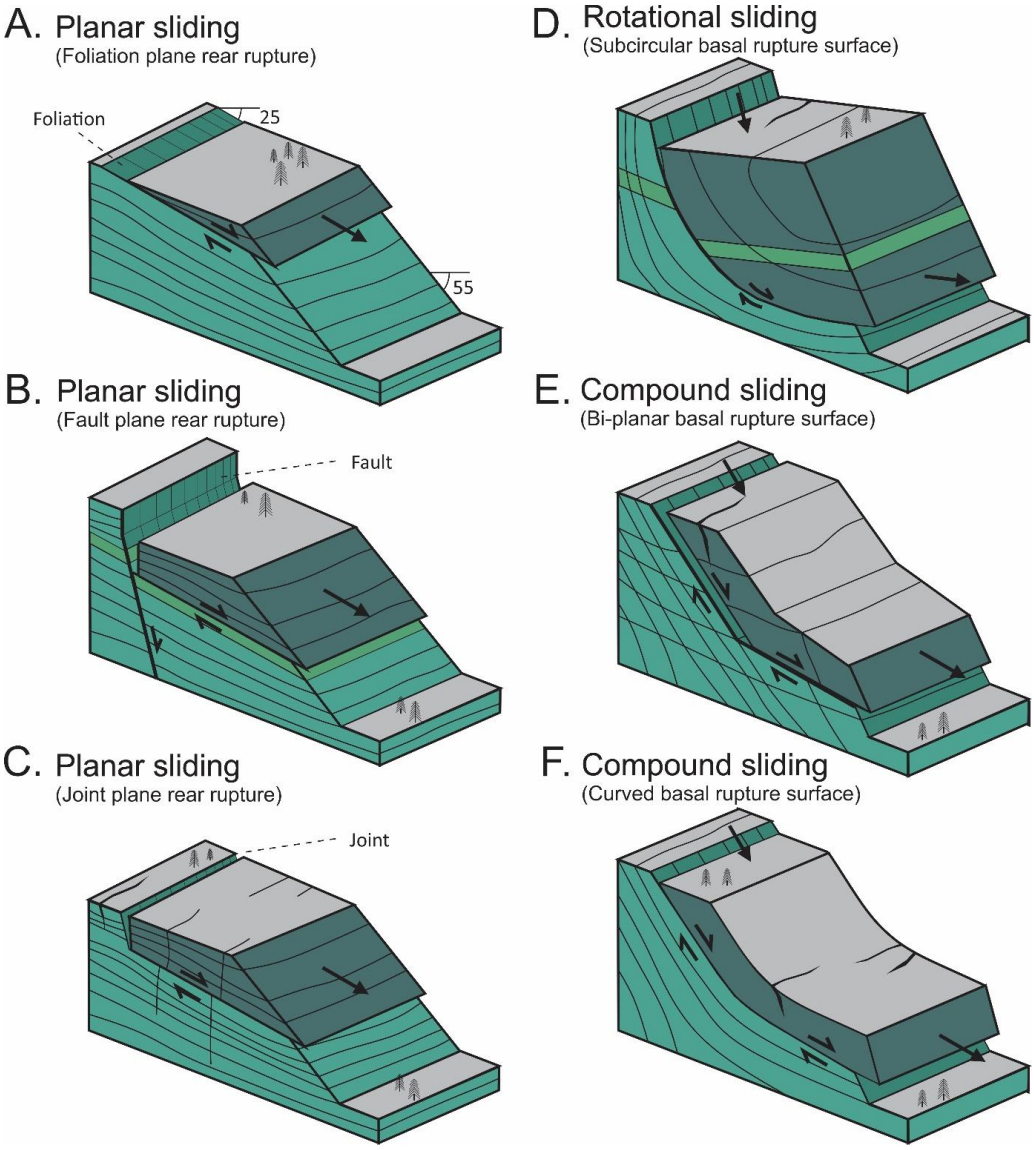

Figure 2.4: (A, B, and C) planar sliding (translational slides) with three different pre-existing structures creating the rear ruptures. (D) Sliding along a sub-circular failure surface (E) Sliding on two planar rupture surfaces with different inclination (compound sliding). (F) Compound sliding on basal rupture surface that becomes listric with depth (curved). Inspired by Vick et al. (2020) Wyllie & Mah (2004) and Hermanns & Longva (2012).

RSD kinematic pattern and displacement rates

Assessments of kinematic behavior (i.e., failure mechanism/mode) and progressive slope development (i.e., spatial extent and slab-formation/segmentation) of RSDs have conventionally been attained by traditional in-field methods such as geological mapping, geophysical surveys, and geodetic monitoring (Zangerl et al., 2019: Lauknes et al., 2010). However, such methods require ground contact, which can be problematic since many RSDs are located in harsh, dangerous environments (Gischig et al., 2011). Furthermore, geodetic monitoring, such as differential Global Navigation Satellite Systems (GNSS) and Total Station

measurements, provides displacement information very limited in space (Eriksen et al., 2017). Remote sensing techniques such as InSAR allow displacement information to be obtained with mm–cm precision from large inaccessible areas (Samsonov et al., 2020). In addition, as demonstrated by Rouyet et al., (2019), Eckerstorfer et al., (2018), and Eriksen et al., (2017) on various localities in Troms, the implementation of two-dimensional InSAR provides a robust tool for visualizing and describing deformation patterns.

RSDs commonly display some variations in velocity along a longitudinal swath. Such disparity may be the result of (1) heterogeneous material properties, (2) the existence of internal structures (scarps, faults, etc.) and/or secondary landslides, (3) geometry of the basal rupture surface (Frattini et al., 2018; Hermanns et al., 2012). In addition, when evaluating the kinematics of the RSD by the application of InSAR, one must acknowledge that changes in the direction of displacement with respect to the satellite's LOS may produce an apparent change in velocity (Frattini et al., 2018; Eriksen et al., 2017). Nonetheless, this statement indicates that it is possible to attain information about the geometry of the basal rupture surface if none of the other listed factors play a significant role in controlling the evolution of the landslide. (Frattini et al., 2018; Intrieri et al., 2020).

When evaluating deformation rates of an RSD in map view, it is possible to predict the extent of a possible failure scenario. Uniform distributed displacement rates throughout the whole deforming area may insinuate that the RSD moves as a homogeneous body. Hence, the slope failure is more likely to occur as one single event. Slopes that express nested sectors with differential velocity are potentially segmented into multiple slabs. These slabs may move independently and potentially by separate failure mechanisms. The failure of the slope can then either transpire as a synchronous failure of several slabs or as multiple repetitive events with a temporal difference (Zangerl et al., 2019; Hermanns et al., 2013; Crippa et al., 2021).

Morphostructures associated with RSDs and their function as kinematic indicators

As a response to a rock slope deformation, certain morphostructures develop (Hunger et al., 2014). They are commonly linear features following the orientation of the natural discontinuities (i.e., joints, foliation, faults, shear zones), or stratigraphic elements (i.e., lithological boundaries or weak rock) (Crosta et al., 2013). These structures reflect the magnitude of past displacement and provide valuable information about the extent of the deforming area (Agliardi et al., 2001)

Varying strain rates within an RSD give rise to different morphostructures. The Upper section/head domain is usually subjected to a mixed- or extensional stress regime, which typically produces scarps, counterscarps, double-ridges, trenches (open or infilled), horst and graben structures (Fig. 2.5) (Crosta et al., 2013; Agliardi et al., 2001). Such structures that emerge as a response to extension provide valid indications about the direction of movement. According to Fossen & Gabrielsen (2005), tensional fractures and scarps tend to develop perpendicular to the main stretching axis (σ1) and thus reveal the main direction of displacement.

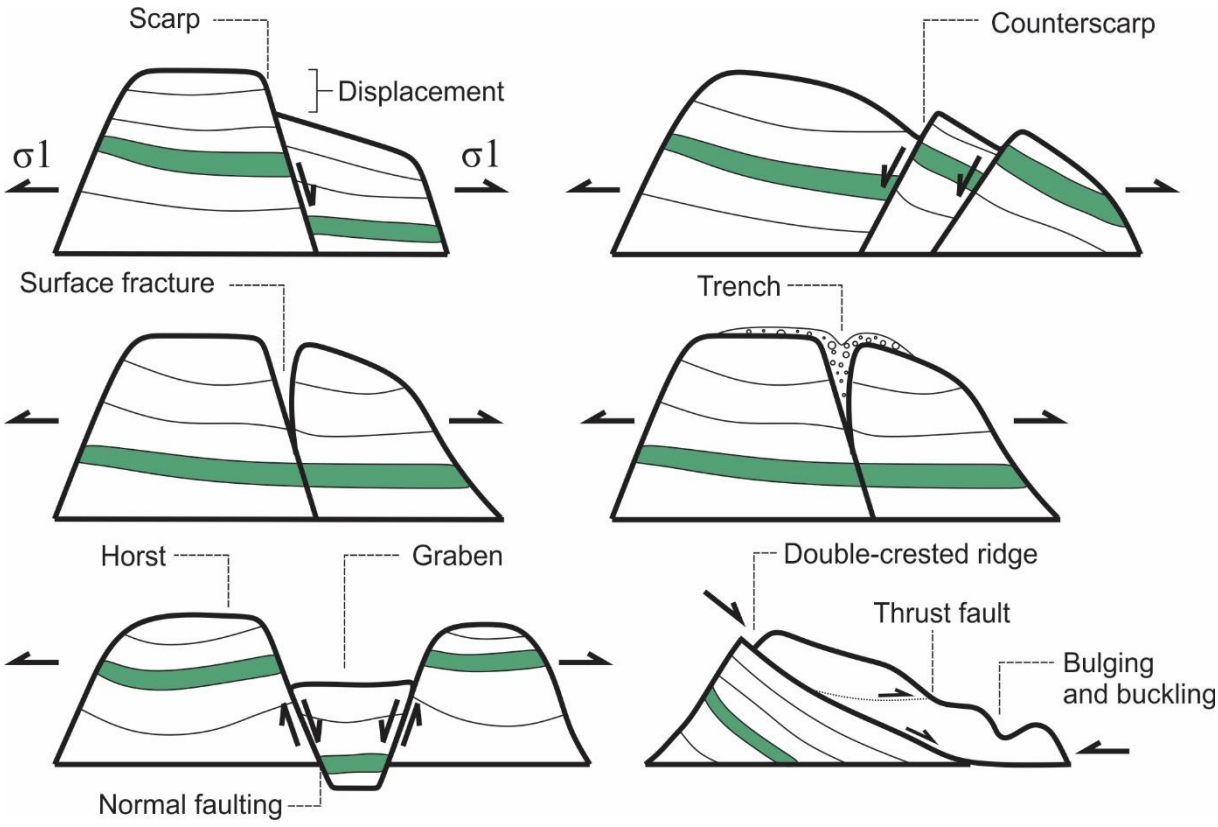

Figure 2.5: Morpho-gravitational structures typical for rock slope deformations. Inspired by Fossen & Gabrielsen (2005) and Agliardi et al. (2012)

The lower section/toe zone generally experiences a compressive stress regime, leading to the development of bulges, thrust faults, and highly disaggregated rock (Agliardi et al., 2012). Extensive bulging can potentially initiate secondary landslides since the steepness of the slope surface may become locally enhanced (Crosta et al., 2013). In mica-rich metamorphic rock, a stepped slope profile is additionally typical (Zangerl et al., 2019) since the mechanical weak rock easily deforms in a brittle-ductile manner.

RSDs in Troms

According to NGU, Troms and Finnmark is the county with the highest density of unstable rock slope deformations in Norway (NGU, 2020a). The majority of the RSDs are found in central Troms (clustered East of Lyngen and Storfjorden) (Fig. 2.6), which can to some extent be explained by the presence of metasedimentary rock and inherited structures from older deformation events. The medium-graded metamorphic rock, mica schist, is the dominating lithology in many RSDs (Vick et al., 2020; Rouyet et al., under review). It is characterized by low intact strength and is highly anisotropic, and thus facilitates instability. The rock is weakest when dipping between 20–40° (Zhang et al., 2011), which happens to coincide with the average dip of the nappes (Faber, 2017). Furthermore, the presence of weakness zones such as ductile shear zones or brittle faults may adversely affect the competence of the rock due to tectonic damage or potentially act as detachment planes (Vick et al., 2020). The steepness of the relief is recognized to be an essential factor in slope stability. However, since most of the RSDs in central Troms are located on moderate to steep slopes (20–35°), and seldom in slopes steeper than 60° (Vick et al., 2020; Bunkholt et al., 2013c), it cannot be assigned as a primary cause of the high spatial density. It should, however, be acknowledged as a significant contributing factor (Bunkholt et al., 2013c).

About 60% of all RSD in Troms are found on west-facing slopes (Rouyet et al., under review), which is thought to be explained by the overall nappe architecture and the orientation of major fault-systems (Bunkholt et al., 2013c; Vick et al., 2020; Rouyet et al., under review). Furthermore, as highlighted by Zangerl et al., (2019), the predominant failure mechanism for RSDs in mica-rich rock is compound slides.

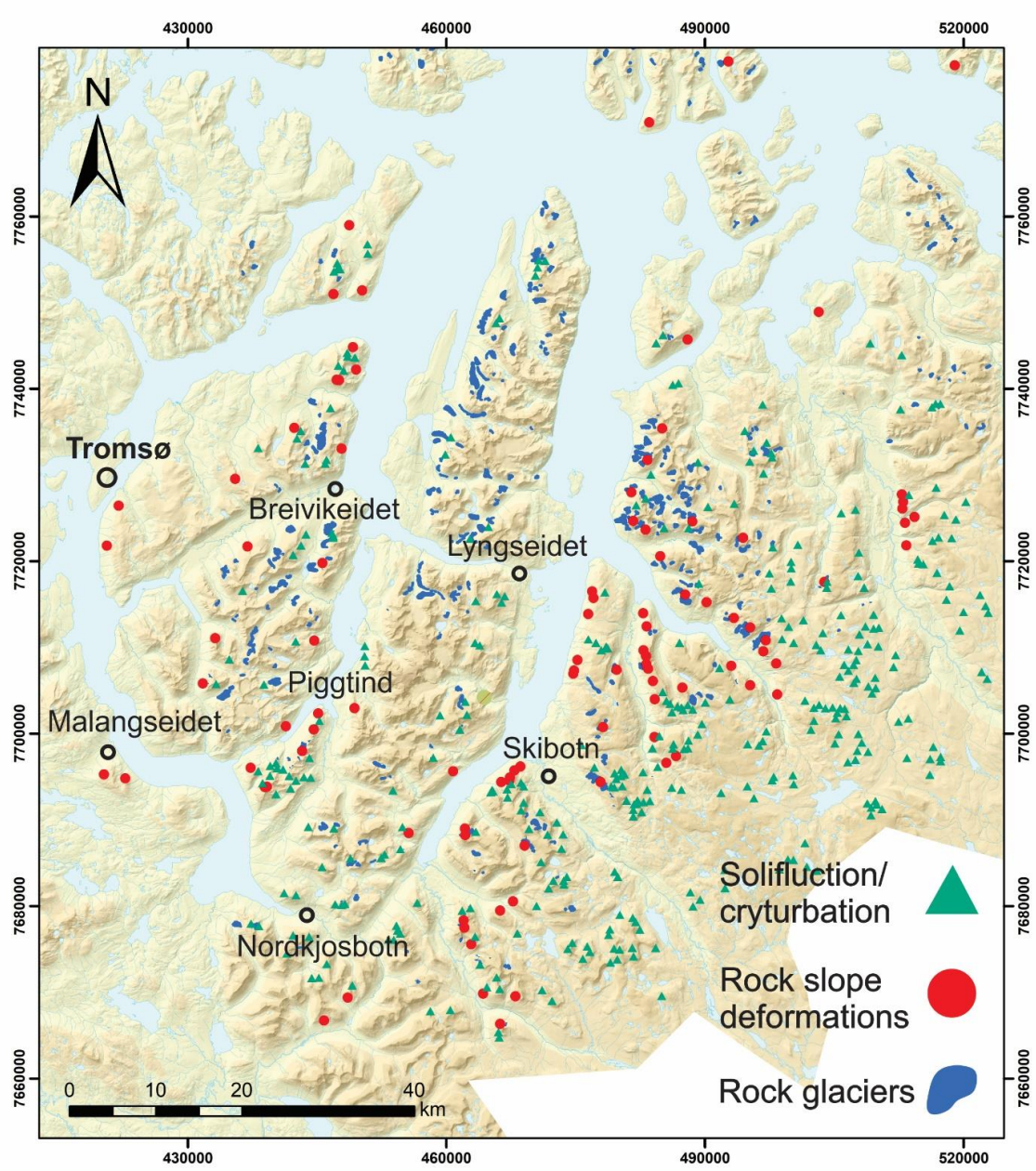

Figure 2.6: Relief map showing the spatial distribution of rock glacier, rock slope deformations, and solifluction features in Lyngen-Kåfjord area. The inventory is predominantly made by using InSAR but additionally aided by morphological investigations. Source data: periglacial landforms: Rouyet et al. (2021) (https://doi.pangaea.de/10.1594/PANGAEA.930856) and Lilleøren & Etzelmüller (2011) and rockslides NGU (2020a). Background map obtained from NMA (2020a)

2.2.2 Rock glaciers and permafrost

"Permafrost is defined on the basis of temperature: it is ground (i.e., soil and/or rock) that remains at or below 0 °C for at least two consecutive years" (French, 2007, p. 83). The uppermost layer of the soil, called the active layer, freezes during winter but thaws during summer. Thus, it cannot be classified as permafrost after the thermal definition (Shur et al.,

2005). This layer is affected by the seasonal and diurnal temperature changes and experienced cm-scale subsidence and heave connected to the water-ice phase changes (Harris et al., 2011).

Permafrost being a thermal-defined phenomenon, is not necessarily visible on the surface (Gisnås et al., 2017). However, it may give rise to certain landforms, either associated with permafrost aggregation or degradation (French, 2007). In Norway, rock glaciers are the most widespread permafrost-related landform (Lilleøren & Etzelmüller, 2011).

Definition rock glacier

"A rock glacier is a lobate or tongue-shaped body of frozen debris, with interstitial ice and ice lenses, which moves down-slope or down-valley by deformation of the ice contained within it" (French, 2007, p. 129). Rock glaciers are commonly classified after the degree of movement, which is highly correlated to the ice content. Active (moving) and inactive rock glaciers (not moving) are located in areas with present-day permafrost. They consist of a mixture of ice and rock and have a characteristic surface expression with flow lines, ridges, furrows, and a steeply dipping front, indicating past or present displacement (Singh et al., 2011; Wang et al., 2017). Relict rock glaciers are located in areas with former permafrost. The ice matrix has melted, which has led to subsidence and thermokarst structures on the surface. Due to the lack of ice, they are no longer able to move; thus, the surface is often highly vegetated and covered with lichen (Lilleøren & Etzelmüller, 2011; Jones et al., 2019). Rock glaciers can also be classified after their origin: Talus-derived rock glaciers and moraine-derived rock glaciers. Talus-derived rock glaciers are located beneath a talus slope, and no ice is usually visible (French, 2007). Occasionally, the term landslide-connected (a subordinate type of talus-derived) is applied to emphasize a spatial connection to an RSD, rock- or debris slide (IPA, 2020). The lower altitudinal limit (LAL) of active talus-derived rock glaciers are thought to coincide with the LAL for discontinuous/sporadic permafrost (Humlum et al., 1998; Wang et al., 2017; Sattler et al., 2016).

Rock glacier kinematic pattern and displacement rates

Because active rock glaciers are confined to areas with permafrost, they subsequently provide indications about the state of permafrost, which is valuable in assessing climate changes (Sattler et al., 2016; Strozzi et al., 2020). However, such evaluation can only be achieved if active landforms can be distinguished from inactive and relict. The assessment of kinematic status is traditionally obtained by in-field investigations of geomorphological features, examination of

optical images, and terrestrial geodetic measuring techniques (Wang et al., 2017; Eriksen et al., 2018). However, such methods are strenuous and time-consuming when utilized on regional or national studies, and therefore best suited for case studies.

The surface velocity on active rock glaciers usually is in the order of cm–m/yr (Singh et al., 2011; Eriksen et al., 2018; Rouyet et al., under review). The kinematic pattern resembles the flow of a glacier, with the highest velocities in the center and frontal part and a gradual decrease towards the initiation line (rear limit) and toward the lateral boundaries (Singh et al., 2011). The magnitude of the displacement is connected to temperature, water access, and topography (steepness) (Eriksen et al., 2018, Kääb et al., 2007), and the surface aspect essentially controls the displacement direction. However, as Eriksen et al., (2018) discovered on Ádjet, the displacement may also transpire along internal shear zones. Since the displacement is affected by climatic variables, temporal changes both long-term and annually are expected. Commonly, the velocities progressively increase throughout summer, culminating in early autumn. From there, the displacement rates decrease throughout late autumn- winter-early spring (Eriksen et al., 2018; Rouyet et al., 2019) (Fig. 2.7).

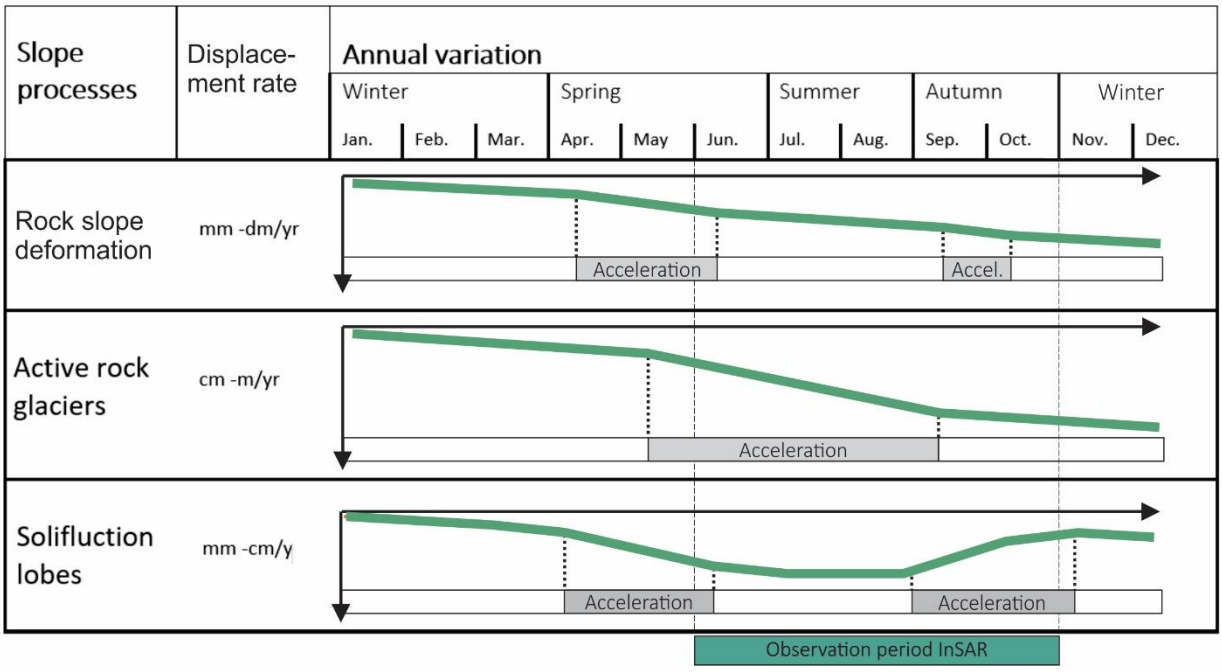

Figure 2.7: Annual variations in displacement rates for rock slope deformations, rock glaciers, and solifluction features. The figure highlights the approximate snow-free months where InSAR can be exploited for evaluating surface displacement.

Rock glaciers in Troms

Several studies aiming to identify and classify rock glaciers based on kinematics and origin have been conducted in Troms (Lilleøren & Etzelmüller, 2011; Hestad, 2019; Rouyet et al., under review). In total, 414 rock glacier units are identified in the Lyngen-Kåfjord area using InSAR and geomorphological mapping (Fig. 2.6). Approximately 22% are classified as active landforms, based on their present-day deformation behavior (Rouyet et al., under review). Most of the rock glaciers are talus-derived; however, a significant proportion is classified as the subordinate type; landslide-connected. The high spatial correlation between landslides and rock glaciers is suggested to be attributed to the landslides (including RSDs) creating environments favorable for the development and preservation of rock glaciers. Continuous supply of highly disintegrated rock is acknowledged as a major controlling factor for active rock glaciers and can serve as a feasible explanation for the frequently observed composite landforms (French, 2007; Rouyet et al., under review).

2.2.3 Solifluction

Definition solifluction

Solifluction is a collective name used for multiple processes associated with freeze and thaw action, resulting in slow superficial mass movement (Matsuoka et al., 2001). The movement is predominantly caused by frost creep and gelifluction working in tandem, causing a small down-slope displacement (Harris et al., 2008). This mass-wasting process and its associated landforms are found in areas subjected to a cold climate with sessional and diurnal freezing and thawing, and not exclusively confined to periglacial environments. Solifluction is easily recognizable on slopes with heterogeneous surface properties since varying topography prevents solifluction from operating uniformly, and results in a more channelized flow of the masses; Hence, the development of tongue-shaped lobes. On smooth surfaces with a low inclination, the solifluction operates uniformly, resulting in sheets of locally derived surface material. Such features may be difficult to identify (Matsuoka et al., 2001; French, 2007). High presence of vegetation generally adversely affects the development of solifluction, since the trees and shrubs reduce the freeze-thaw frequency by acting as a thermal insulator. In addition, vegetation tends to have a binding effect on the uppermost soil and thus prevent displacement (Matsuoka et al., 2001)

Solifluction kinematic patterns and displacement rates

Solifluction features typically move in the order of mm–cm/ yr (Harris et al., 2008; Matsuoka et al., 2001; Benedict, 1976; Eriksen et al., 2017; Rouyet et al., 2019). The surface velocity is usually highest just behind the lobe front and gradually decreases toward the rear of the lobe tread (Harris et al., 2008). Since this gravity-induced process also is related to freeze/thaw cycles (frost creep), there will be variations in the kinematics according to the observation period. In general, heave is expected in autumn and subsidence in spring/summer (Eriksen et al., 2017; Harris et al., 2011). During these periods, it is expected that the vertical component of the displacement is amplified and potentially exceeds the horizontal component (Rouyet et al., 2019). However, when evaluating mean annual displacement, the net displacement will be approximately slope parallel (Harris et al., 2008; French, 2007).

Solifluction in Troms

In Troms, solifluction features (sheets, lobes, and terraces) are most commonly found directly beneath the lower altitudinal limit for discontinuous permafrost, hence in areas with sporadic permafrost (usually above 500–800 m a.s.l.) (Rouyet et al., under review). However, as the development and preservation of solifluction features not necessarily depends on permafrost conditions, they do not serve as evidence of permafrost. A study from Kåfjord revealed that the ideal slope inclination was about 10–20° (Hjort et al., 2014), but solifluction is known to exist on slopes with considerably lower and higher inclination than that (Benedict, 1976). The high presence of mica schist is thought to contribute to the high spatial density of solifluction features in Troms (Fig. 2.6). The mechanical weak rock is especially prone to weathering and erosion, leading to a ground cover dominated by silt-rich diamicton, which is highly susceptible to frost action (Hjort et al., 2014). Recorded displacement rates from the region suggest that the velocity commonly is in the order of 0.3–10 mm/yr and 1–3 cm/yr (Rouyet et al., under review)

3 Study area

The selected localities are situated along the mountain ridge Piggtind in Troms and Finnmark county, northern Norway. Previous studies have identified and described three disparate RSD (Bunkholt et al., 2013b; Henderson et al., 2007) and multiple periglacial landforms, including rock glaciers and solifluction lobes (Rouyet et al., under review; Hestad, 2019; Lilleøren & Etzelmüller, 2011), along the west-facing mountain flank (Figs. 3.1 and 2.6). The present study focuses on the RSD at Njunnás and the periglacial landforms and RSD at Piggtind/Skulvatindane.

3.1 The setting of the study area

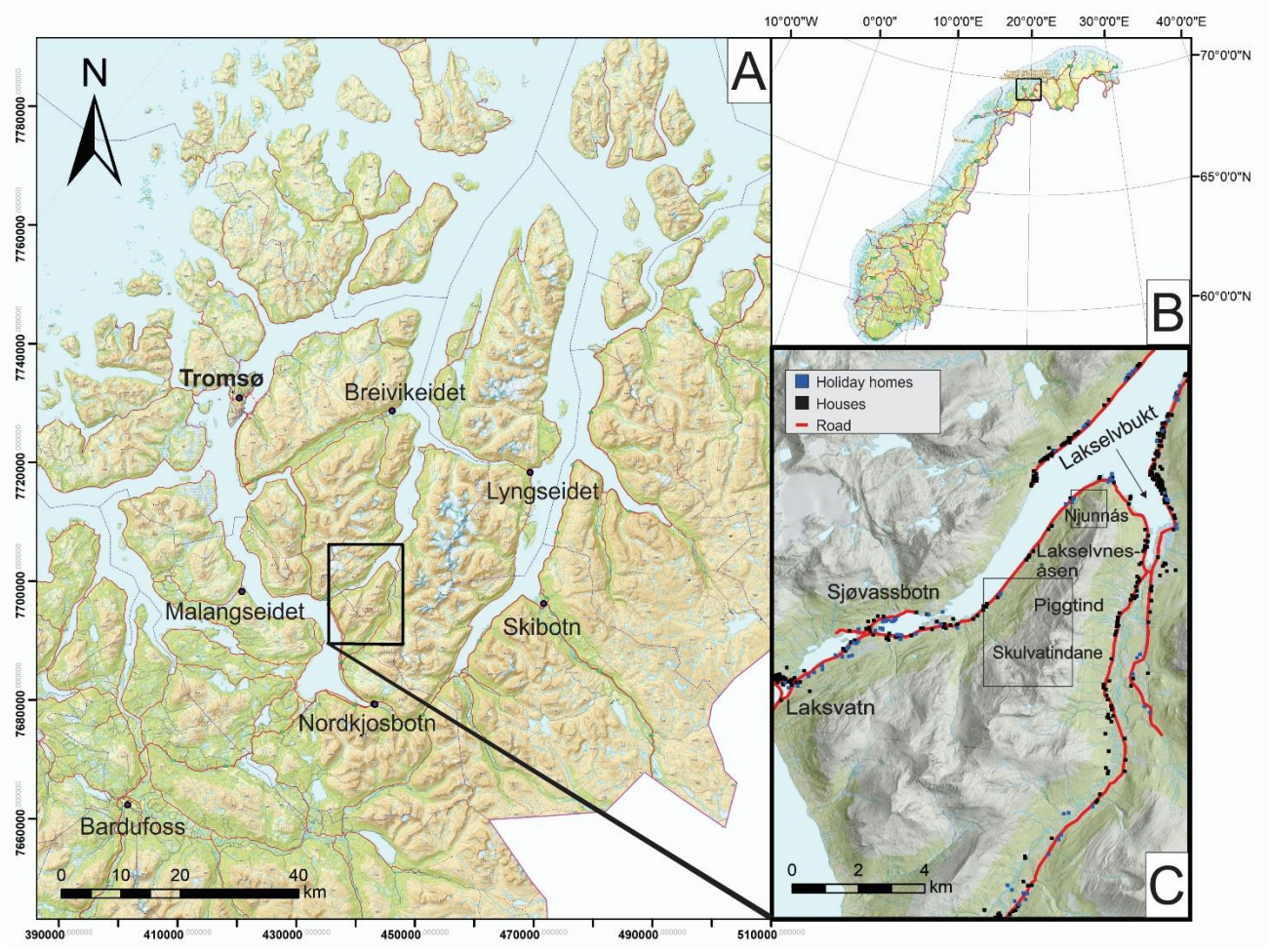

Figure 3.1: Topographic map showing the geographic location of Piggtind in Norway (B) and central Troms (A). Detailed relief map showing the location of municipalities and houses/holiday homes surrounding Piggtind. The picture extent used in the result chapters are displayed as black rectangles on Fig. C. Source maps*: NMA (2020a)*

Piggtind is a mountain ridge situated in Tromsø municipality, northern Norway (Fig. 3.1 a and b). The study area, which measures 9.14 km^2, is located furthest south on the Lyngen peninsula, enclosed by Sørfjorden to the west and Lakselvdalen valley to the east. The NNE-SSW-trending mountain ridge stretches from Njunnás in the north to Skulvatindane in the south (Fig. 3.1c) and ranges in elevation from 474–1062 m a.s.l. The entire western flank contains pronounced slope morpho-gravitational structures, diagnostic for RSDs. In addition, discontinuous/sporadic permafrost, and seasonal frost shape typical landforms, such as solifluction lobes and rock glaciers, are present (Fig. 2.6 and 3.2). The surrounding area is sparsely populated, with 151 people living at Lakselvbukt on the eastern side of Piggtind, 20 people living on the opposite side of Sørfjorden in Stordalstrand, and 51 people living at Sjøvassbotn at the end of Sørfjorden. However, about a dozen of the houses at Sjøvassbotn is located directly below the mountain slope of Piggtind (SSB, 2020).

Piggtind/Skulvatindane

Piggtind/Skulvatindane is the southernmost locality in the study area (Fig. 3.2). The valley flank falls on an average 25° towards WNW and is dominated by debris deposits and highly disintegrated rock related to fast-moving landslide processes and the rock slope deformation. The lower and middle section of the mountain slope is characterized by rounded morphostructures and an overall gentle inclination. The presence of vegetation is high in the lower section but gradually decreases before completely disappearing at 400–450 m a.s.l. Rockfall debris and hummocks dominate the ground cover in the middle section, and multiple solifluction lobes are visible from approximately >400 m a.s.l. The upper section displays the same characteristics as the middle section, containing rocks and boulders, but in dm–m scale. The slope inclination gradually increases before reaching scattered cliff bands in the uppermost section.

The locality is classified by NGU as an unstable rock slope, based on displacement rates observed with InSAR and the presence of morphostructures characteristic for RSDs (Henderson et al., 2007) (entitled Piggtind 1 by NGU). Field investigations were conducted in 2007 and 2013 by NGU. However, a satisfying understanding of the spatial extent, failure mechanism, and current deformation rates are missing. According to Rouyet et al., (under review), two active rock glaciers are identified with InSAR within the delimitations of the study area. A prominent rock glacier complex is located between the summits of Piggtind and Skulvatindane, and roughly covers an area of 0.5 km^2. The landform displays obvious morphological structures

characteristic for rock glaciers (discussed in Section 2.2.2) and displacement rates in the order of cm–dm/yr. Contrary, the second rock glacier, which is much smaller (0.05 km^2), lacks obvious morphostructures. However, the mean annual velocity is proportional. Both rock glaciers are inferred to be spatially connected to the RSD; Hence, classified as landslide-connected. Since the identification and delineations predominantly are based on kinematics observed with InSAR, and not field validated, the outer limits may be a little unprecise. Furthermore, since the extent of the RSD is unknown, the degree of spatial interconnection between the two landforms is unspecified.

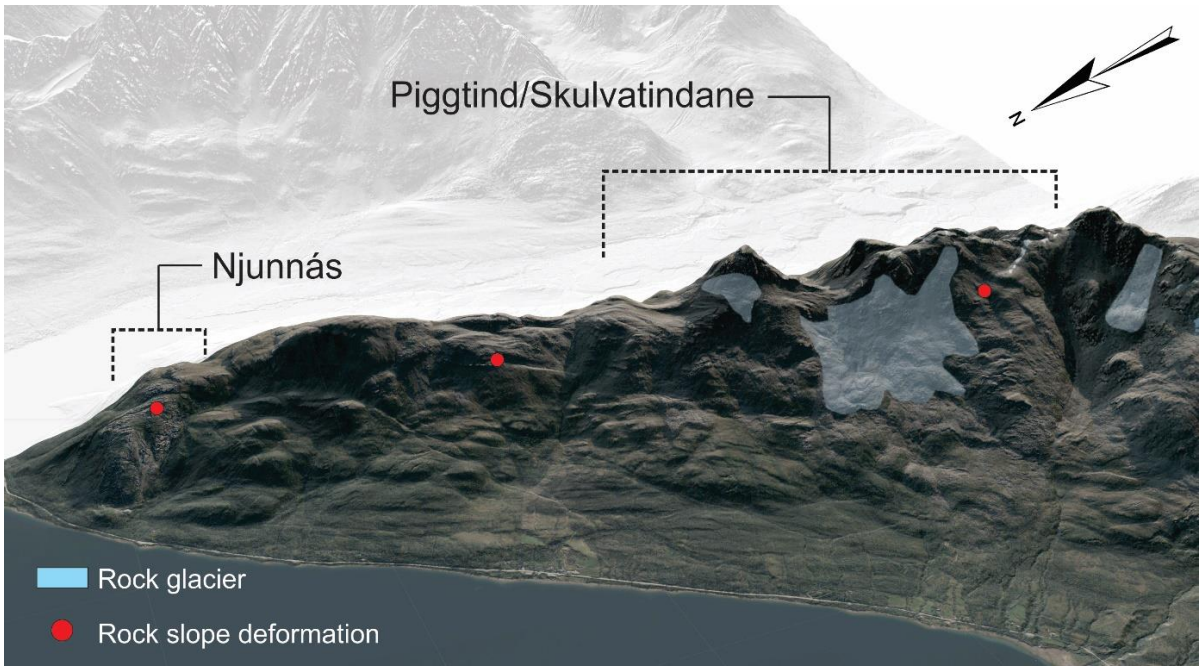

Figure 3.2: Three-dimensional view of Piggtind. Blue transparent polygons correspond to rock glaciers identified and mapped by means of InSAR (Rouyet et al., under review), while red dots represent rock slope deformations (NGU, 2020a). The width of the black dotted lines indicates the extent of the investigated areas included in this thesis. Source background: orthophoto NMA (2020c) draped on a DEM originating from NMA (2020b)

Njunnás

Njunnás is located furthest north on the ridge (Fig. 3.1c). It slopes down from the summit at 473 m a.s.l. to the fjord at an average of 24°. The locality protrudes from the surrounding landscape, having a convex-shaped topography with no vegetation (Fig. 3.2). Most of the locality consists of massive bedrock with only scattered patches of soil and debris deposits. This is in marked contrast to Piggtind/Skulvatindane, which is dominated by disintegrated rock and hummocks.

Njunnás is, according to NGU, classified as an RSD (entitled Piggtind 3 by NGU). Simple investigations involving field campaigns in 2012 and 2013 have been conducted on the locality. However, a comprehensive understanding of the RSD is lacking, and a more thorough risk assessment was therefore advised (Bunkholt et al., 2013b, p. 80-81). A potential rock avalanche may cause severe damage to the infrastructure (Fv. 7900) located immediately beneath Njunnás. Furthermore, a fast-moving landslide may initiate a tsunami wave, potentially hazardous for municipalities located along Sørfjorden.

3.2 Geological context

The following subchapter introduces the geological setting of the study area. Knowing the region's lithology, nappe architecture, post-Caledonian brittle structures, and deglaciation history are necessary for evaluating conditioning- and controlling factors for RSDs. However, as this is outside the scope of this study, the treatments of the topics will be cursory.

3.2.1 Regional geology

The bedrock lithologies in central Troms are part of the Caledonian nappe sequence. The Caledonian rocks are considered to be allochthonous and were emplaced on the Precambrian bedrock during the Caledonian orogeny (Bergh & Andresen, 1985). Piggtind is built up by the Lyngen nappe complex, located in the upper Allochthon (Ramberg et al., 2007). More precisely, the lithologies present at Piggtind originate from the Balsfjord group in the upper tectonic level (Andresen & Bergh 1985) (Fig. 3.3) and typically consist of an assembly of low-grade metamorphic rocks. The group predominantly comprises schists, conglomerates, and limestone/dolomite. The metamorphic grade varies within the group; however, a gradual increase is seen upwards in the nappe stack (Bergh &Andresen, 1985).

The dominating lithology in the study area is garnet chlorite mica schist, but the slightly decreased metamorphic equivalent phyllite is also present. According to the geological map presented in Fig. 3.4b, a band of quartzite crosscuts the slope, extending from Njunnás in the north to Rasmustinden in the south, where it abruptly stops. A thin band of quartzite is also exposed on the eastern side of Lakselvnesåsen but vanishes before reaching the summit of Piggtind. However, field observations in relation to this study suggest that the quartzite is not exclusively confined to the mapped bands. In several areas, minor quartzite bands are observed crosscutting both schists and phyllite. The mineral composition of the rock varies between mica-rich (muscovite and chlorite) and more quartz-rich. This alternating mineral composition

affects the physical properties of the rock and gives rise to layers and/or areas with more compact rock and more schistose rock.

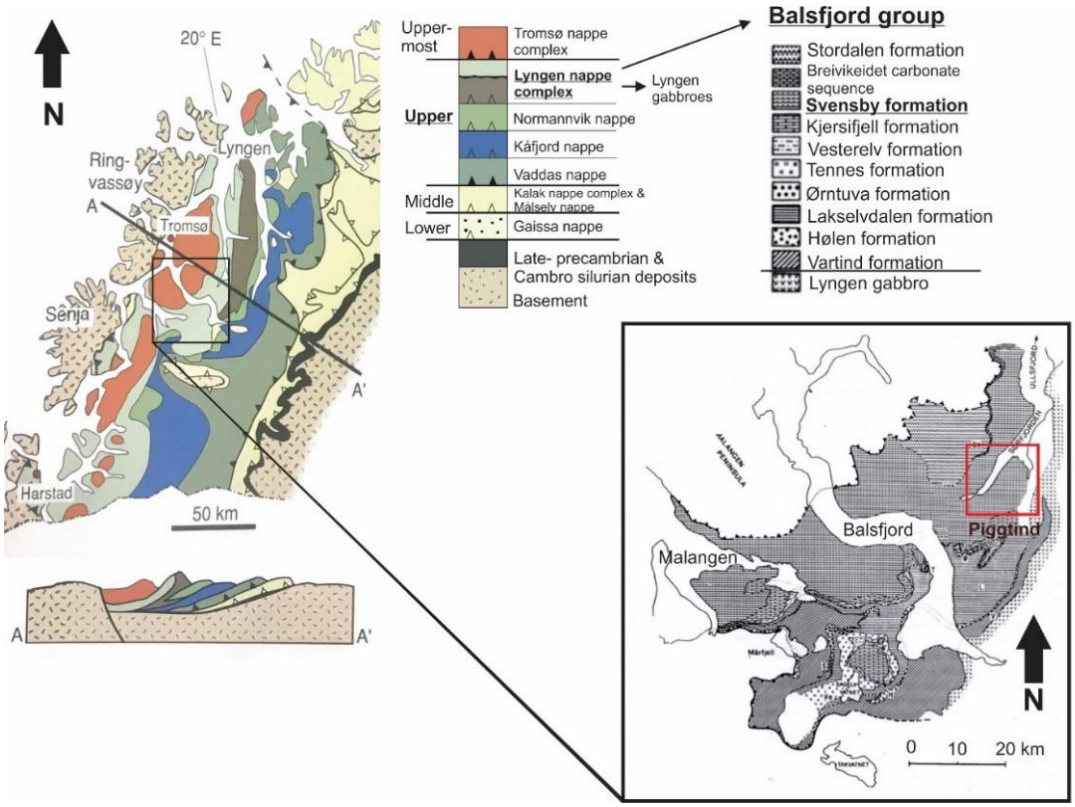

Figure 3.3: Overview of the Caledonian nappes present in Troms. Inset shows the spatial extent of the various lithological formations in the Balsfjord region. Modified after Ramberg et al. (2007) and Andresen & Bergh (1985).

3.2.2 Quaternary geology

In the context of rock slope deformations in periglacial environments, deglaciation history is regarded as an important conditioning factor (Hermanns et al., 2017;). This is related to oversteepening of valleys due to glacial erosion, debutressing, and stress release (Crosta et al., 2013; Agliardi et al., 2001).

According to Hughes et al., (2016), Piggtind became ice-free at approximately 14 ka (kilo annum). The past glaciations have draped Piggtind with glacial deposits, as testified by Fig. 3.4c. However, disparate patches of weathered material and marine shore deposits are additionally found in the slope's lower- and middle sections (NGU, 2020c). The presented Quaternary geological map of Piggtind (1:250 000, supplied by NGU) (Fig. 3.4c) is mainly based on aerial images and roadside observation, meaning the accuracy is potentially low and not validated by in-field observations. Indeed, this is evidenced by in-field investigations,

suggesting a significantly higher presence of mass-movement deposits (rockfall, rock avalanche, and disintegrated and disaggregated rock related to the RSD). Furthermore, glacial deposits are generally confined to the southern section and at low elevation.

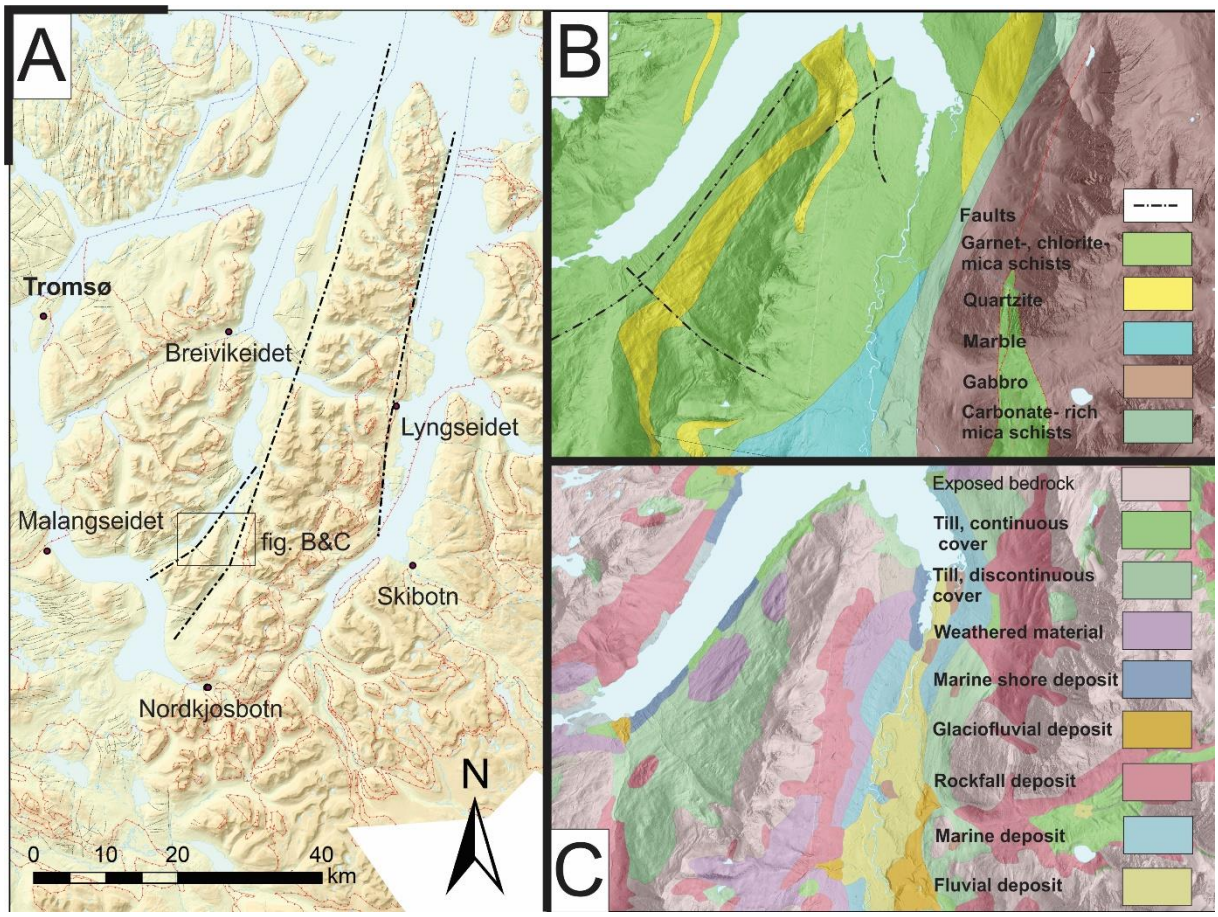

Figure 3.4: Relief map of central Troms, showing major faults bordering the Lyngen peninsula: Laksvatnet fault, western Lyngen fault, and Lyngen fault complex (eastern side of the peninsula) (A) (inspired by Vick et al., 2020). Bedrock map showing lithology's present at Piggtind (B) and a quaternary map showing sediment type by origin (C) (NGU, 2020c and NGU, 2020b).

3.2.3 Post Caledonian structures

Piggtind directly boarders Laksvatnet fault and western Lyngen fault (Fig.3.4a). In addition, smaller faults striking NW-SE and NE-SW are inferred to directly crosscut the locality (NGU, 2020b) (Fig. 3.4b). These post-Caledonian brittle structures are inferred to have developed during the rifting and basin formation of the Norwegian continental margin and are typically characterized by a sub-vertical to vertical dip (Bergh et al., 2007; Indrevær et al., 2014). The structures often provide the main directions for scarps and counterscarps in viscoplastic deformation and the opening of trenches due to tensile stress.

3.2.4 Climate

The climate in Troms is influenced by its far northern placement and is defined as subarctic. Long cold winters and short summers are characteristic of the subarctic climate. However, because of the proximity to the Norwegian Sea and the warm North Atlantic Current, the temperatures are slightly higher than expected. The climate varies, going from relatively warm and moist along the coast/ fjords to colder and dryer in Troms interior parts (Farbrot et al., 2013; Dyrrdal et al., 2020).

Piggtind is greatly affected by its immediate vicinity to the fjord, with an average winter temperature of -5.7° and a mean annual air temperature of -0.12°. About 6–7 out of 12 months have average temperatures below zero. However, 226 days have daily minimum temperatures below freezing, suggesting that sporadic frost nights occur during spring, summer, and autumn (Weather station at Lyngen-Gjerdvassbu 710 m a.s.l. in the time period 2012–2019). The first snow normally falls in October, and the snow cover lasts until May but varies depending on the altitude. The average precipitation is just above 900 mm, and 66% comes in months with average negative temperatures (weather station at Ytre Holmebukt (25 m a.s.l.) in the time period 2009–2019) (Meteorologisk Institutt, 2021).

3.2.5 Permafrost

Based on Piggtinds far latitudinal position (69.4°N), the lower altitudinal limit for intermittent permafrost could theoretically be at 400 m a.s.l. (Gisnås et al., 2017). However, the proximity to the coastline (60 km) and Sørfjorden is thought to greatly affect the altitudinal limit (Magnin et al., 2019; Farbrot et al., 2013), and thus, it could theoretically be as high as 1400 m a.s.l. (Gisnås et al., 2017). Hence, it is difficult to precisely predict the altitudinal position. However, both Magnin et al., 2019 and Farbrot et al., 2013, estimated a lower altitudinal limit of permafrost (LALP) at approximately 800–900 m a.s.l. in Lyngen-Kåfjord based on interpolated air- and ground temperatures (this stated limit corresponds to estimates for west-facing slopes in Magnin et al., (2019).

4 Data and methods

The following chapter presents a description of exploited data and methods considered necessary for solving the objectives presented in Section 1.2. The overall concept of the thesis is schematically presented in Fig. 4.1.

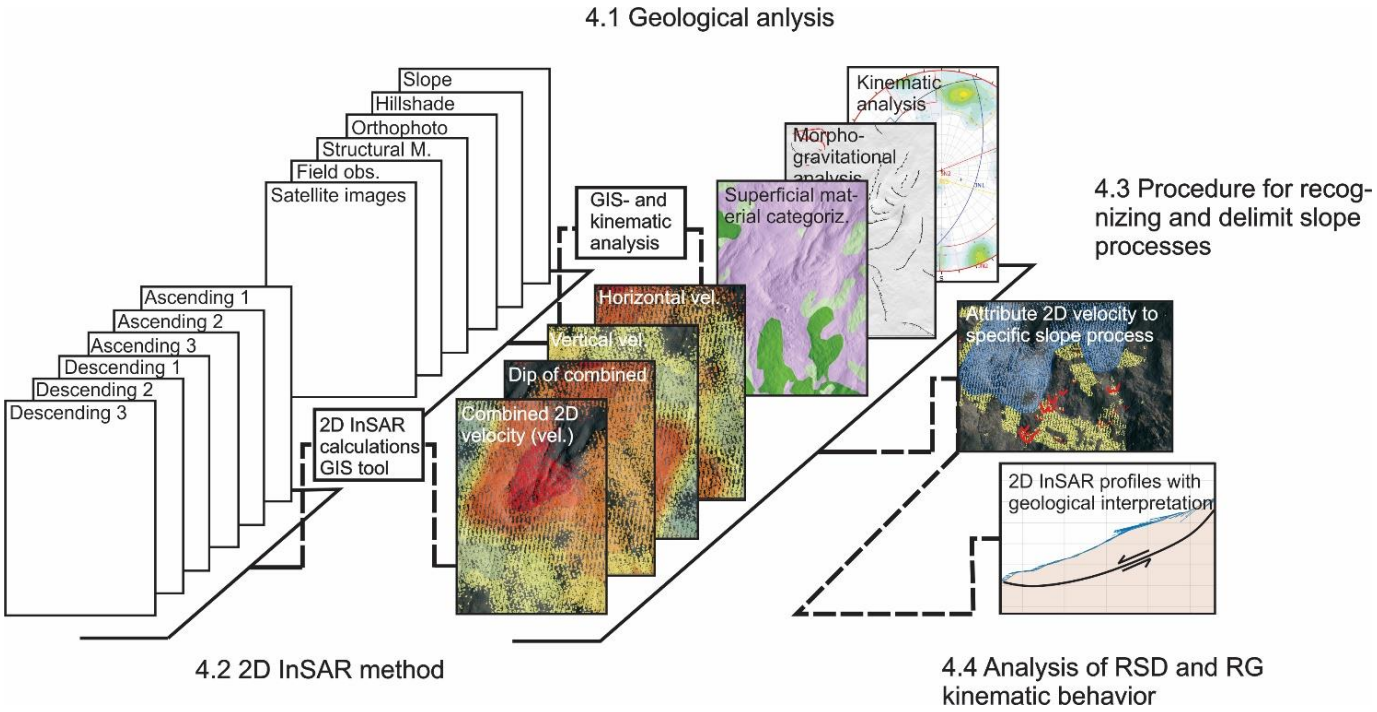

Figure 4.1: Methodical sketch showing the data utilized (left column) for creating the results (middle column) and further interpretation (right column).

4.1 InSAR

4.1.1 InSAR Norway

The public ground motion service *InSAR Norway,* which is based on the PSI method, was launched by the Geological Survey of Norway (NGU) in November 2018 (insar.ngu.no). Since then, the exploitation of this technique in the workflow of the public stakeholders (such as NVE and NGU) has intensified. The service is free of charge and open to all interested users (Dehls et al., 2019). The web portal allows for evaluating mean annual surface displacement on a national scale, predominantly from map-view, but temporal variations are additionally possible to assess with the time series function. The displacement information is obtained by two satellites, Sentinel-1A and B, with a combined revisit time of 6 days (NGU, 2020d) (Table 4.1). The service was developed to identify and periodically monitor slope instabilities and urban subsidence. However, it has additionally proven suitable for scientific studies of slope processes in high mountain regions (Dehls et al., 2019).

Table 4.1: Sensor parameters for Sentinel-1A and B.

	Band/ Wavelength (cm)	Incidence Angle (deg.)	Swath width (km)	Ground Range Resolution (m)	Azimuth Resolution (m)	Revisit Time (days)	Max. velocity mm/day
Sentinel-1A	C/5.55 cm	20–45°	80–400 km	5–25 m	5–40 m	12 days*	2.8/6
Sentinel-1B						12 days*	

**The two satellites Sentinel-1A and B, are working simultaneously. The revisit time by combining both satellites is, therefore, six days.*

The single geometries LOS InSAR datasets available on *InSAR Norway* originate from both ascending- and descending orbits (Fig.4.2). Since the Sentinel-1 satellites travel in a polar orbit, the satellite tracks gradually approach each other near the poles (Fig. 2.1), resulting in a large overlap between the SAR images. Areas located at high latitudes, such as Piggtind, take advantage of this and are able to obtain three datasets in both ascending- and descending geometry. This is a significant advantage since it allows for validating the quality of the separate datasets by comparison. Furthermore, since each dataset has its own unique LOS direction (incidence- and azimuth angle), it is possible to reduce the geometrical constraints by exploiting multiple datasets and identifying the one with the most favorable LOS compared to the slope geometry (NGU, 2020d).

Because of Norway's high latitudinal position and many mountainous regions, snow covers the ground from approximately November to May. Because snow adversely affects the phase accuracy, only SAR acquisitions from June-October are presented on *InSAR Norway* (NGU, 2020d). However, to compute the mean annual displacement, SAR pairs with long temporal intervals are integrated.

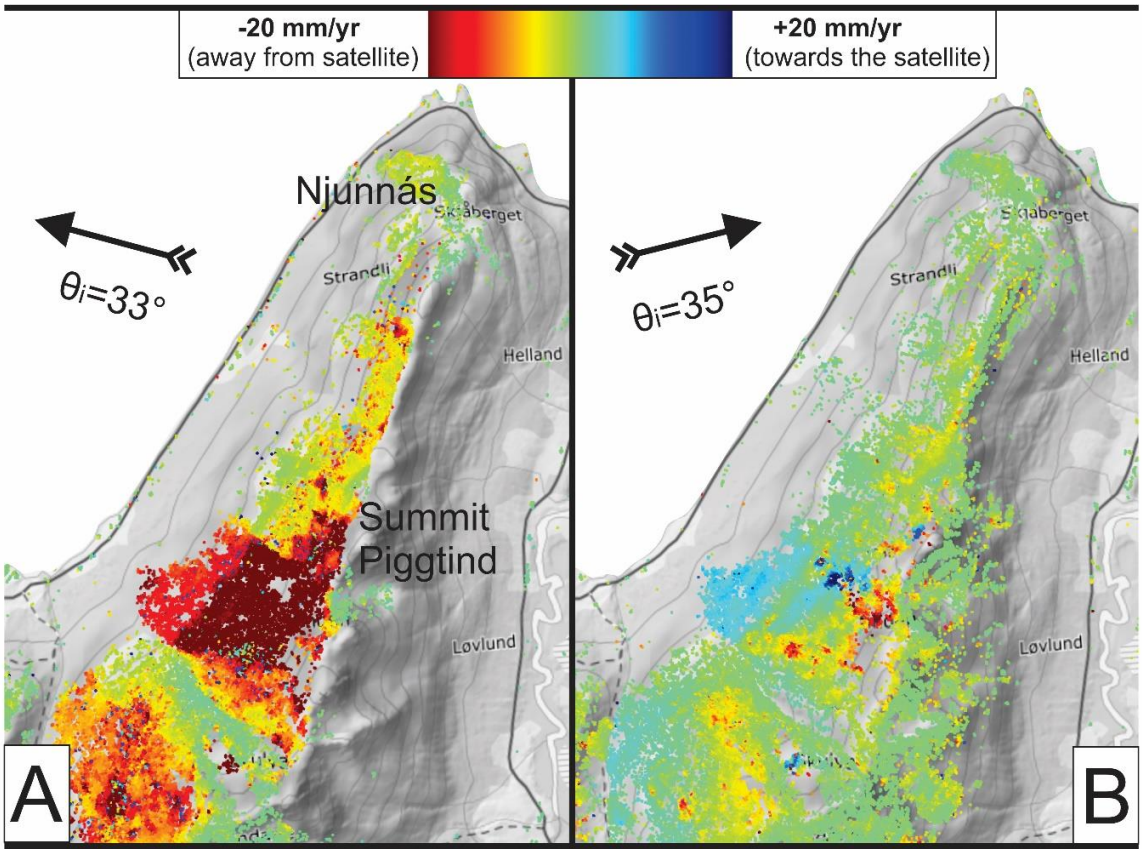

Figure 4.2: The figure shows mean annual surface displacement at Piggtind obtained from (A) descending dataset 1 and (B) ascending dataset 1 (modified print screen of InSAR Norway (http://insar.ngu.no). The LOS orientation for both datasets are displayed with a black vector (azimuth angle), and the incidence angle is denoted in degrees. The figure clearly indicates that the southern section is subjected to a considerable deformation at the present date (high mean annual velocity in mm/yr). Link to Piggtind on InSAR Norway: http://insar.ngu.no/Piggtind

4.1.2 2D InSAR method

InSAR measurements, which are one-dimensional, can only detect displacement along LOS (Section 2.1.2). This is a major disadvantage since the displacement rarely is entirely parallel to the LOS (Wright et al., 2004). To fully understand how much of the actual displacement we are observing, comprehensive knowledge about the displacement direction with respect to the LOS is needed (Samsonov et al., 2020; Grahn et al., 2019). In 2020, NORCE, funded by the European Space Agency (ESA), developed a Geographical information system (GIS) compatible tool allowing for 2D InSAR calculations. The tool exploits two (or more) overlapping SAR geometries with different LOS to estimate combined 2D displacement (mean annual velocity) (Fig. 4.3). The tool comprises multiple functions, allowing the user to exploit 2D displacement information in map view and along topographic profiles (profile tool). Furthermore, temporal variations in displacement can be evaluated by utilizing the time-series function.

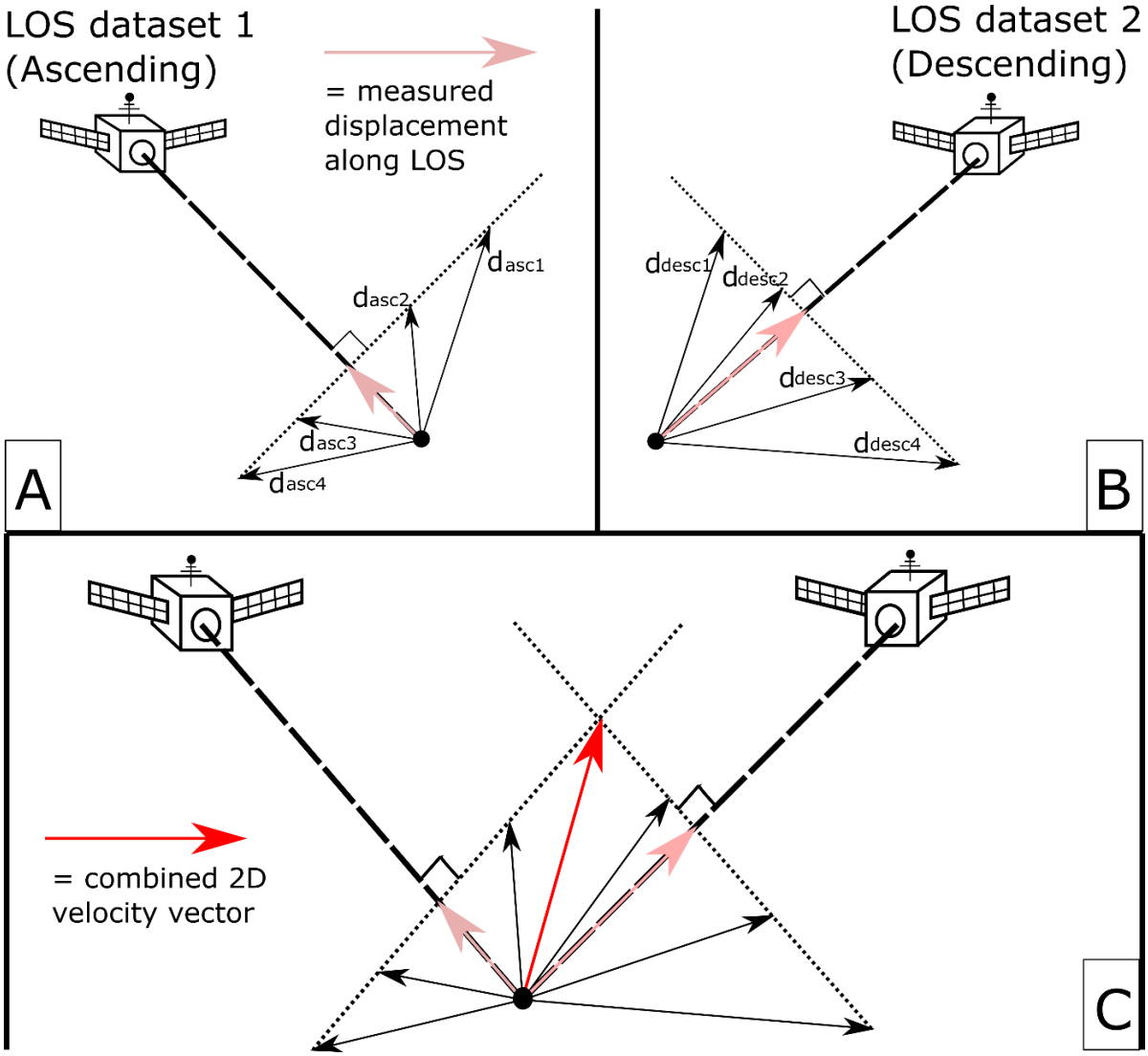

Figure 4.3: Figure illustrating how 2D InSAR method allows for combining multiple geometries to reduce the LOS-ambiguity. Fig A: Using single geometry, all black vectors (dasc1-4) result in the same LOS-projected displacement (pink vector), meaning that it is impossible to identify the true displacement direction and magnitude. The same applies for descending geometry displayed in Fig.B. However, when observing the displacement with two (or more) complementary LOS datasets, identifying the true magnitude and direction becomes possible (red vector) (Fig.C).

InSAR data from 2015–2019 (June–October each year), made available through *InSAR Norway* (InSAR data Piggtind), have been used to create the 2D InSAR results presented in Section 5.1.6 and 6.1.5. Three ascending- and three descending geometries acquired from the Sentinel-1 satellites are combined to ensure the best possible spatial coverage. From the calculated combined 2D displacement, multiple biproducts are derived. The tool decomposes the combined 2D velocity vector into a horizontal (E-W) and vertical (up-down) component. Furthermore, the dip of the combined 2D velocity vector (in the E-W plane) is identified (Fig. 4.4).

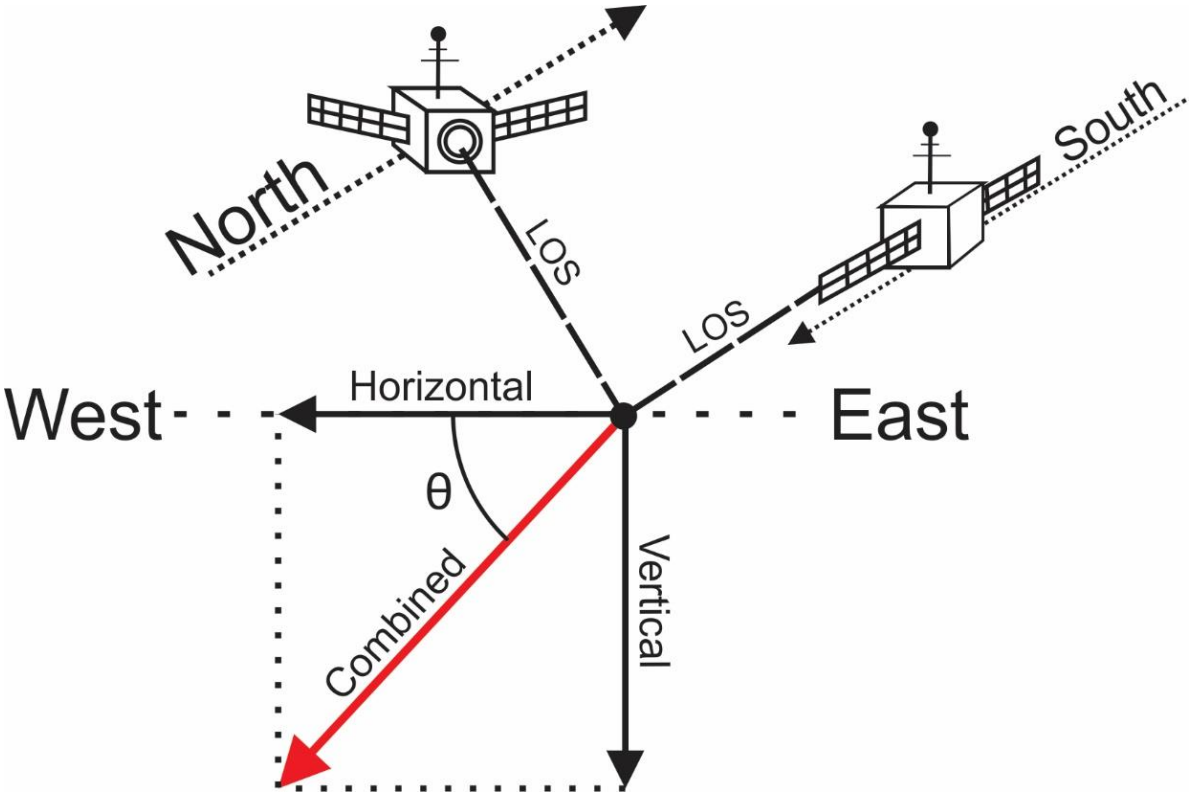

Figure 4.4: Displacement in E-W oriented cross-section. The combined 2D velocity vector has been decomposed into a horizontal- (E-W) and a vertical component. The red vector represents the combined 2D velocity vector, and the dip is expressed by θ in degrees from the horizontal plane. Inspired by Eriksen et al. (2017).

In order to calculate the combined surface displacement (CSD points), the LOS datasets need to be spatially aligned. The same reflector/target on the ground must be identified by both ascending- and descending satellites. However, the pixels from the two LOS datasets are rarely exactly intersecting (same geographic position). Therefore, it is assumed that the points represent circles with a given radius (step 2 Fig. 4.5). The radius (sample intersection radius), which the user can adjust, essentially controls the spatial resolution and accuracy of the output. A large sample intersection radius will generate more intersections and, consequently, more CSD points. However, this may adversely affect the accuracy since LOS measurements representing disparate targets may be utilized to generate the same CSD point. Contrary, a small radius will enhance the accuracy but generate fewer CSD points. When two LOS datasets intersect and thus creates a CSD point (step 3 on Fig. 4.5), LOS data are interpolated onto the point by weighted neighborhood interpolation. All LOS data located within a chosen radius (neighborhood radius) are calculated as an average value and attributed to the CSD point (step 4 Fig. 4.5). Then, as demonstrated in Fig. 4.4, the combined 2D velocity vector can be decomposed into a horizontal and vertical component.

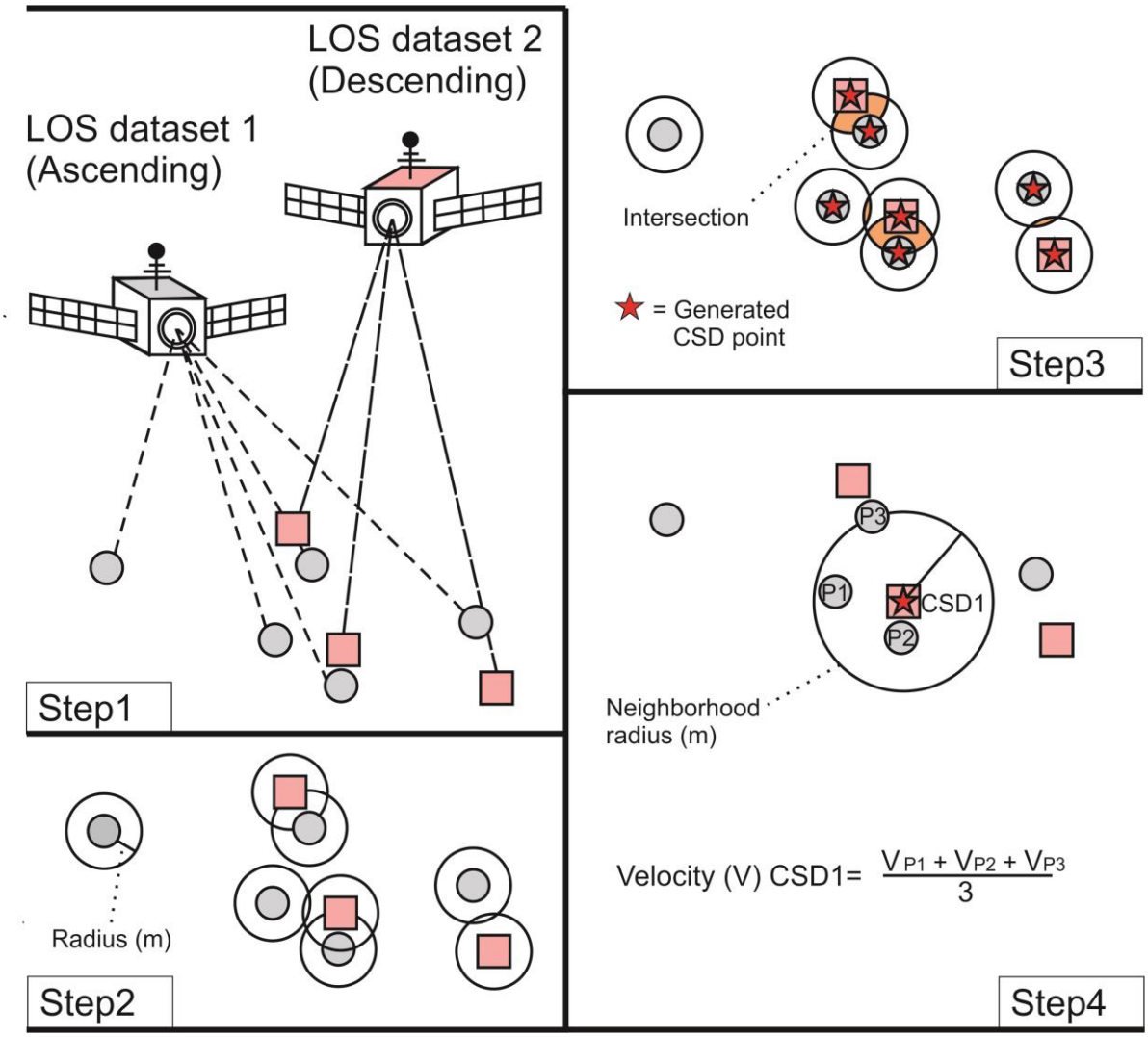

Figure 4.5: Procedure for generating CSD points and attributing LOS data. Inspired by Grahn, (2019)

Since InSAR is a relative technique, it is critical to calibrate the data to a reference point with known velocity, preferably zero displacement. Furthermore, when applying multiple LOS datasets to create 2D InSAR, it is imperative that all datasets are calibrated with respect to each other. Tests were performed to calibrate the data to a local reference point with postulated zero displacement. However, when validating the calibration (examining velocity on in-situ bedrock) and comparing it to the original calibration completed by InSAR Norway, it is evident that the original calibration is more successful (Fig. 4.6). The InSAR data obtained from *InSAR Norway* is internally calibrated between each processing tile measuring 5x5 km.

As reviewed in Section 2.1.2, the geometry of the SAR device and the roughly N-S-oriented flight path limits the ability to obtain displacement information from the N-S plane. We,

therefore, need to impose some information regarding the displacement in this blind plane. During the computation of CSD points, this is determined by the parameter "regularization". Displacement orthogonal to the main displacement direction is assumed to be constant zero. The direction where we assume zero displacement is manually determined and should be based on prior knowledge (Grahn, 2019). In this thesis, the main movement direction of the RSD and subsequently the direction of zero displacement, is determined by evaluating structural indicators (extensional features) and the dip direction of the structures suggested to create the basal rupture surface (Table 4.2). When investigating the rock glacier, the direction of movement is assumed to follow the topography (slope inclination and orientation/aspect of the slope surface).

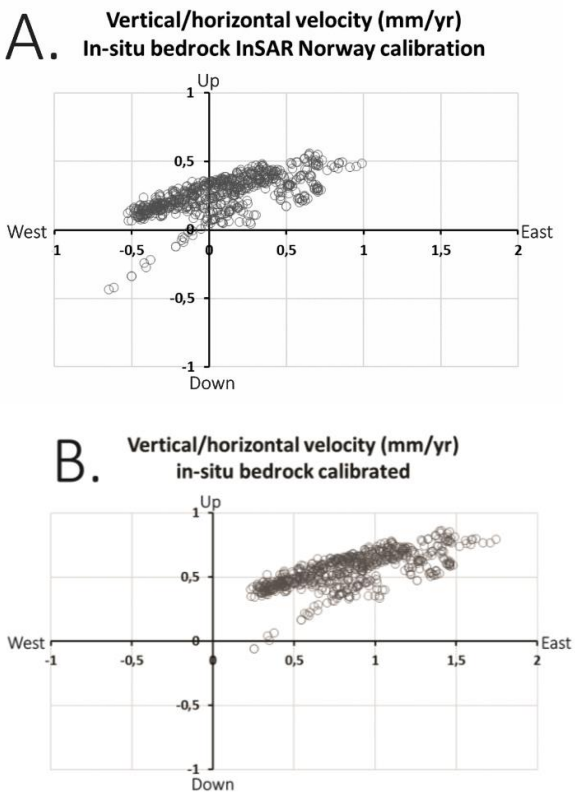

Figure 4.6: Calibration completed by InSAR Norway (A.) and local calibration to an area in Sjøvassbotn (B.). The scatter plots display vertical- and horizontal velocities from rock postulated to be stable, meaning that the velocity theoretically should be close to zero. As highlighted by the figure, the author's attempted calibration has resulted in a shift in the cluster towards east and up (B.).

Table 4.2: Summary of input parameters when computing CSD features for Njunnás and Piggtind/Skulvatindane

Parameters		**Applied techniques and values**
Alignment		
	Sample intersection radius (m)	15 m applied when evaluating RSD on Njunnás 20 m applied when evaluating the RSD and 10 m used when evaluating the RG on Piggtind/Skulvatindane
	Type of interpolation	Weighted neighborhood 50 m search radius (RSD) and 30 m (RG). Uniform neighborhood weight.
Regularization		
	Type	Constant zero
	Direction	Bearing (degrees). Assumed zero displacement perpendicular to postulated displacement direction (20° for Njunnás and Piggtind/Skulvatindane)
Calibration		
	Method	None (original calibration from InSAR Norway)

Fig. 4.7 shows the utilized color scales for displacement rates (mm/yr) and aspects of the combined 2D displacement. Horizontal displacement towards east and vertical displacement upwards (above horizontal plane) are denoted with positive values and blue color, while displacement down- and westwards are highlighted with red color and negative values. The magnitude of the combined 2D velocity vector is represented with a color bar ranging from blue (zero velocity) through yellow to red (maximum observed velocity). The dip of the displacement is represented with a color palette divided into sectors of 15°. Mean annual velocities are consistently stated in mm throughout the thesis.

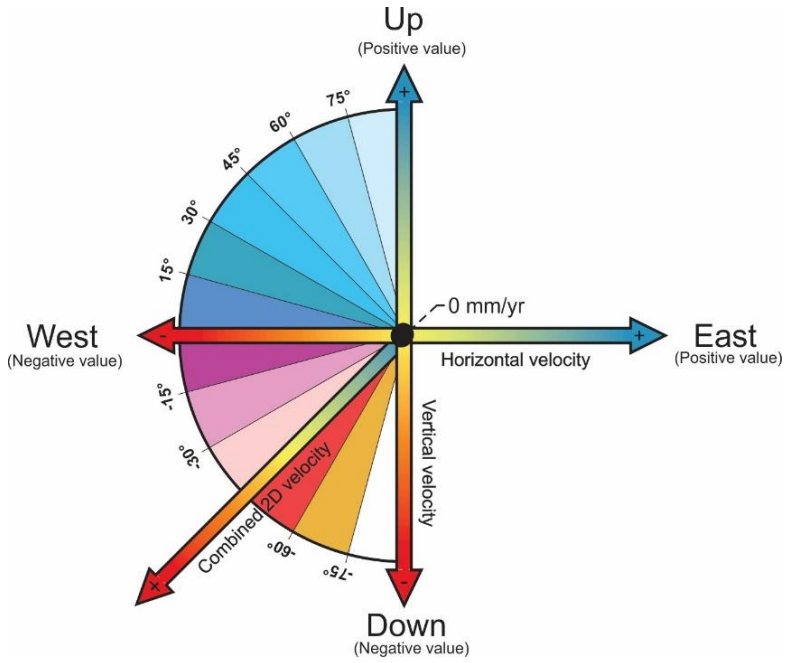

Figure 4.7: Color conventions used in the thesis to describe displacement rates and direction in map view. Inspired by Eckerstorfer et al. (2018) and Eriksen et al. (2017).

4.2 Geological analysis

4.2.1 Fieldwork and rock slope stability assessment using kinematic analysis

Field data were collected during an eight days long field campaign in September/early October 2020. The main focus was to map morphological elements and to collect structural data. The orientation of foliation and joints were recorded using the Fieldmove Clino app delivered by Midland Valley Ltd. Additional structural data collected by NGU (Böhme, M., Bunkholt, H., and Henderson, I.) and Geo-3135 2020 course has been integrated to ensure better spatial coverage and distribution. In total, 1732 orientation measurements of foliation and joints have been collected, and all are presented as dip/dip direction (in degrees). Utilized software's for geographically projection and external data resources are listed in Appendix 1 & 2.

The measured discontinuity orientation has been analyzed using Dips8 (https://www.rocscience.com/) and presented as poles in an equal angle and lower hemisphere projection. Based on the pole densities, trends in the natural discontinuities are recognized, and the average orientations are determined by the tool "sets from cluster analysis". In addition, the 1σ variability is displayed. A simple kinematic analysis has additionally been performed to evaluate the kinematic failure mechanisms. Structural features such as faults, joints, and folds, control the internal behavior of the rock mass, and the orientation may potentially enhance or reduce the stability of slopes (Stead and Wolter, 2015; Agliardi et al., 2012). The analysis aims to evaluate which discontinuities have the potential to facilitate certain failure modes, i.e., planar sliding, wedge sliding, and flexural toppling (Rocscience, 2021) (Fig. 4.8). The analysis does not account for external factors such as seismic activity, groundwater changes, and thus it only provides indications of the stability conditions (Wyllie and Mah, 2004). Furthermore, even though the method is successfully applied on RSDs around the world (Böhme et al., 2013; Gischig et al., 2011), it was initially developed for artificial (mine benches and road cuts) (Stead and Wolter, 2015). Hence, applying the method on large instabilities with potentially very heterogeneous slope properties (significant variations in aspect and inclination) and a more complex failure mechanism may be problematic (Park et al., 2016).

Three failure modes are evaluated in the analysis, of which all have certain requirements regarding the orientation of the discontinuities. (1) Planar sliding occurs when a planar basal rupture surface is dipping steeper than the friction angle of the rock. However, it must additionally dip gentler than the slope surface (Fig. 4.8a). This latter requirement ensures that the rupture surface "daylight" in the slope, meaning that the unstable block lacks support in the lower end (Wyllie and Mah, 2004; Hermanns et al., 2012). (2) Wedge sliding occurs when two discontinuities with opposite dip direction intersect, creating a wedge in between (Hungr et al., 2014; Wyllie and Mah, 2004). Thus, the displacement transpires along two gliding surfaces simultaneously, and the direction is constrained by the intersection line (Fig. 4.8b). In cases where one of the two planes is more favorably oriented, e.g., one is significantly gentler inclined (more horizontal), sliding can occur on only one discontinuity plane, and the other works as a steep release plane (one-sided wedge sliding) (Rocscience, 2021). (3) Flexural toppling can potentially develop if the discontinuities dip steeply into the slope and strike approximately parallel to the slope (Hungr et al., 2014; Hermanns et al., 2012). This failure mechanism requires densely spaced discontinuities separating continuous columns of rock (Fig. 4.8c).

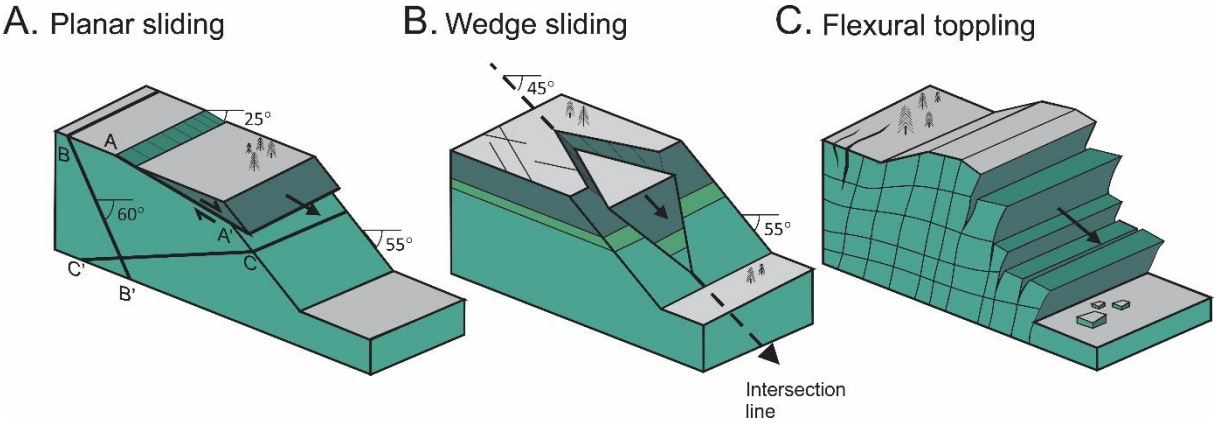

Figure 4.8: Three different failure mechanisms tested in the kinematic analysis. Left figure (A.) displays a planar slide (translational slide) on a basal rupture surface gentler inclined than the slope (line A-A'). Line B-B' and C-C' represents potential basal rupture surfaces; However, their orientation with respect to the slope surface, prevents sliding. The middle figure (B.) shows wedge sliding along an intersection line gentler inclined than the slope surface. Right figure (C.) demonstrates how steeply dipping, and densely spaced discontinuities may adversely affect the stability of the slope and result in flexural toppling. Inspired by Wyllie and Mah (2004) and Hungr et al. (2014).

To conduct the kinematic analysis, a series of parameters are determined. As highlighted, the relationship between the slope orientation and the discontinuities are of great relevance. However, the slope properties may be difficult to determine since large-scale RSDs often have a heterogeneous surface. Therefore, choosing one value to represent the whole slope is a major assumption (Park et al., 2016). In the analysis, the slope properties are calculated as average values with the tool "zonal statistics" in ArcMap. To take into account the variations, the standard deviations are attributed to the mean value (Table 4.3). In addition to the geometry of the slope, the friction angle and lateral limits are required for evaluating the kinematic failure mechanism. Such values are chosen based on recommendations and prior experience with RSDs in Norway.

Table 4.3: Input parameters kinematic analysis Dips8. Friction angle and lateral limits are based on recommendations from Hermanns et al., 2012.

		Njunnás	**Piggtind/Skulvatindane**
Friction angle		20°	20°
Lateral limit		30°	30°
Slope properties (mean and standard deviation)	Inclination	30° ± 9°	24° ± 6°
	Aspect	286° ± 62°	294° ± 29°

4.2.2 Geomorphological mapping

Superficial/surficial material categorization

The surface cover has been mapped and categorized to highlight areas where InSAR has limitations, investigate the causes of the displacement measured using InSAR, i.e., slope process, and reveal the spatial distribution and extent of the different superficial slope processes and RSD. The classification's leading source of information has been field observation, satellite images, orthophotos, and aerial photos supplied by NGU.

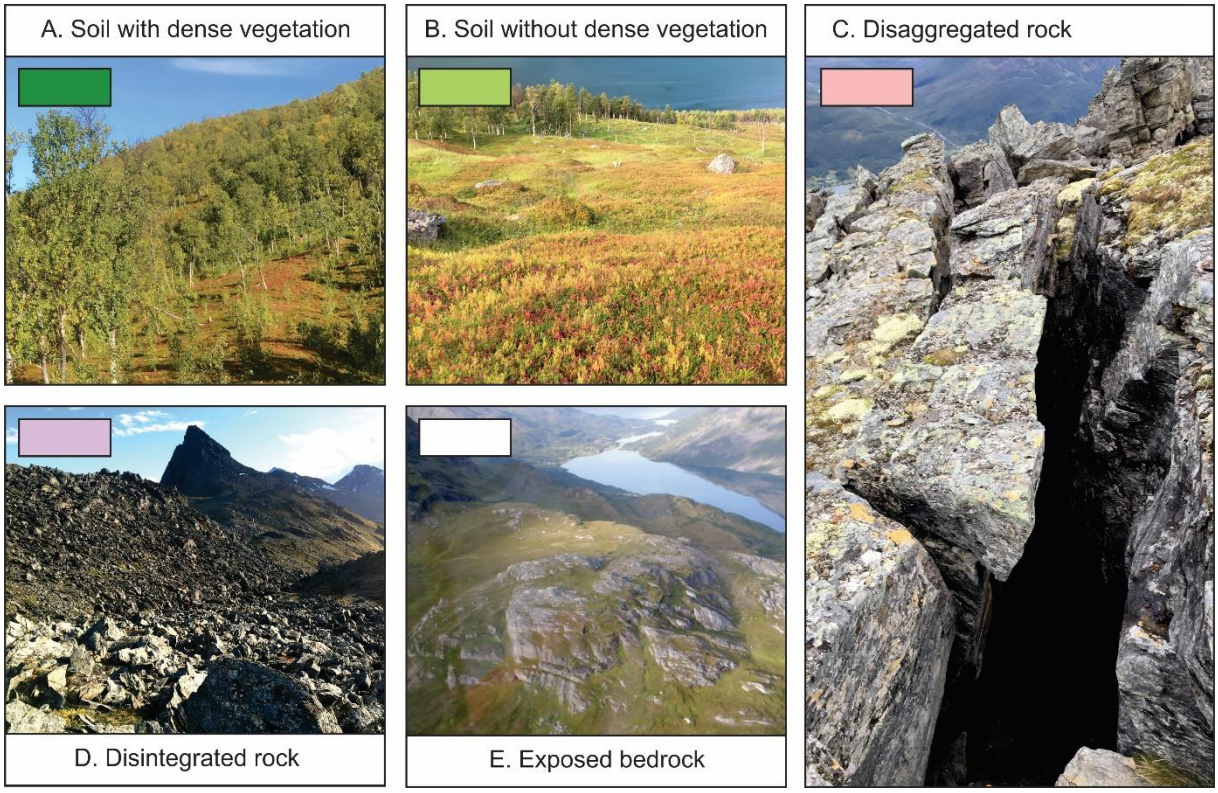

Figure 4.9: The surface cover has been divided into five units: (A) soil with dense vegetation, (B) soil without dense vegetation, (C) disaggregated rock, (D) disintegrated rock, and (E) exposed bedrock. Attributed color corresponds to those applied in the superficial/surficial material categorization presented in the results chapters. Picture source: private and Martina Böhme (NGU).

The surface cover has been divided into five classes: Soil with dense vegetation, soil without dense vegetation, disintegrated rock, disaggregated rock, and exposed bedrock (Fig. 4.9). "Soil with dense vegetation" represents all areas with dense forest/shrubs. Obtaining displacement information with InSAR from this unit can potentially be problematic since vegetation tends to cause temporal decorrelation (Section 2.1.2). The absence of InSAR data does, therefore, not mean that there is no displacement. "Soil without dense vegetation" is used on all areas with hummus cover and only scattered or no vegetation. This class is highly susceptible to frost action, and solifluction features may be present. "Disintegrated rock" and "disaggregated rock"

are both related to the rock slope deformation. "Disintegrated rock" is used where the rock is out-of-contact, meaning that the source is difficult to determine. This unite is characterized by loose unconsolidated rock debris and potentially subjected to a superficial deformation. "Disaggregated rock" still has rock bridges in-contact but is clearly gravitationally deformed, as manifested by the high presence of morpho-gravitational elements. Observed displacement in this unit is believed to represent the kinematics of RSD. "Exposed bedrock" is used on rock outcrops that display relatively few or no morpho-gravitational structures, meaning that this unit is inferred to be in-situ/not deforming.

Morpho-gravitational elements

Extensive mapping of morpho-gravitational elements has been conducted to understand the extent of the deforming area, investigating structures controlling the deformation, i.e., lateral and rear limits and basal rupture surface, and relating spatial variations in displacement to specific structures. All structures are mapped using satellite images, orthophotos, hillshades, slope inclination maps, aerial images, and field observations. A selection of structures related the gravitational deformation are displayed in Fig. 4.10.

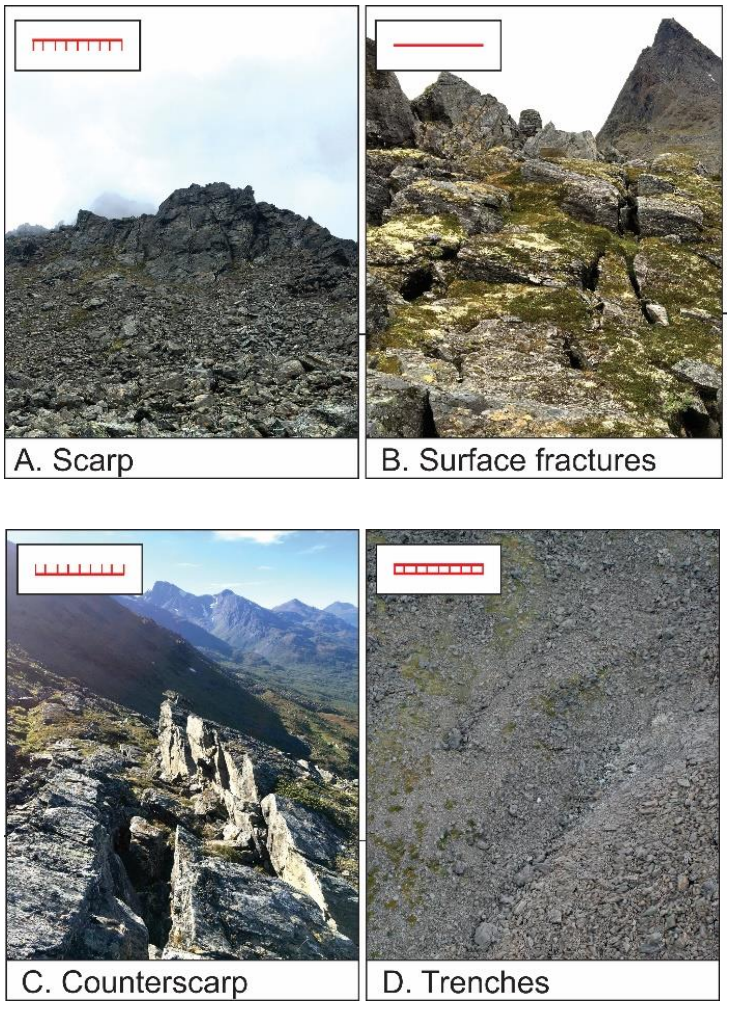

Figure 4.10: A selection of morpho-gravitational structures: downslope facing cliff, denoted scarp (A), surface fractures (B), uphill facing scarps, termed counterscarp (C), and a linear surface depression termed trench (D). The attributed red symbols correspond to those applied in the Morpho-gravitational map presented in the result chapters. Source: private and Henderson, I. (NGU)

4.3 Procedure for slope movement investigation using 2D InSAR and geological analysis

Mountainous regions in periglacial environments often show a complexity of overlapping processes. Geomorphological mapping, including superficial material categorization and morpho-gravitational mapping, is the first step in recognizing landforms or areas susceptible to superficial deformation. RSDs, rock glaciers, solifluction, and superficial deformation of postglacial deposits, all display certain characteristic surface features. However, identifying and delimitating them solely based on geomorphology may be challenging.

An additional approach investigating kinematics is therefore considered beneficial. I hypothesize that rock glaciers, RSDs, and superficial deformation in postglacial deposits (including solifluction) should be possible to identify and delimit based on their distinct kinematic behavior observed with 2D InSAR. This section highlights the characteristic disparities in kinematics between the various slope processes and proposes a methodology for evaluating them with 2D InSAR.

The surface velocities on an active rock glacier are expected to be in the order of cm–m/yr (Eriksen et al., 2018; Rouyet et al., under review). This is conventionally higher than expected for RSDs, which usually displays rates in the order of mm–cm/yr (Crosta et al., 2013; Agliardi et al., 2001; Vick et al., 2020). This conjecture, assuming a distinction in velocity, may provide valuable information about the spatial extent of the two landforms. Indeed, this kinematic approach using InSAR to identify and delimit periglacial landforms (Rouyet et al., under review; Barboux et al., 2014; Hestad, 2019; Wang et al., 2017) and RSDs (Lauknes et al., 2010; Dini et al., 2019b) are frequently applied in regional inventorying studies.

The displacement in superficial slope processes is predominantly controlled by the surface topography (aspect and inclination of the terrain) (Matsuoka et al., 2001; French, 2007; Singh et al., 2011). It is, therefore, presumed that the dip of the 2D velocity vector would be approximately parallel to the slope surface. However, it should be emphasized that this assumption only is valid when investigating mean annual displacement for the periglacial landforms, as is the case in this thesis. As reviewed in Sections 2.2.2 and 2.2.3, significant temporal variations are expected between the periods of thawing and freezing. RSDs show a somewhat different pattern since the displacement transpires along deeper structures (i.e., basal rupture surfaces) rather than the slope surface (Agliardi et al., 2001). The dip of the 2D velocity

vectors will, therefore, potentially reflect the geometry of the basal rupture surface (Intrieri et al., 2020; Eriksen et al., 2017; Frattini et al., 2018; Böhme et al., 2016).

To investigate if deeper structures or the surface topography controls the displacement, the computed 2D velocity vectors were subtracted from the slope inclination. This allows identifying the angle between the displacement and the slope surface (Eriksen et al., 2018; Eriksen et al., 2017; Crippa et al., 2021). Negative values imply displacement into the slope, while positive values indicate displacement out of the slope. Furthermore, values close to 0°, suggests that the displacement is parallel to the slope surface. If such values are observed in units susceptible to superficial deformation, i.e., disintegrated rock or soil without dense vegetation, it may insinuate that the displacement is controlled by the surface topography, meaning that we potentially are observing a superficial process. Contrary, large angles imply less correlation between surface topography and displacement direction. Hence, the displacement is potentially controlled by deeper structures rather than surface topography.

Considering the spatial resolution of the input data (ascending and descending: 5x25 m) and the chosen search radius in the construction of 2D InSAR (20 m), the calculations are performed with a 50 m resolution slope raster. However, an exception is made when evaluating small-scale features such as lobes and bulges on the rock glacier. It is then considered necessary to decrease the search radius in the construction CSD points. Consequently, the spatial resolution of the slope raster readjusted to a higher resolution (10 m).

4.4 Analysis of kinematic behavior

The profile tool developed by NORCE allows for visualizing displacement rate distribution along profiles. The CSD points created by the combine tool are used as input and allows to observe changes in combined 2D velocity, dip of combined 2D velocity vector, vertical-, and horizontal velocity along topographic profiles with chosen geometric properties (curved, straight, etc.). The CSD points attributed to the profile are interpolated values based on CSD points located perpendicular to the profile, within a chosen width. Accordingly, not only points in direct contact with the profile are utilized, and the profile represents a band rather than a line (Table 4.4).

Table 4.4: Selected band width for the created profiles.

	Njunnás	**Piggtind/-Skulvatindane**			
	Profile A-A' (Fig. 5.9)	Profile A-A' (Fig. 6.8)	Profile B-B' (Fig. 6.8)	Profile C-C' (Fig.6.12)	Profile D-D' (Fig. 6.14)
Band width	100 m	40 m	40 m	100 m	30 m

As highlighted by Frattini et al., (2018), spatial variations in velocity along a longitudinal swath may disclose the geometry of the basal rupture surface of RSDs (Section 2.2.1). However, this assumption works if the diversities in velocity are not related to internal structures dissecting the RSD, secondary instabilities, or heterogeneous material properties. Furthermore, this assumes that the observed displacement indubitably is coupled to the RSD and not influenced by other superficial slope processes. By using the profile tool on the rock slope deformation at Njunnás and Piggtind/Skulvatindane, a more comprehensive understanding of the basal rupture surface and subsequently the failure mechanism can be derived (Frattini et al., 2018: Eriksen et al., 2017; Böhme et al., 2016).

In order to interpret the longitudinal kinematic patterns obtained from the profile tool, the results are compared with expected patterns based on fundamental mechanical knowledge. Fig. 4.11 shows a selection of different basal rupture surfaces and expected kinematic patterns derived from simple finite element simulations (Frattini et al., 2018). These simulations constitute the basis of the interpretation of the basal rupture surfaces in this thesis. However, it must be underlined that they are simplified examples. From the figure, we can see that both endmembers within sliding, translational- and rotational slides (Fig. 4.11 a & f, respectively) show a disparate kinematic pattern. The translational slide moves along a planar basal rupture surface with approximately constant dip. Consequently, the vertical velocity remains constant along the profile. Rotational slides (subcircular basal rupture surface) display high vertical displacement rates in the head domain (downward directed) and a gradual decrease towards the toe zone. Contrary, the horizontal displacement is negligible in the head domain but progressively increases further down the slide body, culminating in the toe zone. Such kinematic behavior indicates that the whole slope is being tilted backward (Frattini et al., 2018).

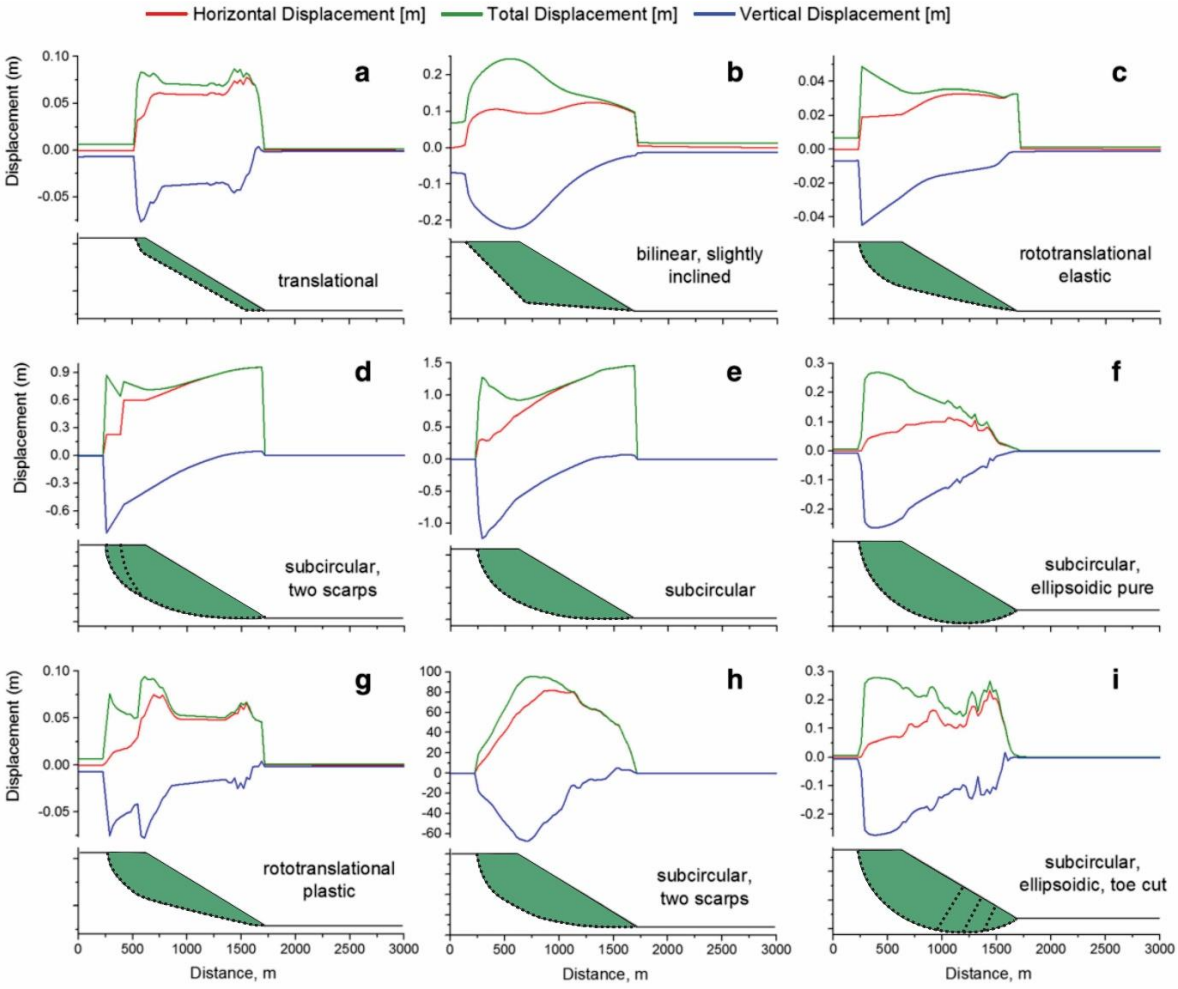

Figure 4.11: Displacement rate distribution along longitudinal profiles. Modified from Frattini et al. (2018).

The methodology used to study longitudinal variations in horizontal and vertical velocities provides solid indication about the geometry of the basal rupture surface and thus the failure mechanism. However, the method does not disclose any information regarding the depth of this surface. Such information, in addition to geometry, can be obtained by the proposed graphical method "vector inclination method (VIM)" (Intrieri et al., 2020). The method, which was developed prior to the development of InSAR technology, was originally dependent on structural indicators such as matching displaced surfaces and slicken side striations, to reveal the direction and magnitude of displacement (Carter & Bentley, 1985). The utilization of 2D InSAR has renewed the interest in the method since it now is possible to easily acquire accurate and spatially dense displacement measurements from RSDs (Intrieri et al., 2020).

In order to use the VIM, it is required that displacement information, including magnitude- and dip of combined 2D displacement is established along a profile in the form of vectors (black

arrows on Fig. 4.12). Fortunately, this is the direct output of the 2D InSAR profile tool, meaning that such information is easily acquired. Knowing the exact location of the back scarp, preferably also the toe, is critical since these two features represent the basal rupture surface where it daylights in the slope. The graphical method assumes that the observed displacement on the surface reflects the displacement at the basal rupture surface (i.e. a point on the slope surface will move parallel to the basal rupture surface), the RSD moves as a rigid body, and only one sliding structure exists (Intrieri et al., 2020). It is therefore critical to have those assumptions in mind when evaluating the location of the profiles. The surface cover should ideally be disintegrated rock with homogeneous material properties. Furthermore, structures dissecting the RSD and controlling the evolution of the deformation, should be absent or at least taken into account when interpreting.

The following section explains the procedure for evaluating the depth and geometry of the basal rupture surface, after Intrieri et al., (2020)'s vector inclination method:

1. A topographic profile with spatially well-distributed combined 2D velocity vectors is created with the profile tool. The topographic profile is extracted from a DEM with resolution 1x1m.
2. For each combined 2D velocity vector, a perpendicular line is constructed (solid black line on Fig. 4.12).
3. The intersection point between two consecutive lines is marked with an "oX".
4. From the intersection point ("oX"), a bisection line is established (dotted lines on Fig. 4.12).

When step 1-4 is completed, one can start drawing the basal rupture surface, starting from the top of the slope.

5. A straight line is constructed parallel to the first 2D velocity vector, starting at the backscarp. The point "p1" is established where this line intersects with the first bisection line.
6. From p1, a line parallel to the second combined 2D velocity vector is drawn and ends when intersecting with the second bisection line. This procedure is then repeated for all the combined 2D velocity vectors further downslope.
7. Step 5 and 6 are then repeated, however, now starting from the toe. The two postulated basal rupture surfaces are then interpolated, creating one surface. However, this requires that the toe is identified, which often is not the case in complex RSDs (Crosta et al., 2013)

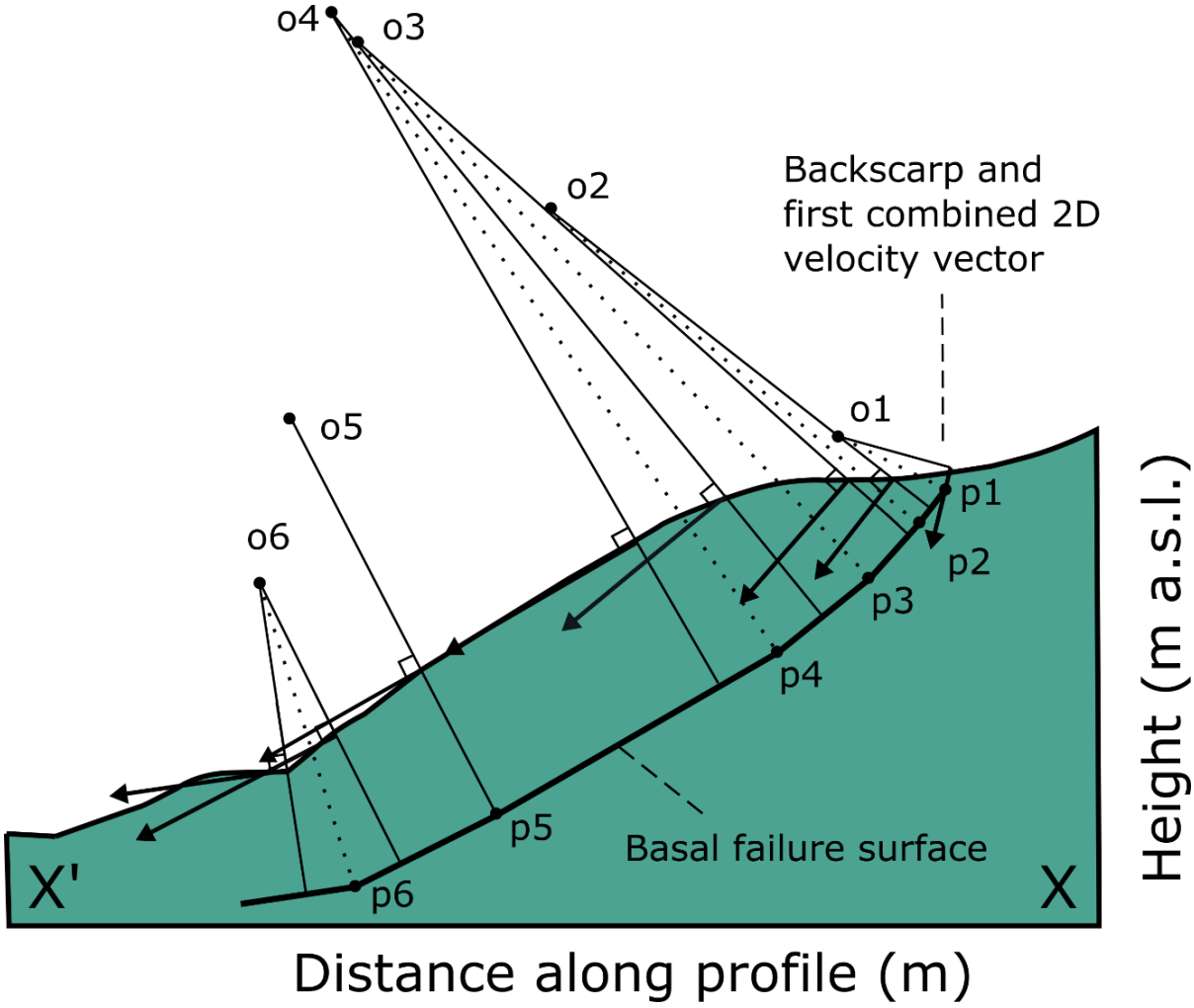

Figure 4.12: Graphical method (VIM) applied to interpret the geometry and depth of the basal rupture surface. The figure shows an instability lacking a clearly defined toe and sparse amount of displacement information in the lower altitudinal section.

By successfully identifying the geometry of the basal rupture surface, it should theoretically be possible to deduce which structures allow the deformation to progress, i.e., which pre-existing structures control the basal- and rear rupture surfaces. Such evaluation can be completed by comparing the dip of measured discontinuities with the dip of the postulated basal rupture surface. Alternatively, a lack of correlation between measured discontinuities and dip of the basal rupture surface may insinuate that the displacement propagates by forming new fractures.

5 Results and interpretation Njunnás

The following chapter presents the results (5.1) from the geological analysis (5.1.1–5.1.5) and the produced 2D deformation maps (5.1.6) of Njunnás. The results are then merged, creating 2D InSAR profiles with geological interpretations. Kinematic behavior, spatial extent, and variations in velocity are discussed and interpreted (5.2).

5.1 Results Njunnás

5.1.1 Morpho-gravitational analysis

The morpho-gravitational map presented in Fig. 5.1 shows structures related to RSD. In addition, the changes in surface morphology are displayed since they potentially can correspond to indirect effects of the gravitational deformation and therefore contribute to interpreting the spatial extent of the RSD.

Njunnás contains prominent structures typically related to a gravitational deformation. The backscarp corresponds to the upper limit of the deforming area and is interpreted as the scarp with the highest altitudinal position and no visible morpho-gravitational elements behind it (Fig.5.1). The upper section is dominated by persistent trenches, scarps, and counterscarps striking approximately N-S and NNE-SSW. These directions are also reflected in the large-scale architectural structures (Fig. 3.4 and Section 3.2.3). The middle section is highly deformed and contains a system of counterscarps oriented parallel to each other. Further down the slide body, the fracture density increases. The lower section is dominated by disintegrated rock and a transverse ridge. Multiple seepage points are located at the distal side of this ridge, and additional dry stream beds further suggest that considerable amounts of water daylight in this area during heavy periods of rain/snow melting. Multiple persistent lineaments oriented obliquely to the strike of the slope are found south from Njunnás. Considering the immediate vicinity of the fault trace mapped along the fjord (Fig. 3.4), these structures are inferred to be faults.

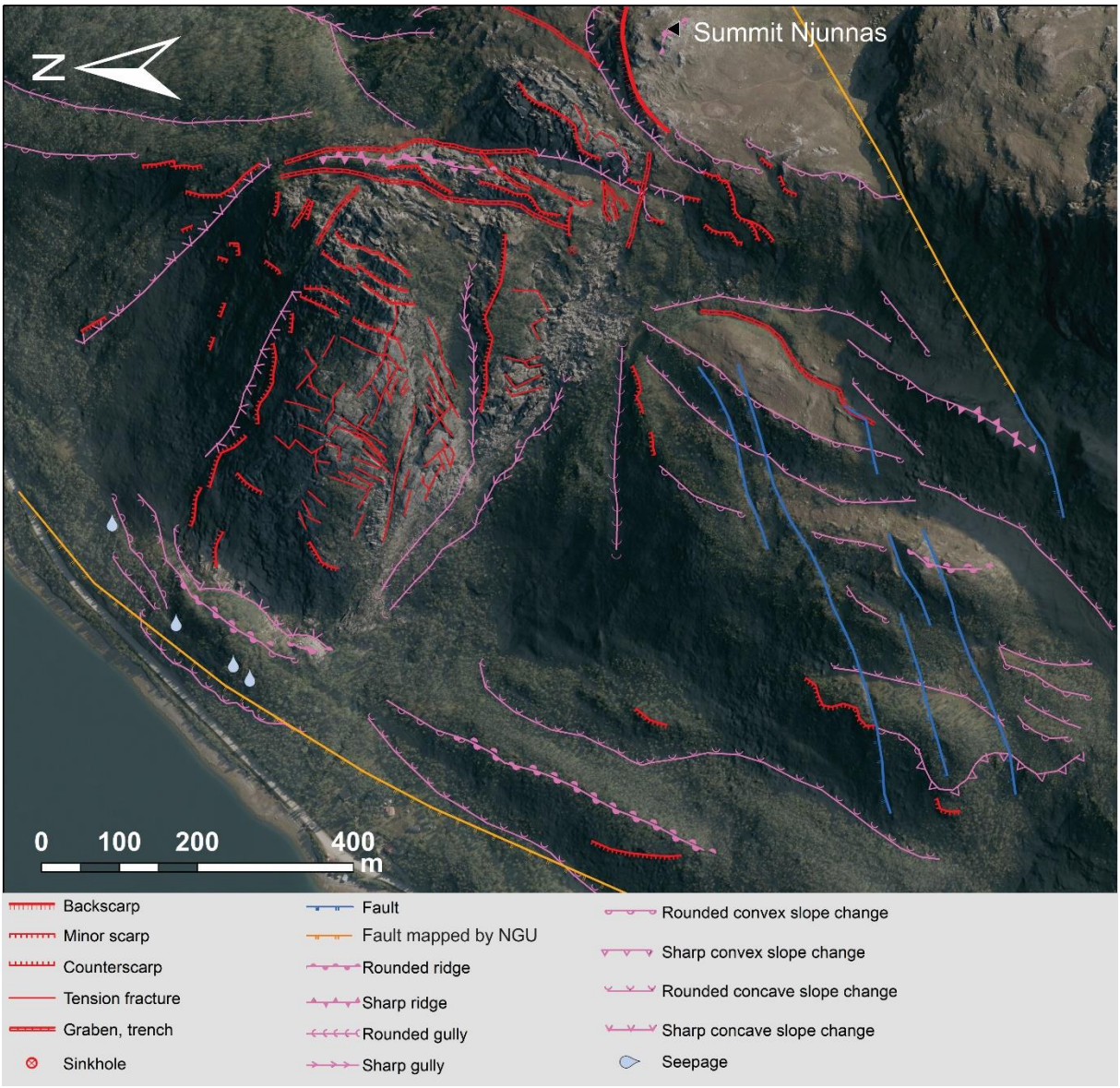

Figure 5.1: Morpho-gravitational map of Njunnás. Structures related to the gravitational deformation are displayed in red color, while changes in slope morphology are visualized in pink color. Faults mapped by NGU origin from the National bedrock database (Bedrock (ngu.no) with resolution 1:250 000 (NGU, 2020b). Background: orthophoto 2016 (NMA, 2020c).

5.1.2 Superficial/surficial material categorization

Vegetation and surface material has a strong influence on the interpretability of ground deformation with InSAR. Therefore, it is crucial to present a map that indicates surface material and vegetation coverage. The deformed area at Njunnás mainly consists of disaggregated and disintegrated rock (Fig. 5.2). The former class clearly dominates the upper- and middle sections of the slope, while disintegrated rock is found in the lower section and below the steep scarps at the lateral flanks. The extensive coverage of these two units witnesses the presence of previous/ongoing gravitational deformation and gives insights into the spatial extent of the

deforming area. However, Fig. 5.2 also reveals that dense vegetation surrounds the deforming area and is additionally found in scattered patches within the deforming area. The area surrounding the summit of Njunnás lacks morpho-gravitational element, which is a sign of limited deformation (Crosta et al., 2013; Agliardi et al., 2001).

An indicative outline of the RSD has been determined based on the spatial extent of morpho-gravitational elements and surface coverage related to slow rock deformation (Fig. 5.2).

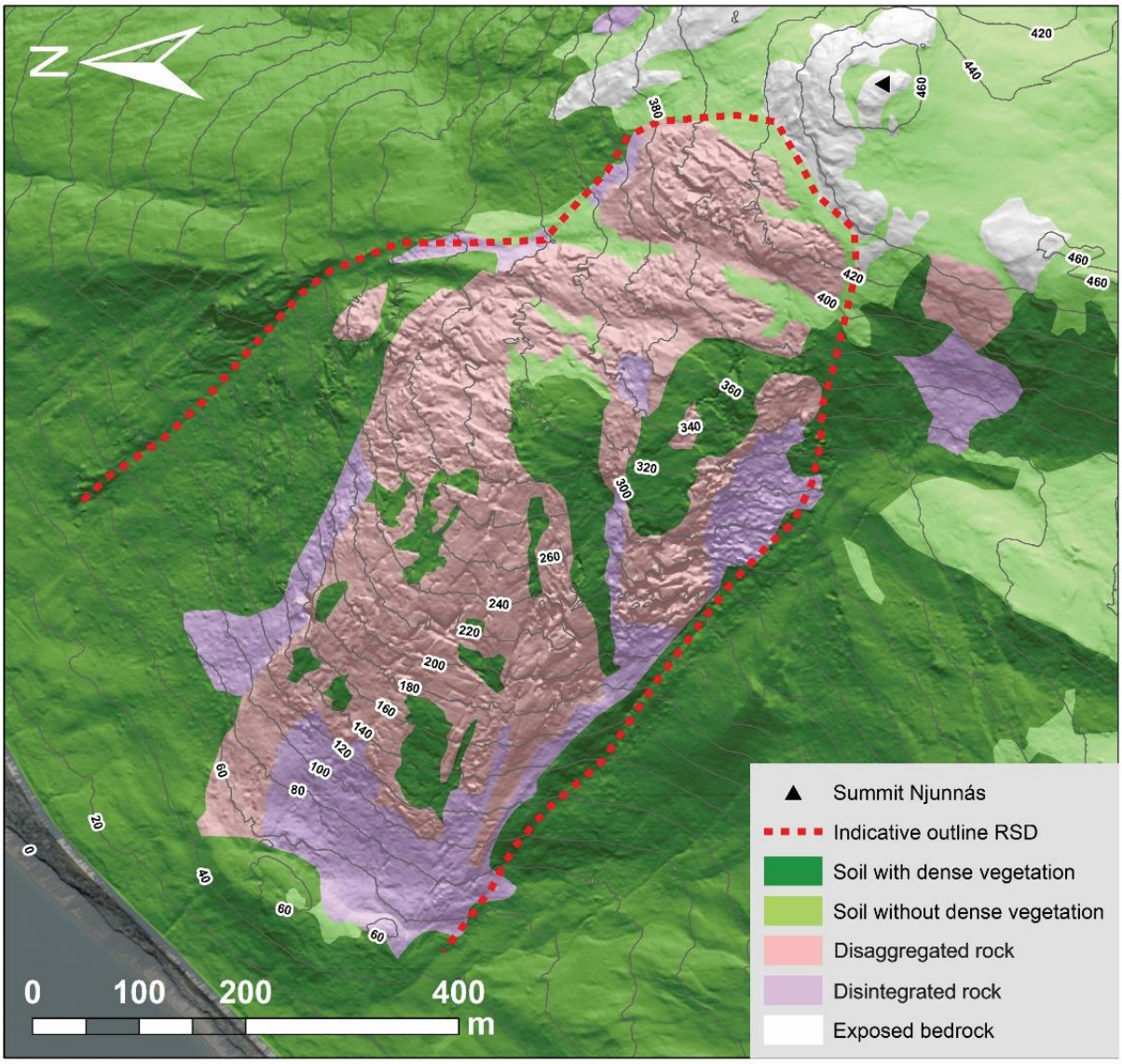

Figure 5.2: Superficial/surficial material categorization of Njunnás. The surface cover is classified into five units as described in section 4.2.2.

5.1.3 Structural analysis

An analysis of all structural data has been performed to evaluate overall trends, variations in the natural discontinuities, and to test for potential failure modes. In total, 323 measurements of joints and 253 measurements of foliation have been analyzed in a stereographic projection. The structural data originates from localities with and without obvious morpho-gravitational structures, meaning that some of the measurements are from outcrops inferred to be actively deforming, i.e., deformed bedrock with intact rock bridges (disaggregated rock), while others are from inferred in-situ bedrock. Based on the state of activity, the structural measurements are separated in the analysis.

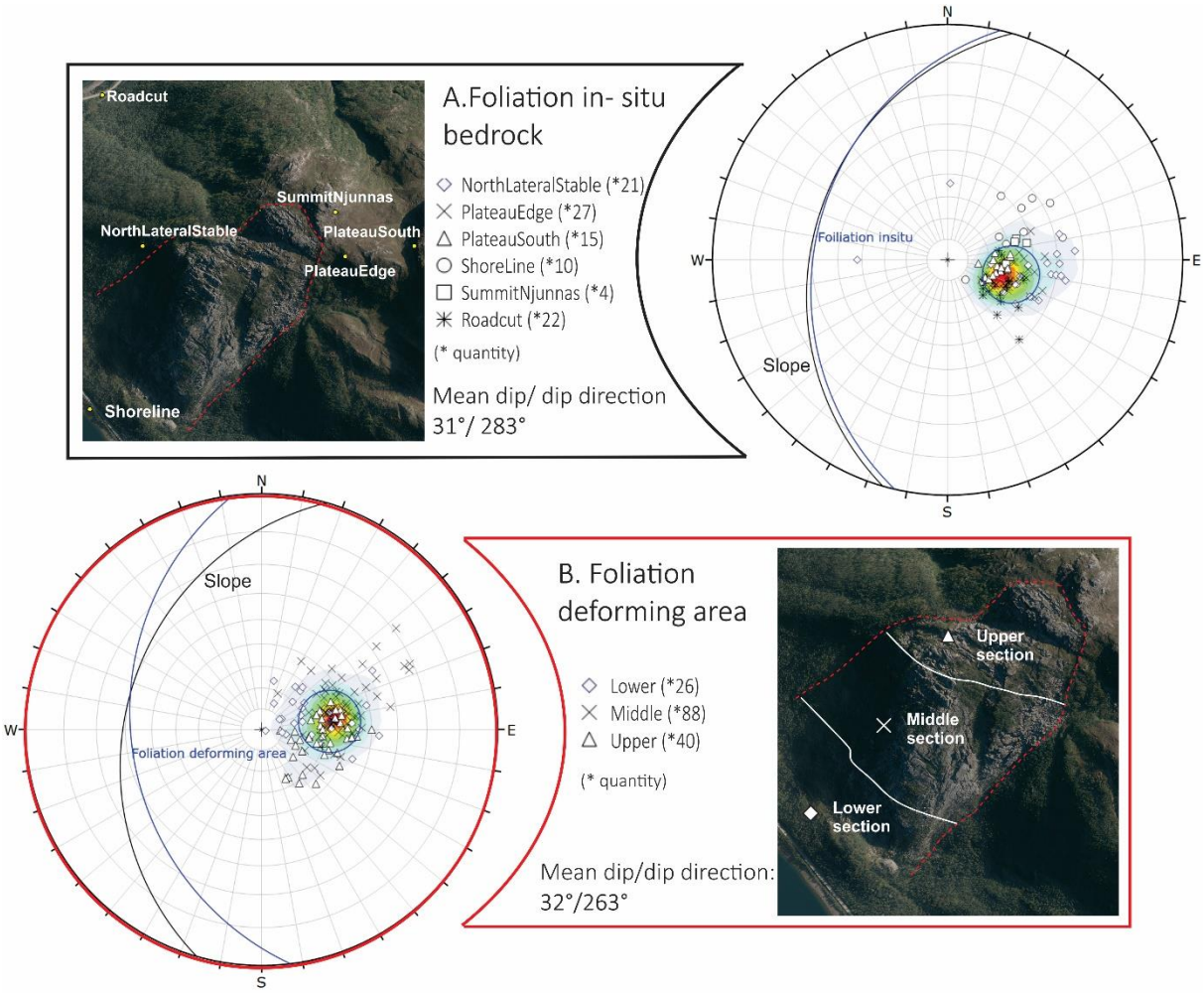

Figure 5.3: Stereographic projection of foliation measurements (stereo pole plot) from (A) bedrock in areas with rather no signs of morpho-gravitational deformation and (B) from bedrock in the area with abundant morpho-gravitational structures. The structural measurements are presented in an equal angle projection of the lower hemisphere. The mean surface (plane) and 1 σ variability cone (circle) are displayed. Data from the deforming area are separated into lower, middle, and upper sections in order to evaluate spatial changes. All observation points located within the disparate section are merged.

Fig. 5.3 displays the stereographic projection of foliation both inside and outside the deforming area. Some variations in dip and dip direction are observed between the inferred stable- and unstable sections of the slope. The average dip and dip direction in in-situ bedrock are calculated to be 31°/283° ± 13°, meaning that the foliation is dipping moderately towards the fjord. The measurements are quite consistent with only minor variations in orientation, i.e., dense cluster of poles (Fig. 5.3a). Within the deforming area, the orientation of the foliation shows a slightly higher variability (Fig. 5.3b). The average orientation is 32°/263° ± 14°. Increased dip angle is observed on blocks separated by counterscarps and towards the northern and southern flanks of the deforming area.

Three dominating joint sets (JN) are identified on Njunnás by examining the stereographic projection (Fig. 5.4) in addition to field observations. They are designated similar names inside- and outside the deforming area because they are inferred to represent the same structures. However, their orientations are not precisely the same.

JN1 is the most notable set within the deforming area and seems to control many of the big scale morpho-gravitational structures, such as counterscarps. On average, the set is dipping between 65–75° towards ESE-SE. It is characterized by a persistent nature and a relatively smooth surface compared to the other joint sets. Outside the deforming area, the set is less prominent. Indeed, the pole density is so low that it does not represent a disparate set in the structural analysis. However, because of the significance within the deforming area, it is also highlighted here. The set is frequently observed in in-situ bedrock, and the small amount of data representing the set may be connected to a sampling bias.

JN2 and JN3 are both sub-vertical to vertical. Both sets reveal an opposite dip direction inside- and outside of the deforming area, which can be explained by that the direction is ambiguous with dip values close to vertical inclination. Both sets are characterized by a rough surface and are generally less persistent than JN1. Both joint sets are more prominent outside the deforming area, but field observations suggest that they are eminent discontinuities within the deforming area as well.

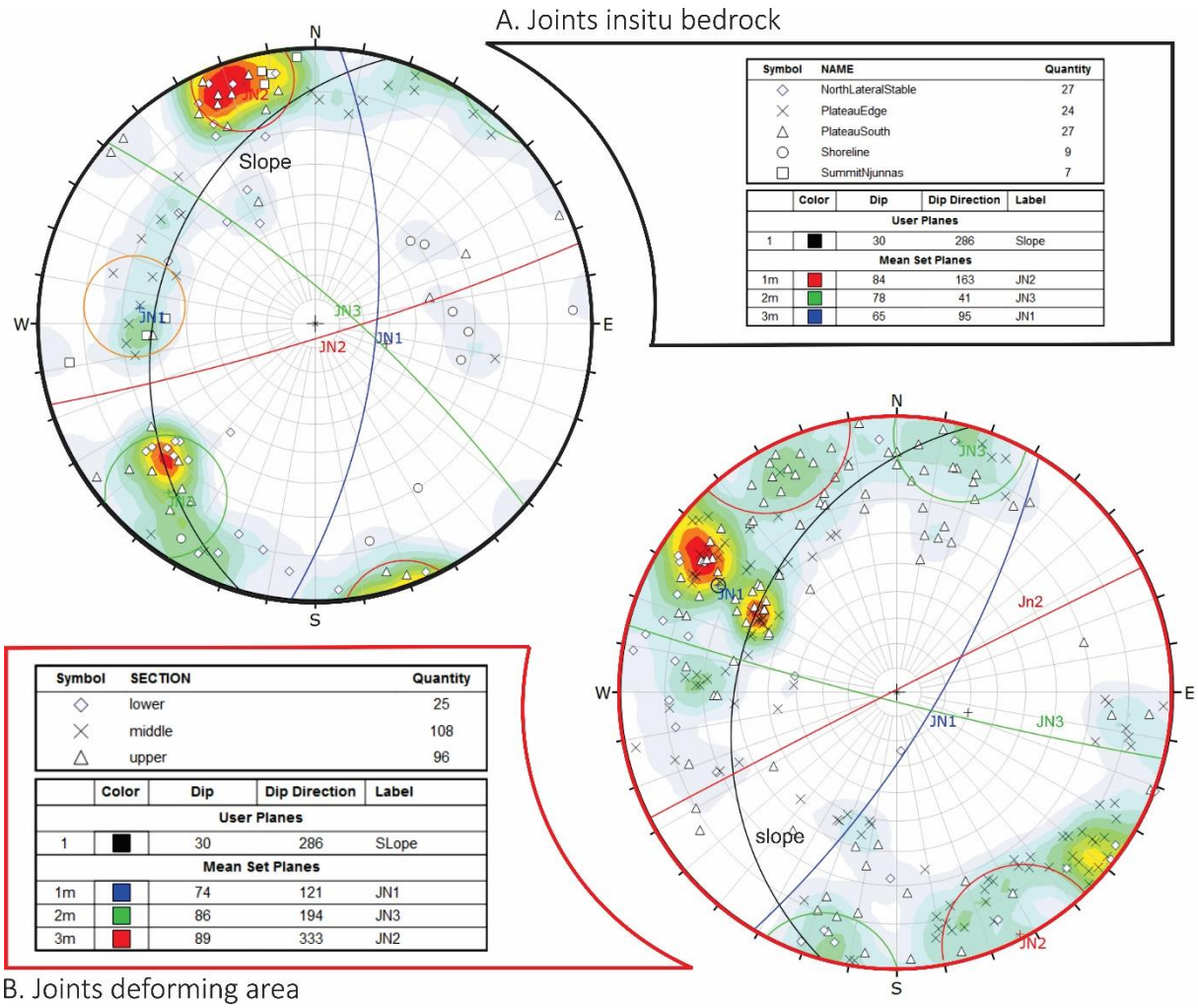

Figure 5.4: Stereographic projection of the joint planes from (B.) outcrops with abundant morpho-gravitational structures and (A.) inferred in-situ bedrock. The structural measurements are presented in an equal angle projection of the lower hemisphere. Based on the pole densities (clusters), three joint sets are recognized. The mean orientation is determined using cluster analysis and field observations (displayed as planes). The 1σ variability cone is attributed to each set.

5.1.4 Rock slope stability assessment using kinematic analysis

A kinematic analysis is performed using data from in-situ outcrops outside the deformation area. In total, 211 orientation measurements of discontinuities are used. To evaluate the kinematic behavior, certain parameters are defined; The mean aspect of the slope is estimated to be 286° ± 62°, and the mean slope inclination of the middle and lower section is approximately 30° ± 9°. The head domain is not included in the latter calculation since it is considerably lower inclined, and a potential basal rupture surface is expected to daylight further down the slide body. This is done to ensure that the mean slope angle does not get underestimated since that will affect the kinematic feasibility of the different failure

mechanisms. Due to the relatively large size of the slope and subsequent variations in the slope face, the lateral limit is set to 30°. The friction angle is set to 20°, which is a conservative value but recommended for large RSDs in Norway (Hermanns et al., 2012).

The kinematic failure analysis reveals that planar sliding is possible along the foliation (Fig. 5.5). The orientation of the slope surface and the foliation are approximately the same. They are both oriented W-WNW, and the dip of the foliation is only one degree higher than the average inclination of the slope. This situation is beneficial for planar sliding. 37.8% of all the foliation poles plot within the critical planar sliding zone (Fig. 5.5a). This is a significant proportion, and the remaining poles are located in the immediate vicinity of the critical zone. The slope is thus extremely sensitive to changes in the parameters in the model. A change in slope inclination of only 2°, which is realistic considering the gradual increase in slope inclination in the middle- and upper part of the lower section and the accuracy/resolution of the digital elevation model, would lead to approximately 50% critical foliation poles.

The analysis further reveals that wedge sliding also is kinematically feasible (Fig. 5.5b). The percentage of critical intersections compared to the total number is 18,3%, meaning that wedge slide is partly possible. However, an increase in slope gradient will also here greatly affect the result. By adding the standard deviation value to the average slope inclination (39°), the percentage of critical intersections goes up to 38,7%. Wedges can potentially form between the foliation and JN2, and the foliation and JN3. Sliding will then potentially occur along the intersection lines (foliation and JN2: 24°/250°, and foliation and JN3: 25°/317°). However, considering the steep dip of JN2 and JN3 compared to the foliation, the displacement could also transpire along the foliation (one-sided wedge sliding). The joints would then act as steep lateral release planes.

Flexural toppling is kinematically feasible with JN1 as a critical discontinuity. However, only 7,1% of the plane poles plots are within the critical zone (Fig. 5.5c). Hence a flexural toppling is unlikely in this area. An increase in slope gradient leads to the same increase as experienced for planar- and wedge sliding, but the number of poles located in the critical zone is still low (14,3%), especially when comparing to the other modes of failure.

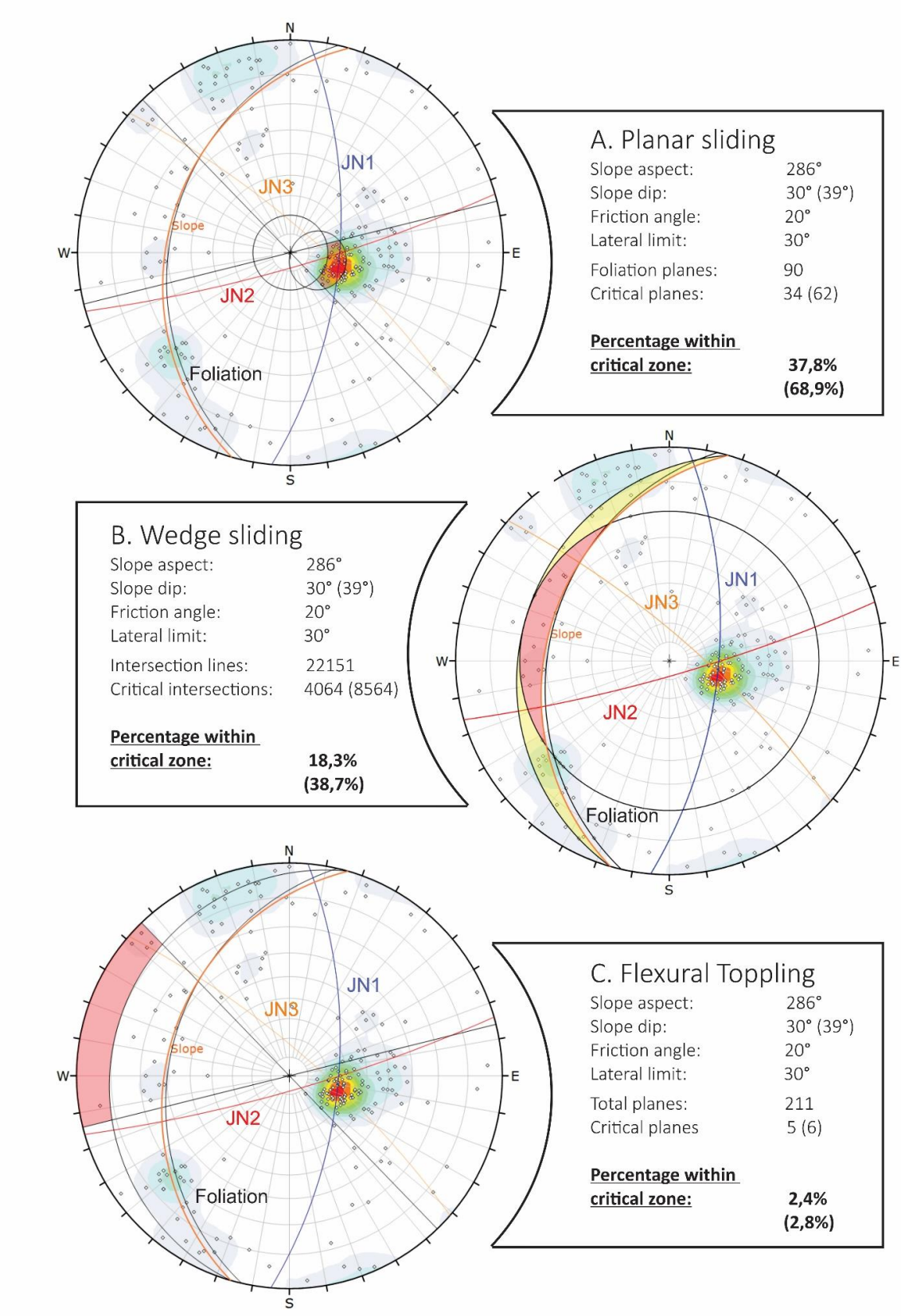

Figure 5.5: Kinematic analysis for three different modes of failure. The structural measurements are presented in an equal angle and lower hemisphere projection. The average orientation of the foliation and the three joints sets presented in Section 5.1.3 are also displayed.

5.1.5 Structural indicators and inferred sliding direction

The rock slope stability assessment using kinematic analysis discussed in Section 5.1.4 disclosed both wedge sliding and planar sliding as potential failure modes. For planar sliding, the foliation was postulated as the discontinuity creating the basal rupture surface. A similar observation was made for wedge sliding (one-sided wedge sliding); However, displacement along the intersection lines is also expected.

By assuming displacement along the foliation, the most plausible movement direction would then be approximately parallel to the orientation of this discontinuity (31°/283° ± 13°). This postulated movement direction is further supported by structural indicators (Fig. 5.6). Vectors constructed perpendicular to extensional fractures suggest an average sliding direction of 290°.

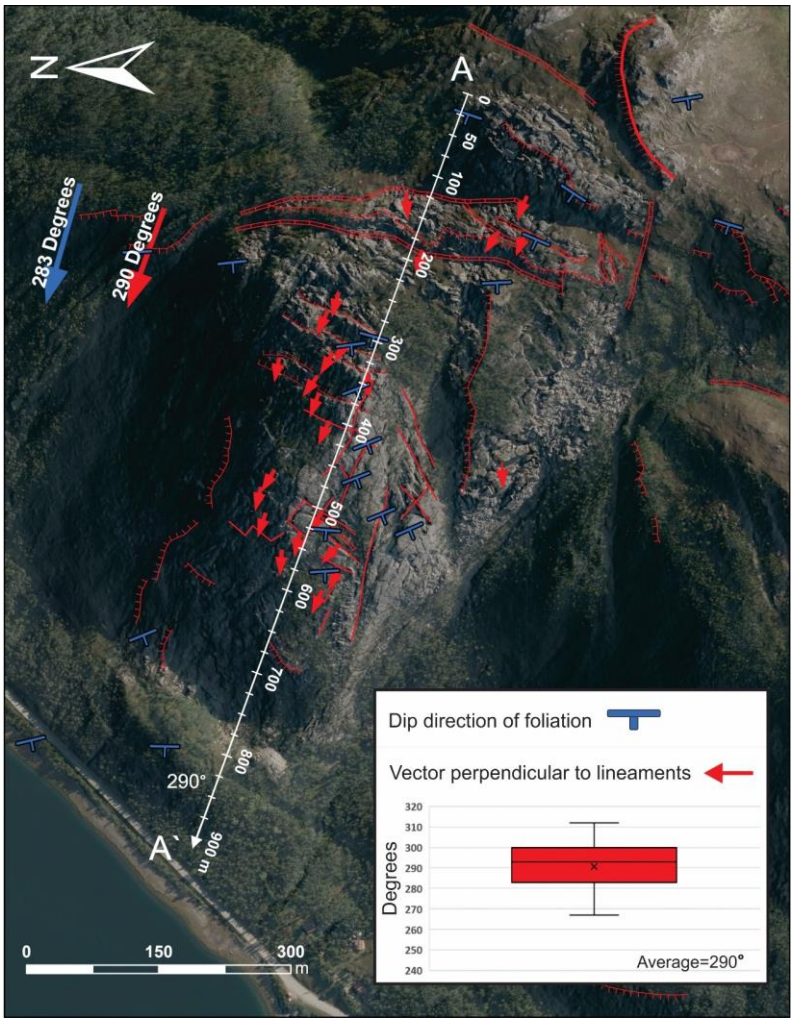

Figure 5.6: Sliding direction interpreted by structures. Red vectors are constructed perpendicular to extensional features and thus reveal the main stress axis (sigma 1). Big arrows in the upper-left corner indicate the average dip direction of foliation in in-situ bedrock (blue) and mean sigma 1 direction, i.e., extensional direction (red). Inset with box plot shows the variation in the measurements and the average orientation of the constructed vectors.

5.1.6 2D InSAR kinematics

Fig. 5.7 a, which shows combined 2D velocity, reveals that the highest velocities are found in the middle section of the slope. On average, the velocities within this section are between 2–4 mm/yr. However, some areas display higher velocities (up to 7 mm/yr), e.g., area along the northern limit. The vertical velocity (Fig. 5.7d) is generally between 2–3 mm/yr. The displacement is predominantly downward directed (into-slope), but a small area in the lower- and upper section has an oppositely directed displacement (out of slope). The horizontal velocity (E-W) (Fig. 5.7c) reveals a uniform displacement towards the west, but the magnitude varies. The vertical velocity and the horizontal velocity show matching patterns and distribution as the combined 2D velocity: increased velocities along the northern flank and an abrupt increase in displacement when crossing the two persistent trenches in the upper section. The dip of the combined 2D velocity vector (Fig. 5.7b) is steepest in the upper section (45–90° downward and west) and gradually decreases toward the middle section. There, the dip is relatively constant, around 30–35°. In the most distal part of the lower section, the dip is horizontal but also above the horizontal plane.

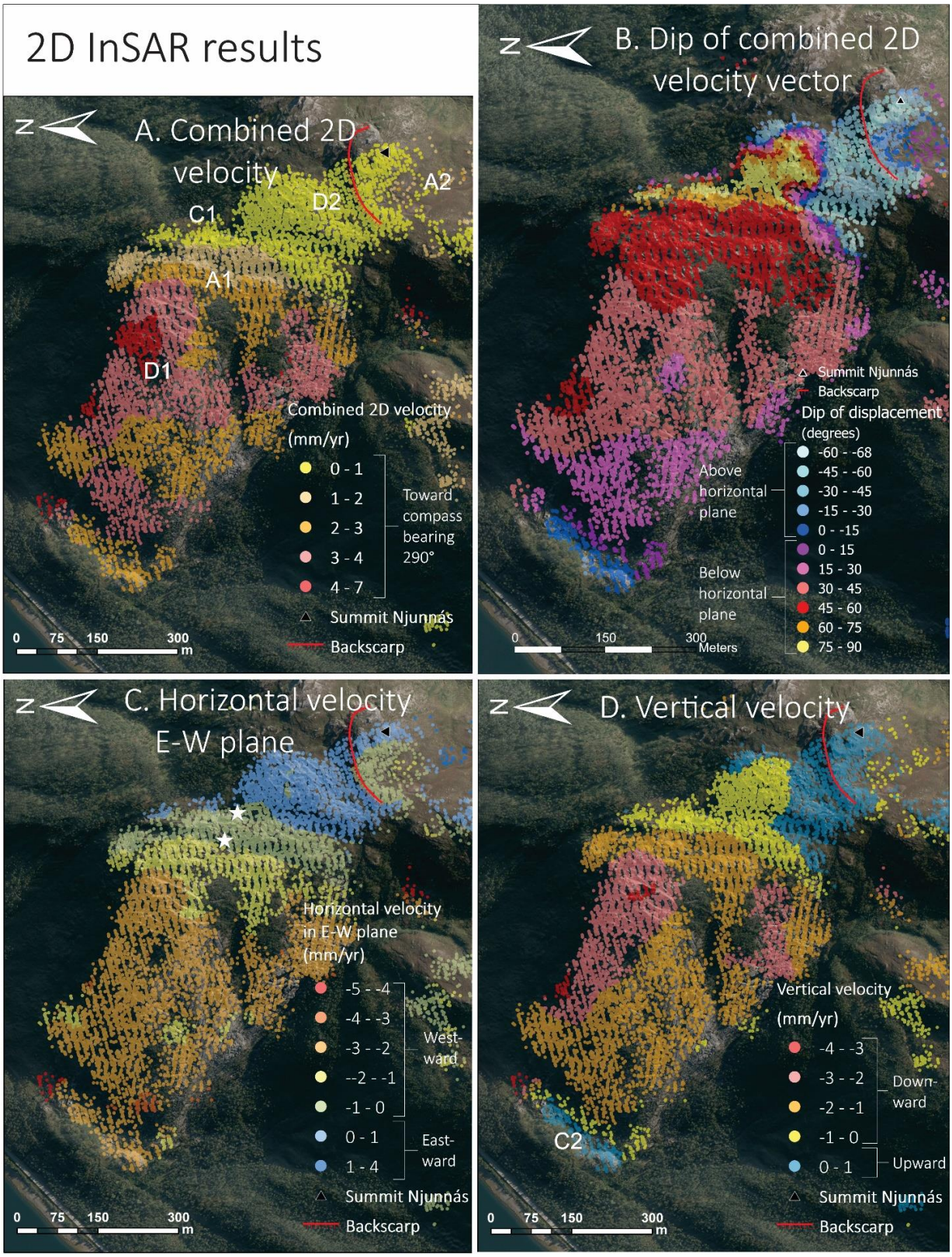

Figure 5.7: 2D displacement maps from Njunnás. Combined 2D velocity (A) and decomposed horizontal- (C) and vertical (D) components. The dip of the combined 2D displacement vector (B) shows if the displacement is under or over the horizontal plane. The transparent 2D InSAR results are draped over an orthophoto originating from NMA, 2020c.

5.2 Interpretation and discussion Njunnás

2D InSAR velocities for each superficial material class have been extracted and plotted in Fig. 5.8. The scatter plot of "soil without dense vegetation" (Fig. 5.8a) displays variations in both vertical and horizontal components. The largest values are in soil located in the middle section of the unstable area (A1 on Figs. 5.8a and 5.7a) and in close vicinity to the small ponds on the plateau (A2 on Figs. 5.8a and 5.7a). The displacement rates recorded on the plateau are assumed to be in connection with seasonal variations in water content, creating periods of subsidence and heave. This class also represents a geomorphological unit that is prone to frost action, leading to solifluction.

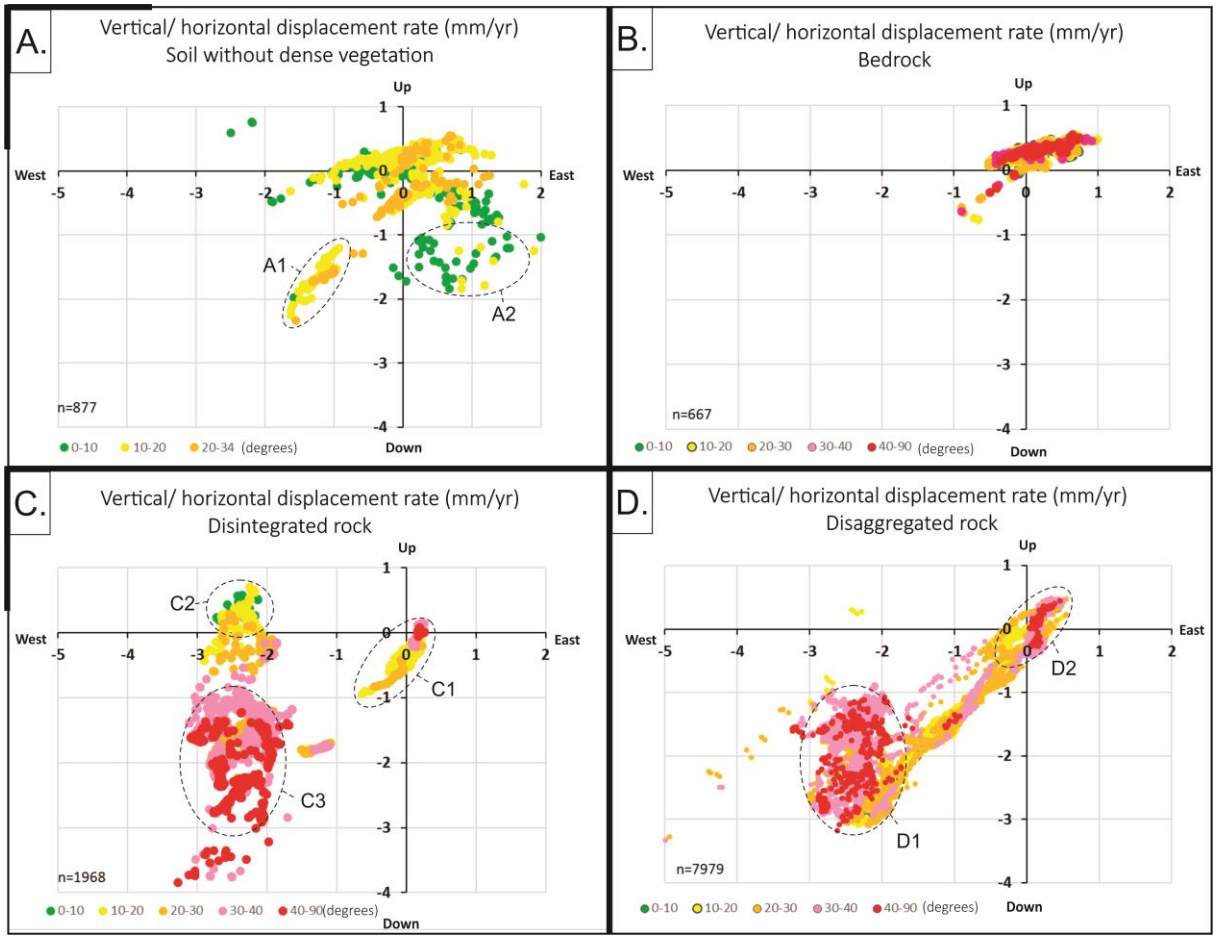

Figure 5.8: Displacement rates (vertical and horizontal) in four different geomorphological units. Slope inclination is attributed to each point and visualized with color.

The scatter points in the exposed bedrock unit (Fig. 5.8b) are clustered around zero, meaning that this class is mostly not moving. This result testifies that the superficial material categorization has been successful for this class and further that the InSAR data is well calibrated.

The scatter plot of the disaggregated class (Fig. 5.8d) shows that the displacement rates generally are in the order of a few mm/yr. The protruding displacement direction is west (80% of all scatter points) and downward (91%). The highest displacement rates are found in the middle section and in the upper part of the lower section (D1 on Figs. 5.8d and 5.7a). Towards the backscarp the displacement rates gradually decrease and reach its minimum directly underneath the postulated backscarp (D2 on Figs. 5.8d and 5.7a).

The displacement rate distribution in the disintegrated rock is similar to what observed in the disaggregated class. Both have a big cluster in the third quadrant, and the magnitude of the displacement is proportional (C3 on Fig. 5.8c and D1 on Fig. 5.8d). This similar pattern might imply that much of the observed displacement is due to the movement of the whole RSD and not individual loose blocks. Hence, much of the disintegrated class can potentially be used for evaluating the kinematics of the RSD. However, it should be used carefully since the displacement also seems to be more correlated to slope inclination. The lowest rates observed in this class (C1 on Figs. 5.8c and 5.7a) are material that has been transported to lower inclined areas outside the deforming area. Towards the transverse ridge in the toe zone, the vertical displacement is directed upward (positive values) (C2 on Figs. 5.8c and 5.7d). The slope surface is here flat and locally dipping in the opposite direction of the RSD. The observed displacement rates in this area are thought to be related to the RSD behavior and therefore implemented in the analysis of the RSD.

2D InSAR profile with geological interpretation

Fig. 5.9 shows 2D InSAR results with a tentative interpretation along profile A-A'. The geological interpretations presented previously in this chapter have been compared with 2D InSAR results in order to evaluate the observed kinematic pattern. The cross-section is oriented parallel to the inferred sliding direction and covers an area that has been extensively investigated in the field. The 2D InSAR profile is exploited for evaluating the spatial extent of the RSD (5.2.1), geometry of the basal rupture surface (5.2.2), and for evaluating variations in velocity (5.2.1).

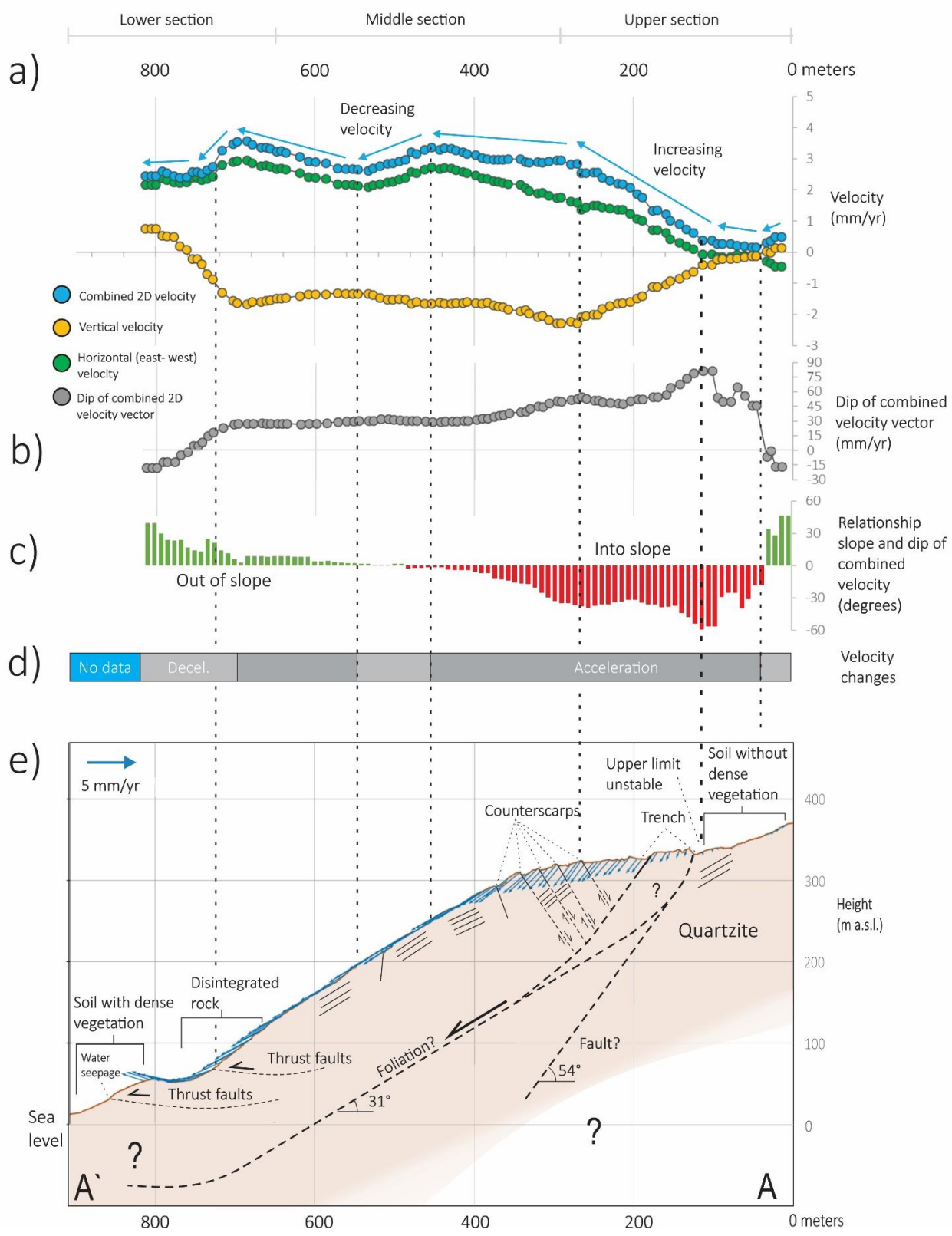

Figure 5.9: 2D InSAR result and geological interpretation in cross-section A-A'. a) and b) scatter plots of 2D InSAR results along the cross-section. c) The angle between the dip of the combined 2D velocity vector and the slope surface, indicates where the displacement is into the slope or out of the slope. d) Areas with accelerating and decelerating velocities. e) Geological interpretation and 2D InSAR results presented as blue vectors. The applied VIM for more precisely evaluating the depth and geometry of the basal rupture surface is presented in Appendix 3. The location of the profile is displayed in Fig. 5.6. Inspired by Eriksen et al. (2017).

5.2.1 Extent of the RSD

The backscarp of the RSD was identified as the uppermost scarp with no visible morpho-gravitational elements behind it. However, the 2D InSAR results reveal that this section is subjected to little or no deformation at the present date, which suggests that the upper limit of the deforming area (herein active major scarp) is located further downslope. A simultaneous and abrupt change in combined, vertical, and horizontal velocity is notable at ≈120 and 175 m along profile A-A' (highlighted with white stars on Fig. 5.7c). This corresponds to the location of two trenches, which potentially act as the active major scarp(s). The dip of these structures is measured and calculated to be around 54° towards NW (map view calculation using contour lines). However, this structural orientation does not coincide with any of the observed joint sets and may indicate another structure's presence. The lineaments located south from the locality, which were interpreted to be major faults, may possibly extend all the way to Njunnás (Fig. 5.10) and act as the rear limit. This assumption is further supported by dip measurements of the fault further south, which revealed a similar dip of approximately 49°. A fault-controlled rear rupture is not unlikely, as it was observed as the rear limit at Laksvatnfjellet, 10 km SW from Njunnás (Vick et al., 2020; Rasmussen, 2011). However, there are uncertainties related to this interpretation.

The toe of the RSD is difficult to determine with InSAR since the area is densely vegetated (Fig. 5.2). A decrease in velocity is observed at the end of profile A-A', which is expected in the toe zone and thus indicates that the daylighting basal rupture surface potentially is close. However, since we are unable to observe where the deformation completely stops (reaching zero displacement), it cannot precisely be determined. As highlighted by Fig. 5.9e, the toe could potentially be located in the fjord.

The transverse ridge located in the most distal part of the lower section may correspond to a compressional bulge since it is located in an area with slightly decreasing and upward-directed velocities. The ridge is covered with what is believed to be a thin veneer of ice-marginal glacial sediments. These sediments are likely transported englacially or supraglacially, rather than subglacially. This suggests that the ridge potentially is a result of the gravitational deformation, and not subglacial erosion and deposition. From the downslope facing side of this ridge, multiple streams are observed daylighting. This suggests the presence of persistent and wide discontinuities. These obviously dominating discontinuities may represent a daylighting failure surface.

The 2D InSAR results show abrupt and well-expressed lateral limits. However, these limits mainly correspond to the boundaries between dense vegetation and no vegetation. Hence, the 2D InSAR results are a little misleading and do not necessarily provide information about the outline of the RSD. The exact locations of the limits are, therefore, to a greater extent, dependent on morphological evidence. The indicative outline of the RSD (Fig. 5.2) is based on the spatial extent of disintegrated and disaggregated rock, in addition to mapped morpho-gravitational elements.

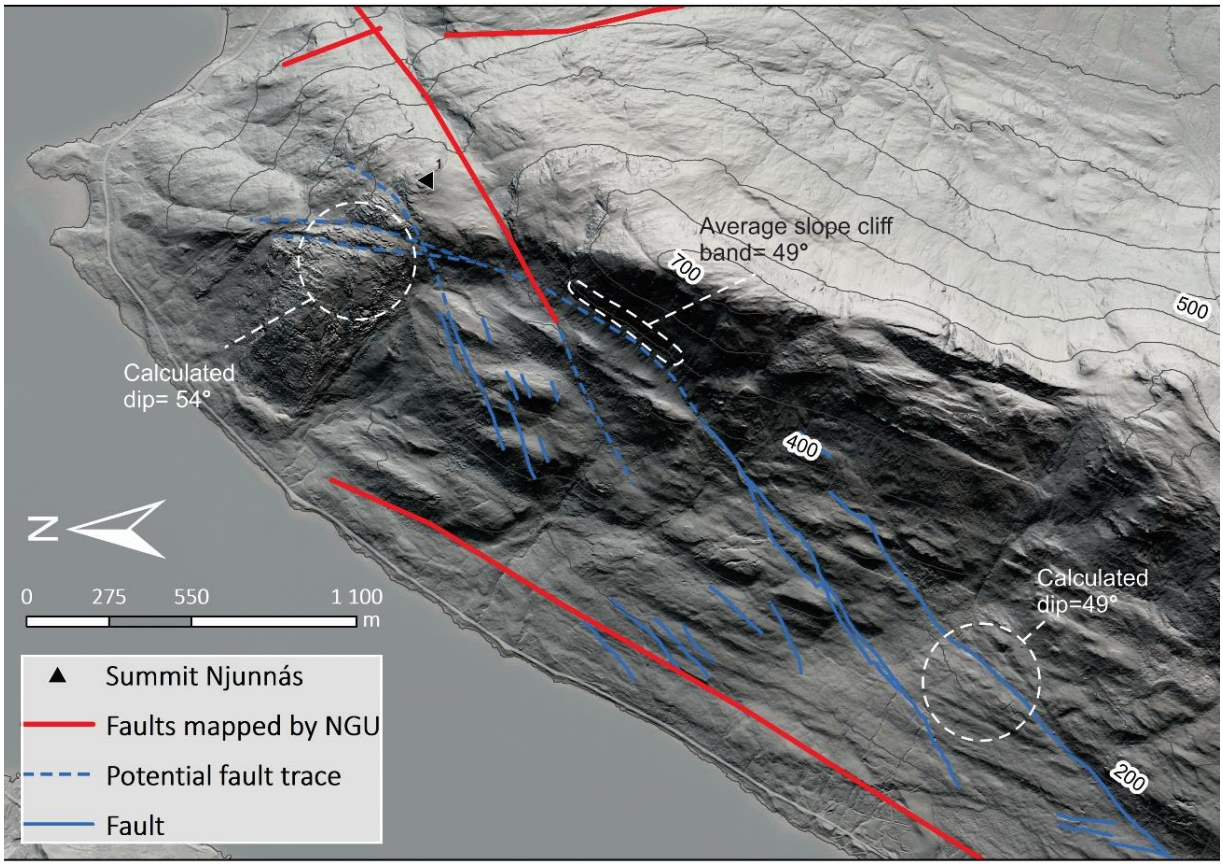

Figure 5.10: Hillshade showing the orientation of big-scale lineaments observed at Piggtind. Multiple NE-SW striking lineaments (inferred faults) are identified from orthophotos and created hillshades and verified in the field (blue lines). Such structures can be recognized from Skulvatindane in the south, to Njunnás in the north. Red lines indicate fault traces mapped on the 1:250000 bedrock map delivered by NGU (NGU, 2020b)

5.2.2 The geometry of the sliding surface

The rock slope stability assessment using kinematic analysis on structures measured in the field (Section 5.1.4) indicated that planar sliding was the most likely failure mode on Njunnás. Such sliding is inferred to occur along a planar failure surface in the upper and middle section of the slope, because of the approximately constant vertical displacement between 270–700 m along profile A-A'. A semicircular or circular failure surface is ruled out since it would result in

decreasing vertical velocity and increasing horizontal velocity, from top to bottom (Frattini et al., 2018). Furthermore, a circular failure surface would result in back-tilting of marker beds, e.g., foliation (Cruden & Varnes, 1996), which is not observed. A planar failure surface is supported by Frattini et al., (2018)'s simplified 2D finite elements modelling of translational movement, which highlights very similar patterns as the graphs presenting the vertical, total (combined), and horizontal displacement rates on Njunnás (Fig. 5.11). The dip of the displacement rates further reveals that the sliding most likely happens along the foliation. The average dip of displacement between 300 m and 700 m is approximately 31.5°. This precisely coincides with the average dip of the foliation in in-situ rock (31°).

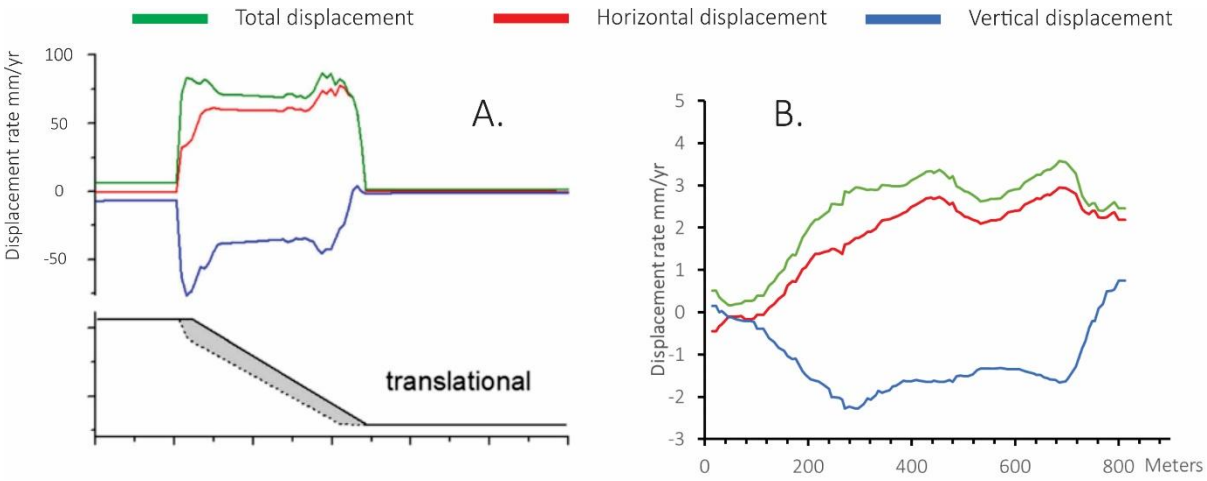

Figure 5.11: 2D displacement model of a translational slide based on a finite elements model from Frattini et al. (2018) (A.) and displacement rates from cross-section A-A' (B.).

At approximately 700 m along profile A-A', a marked decrease in the dip of the displacement is notable. From 700–825 m along profile A-A', the dip progressively decreases, culminating with a dip above the horizontal plane. This trend may insinuate that the basal rupture surface suddenly changes, i.e., the displacement is transferred to a new lower inclined structure or the foliation becomes sub-horizontal. After this abrupt transition, the horizontal component exceeds the vertical component, indicating that the displacement transpires along a gentler inclined structure. Fig. 5.2 reveals that the surface above this postulated transition zone is more disaggregated, i.e., higher fracture density. This is probably not a coincidence. As proposed by Stead & Eberhardt, (2005) and Braathen et al., (2004), a bi-planar or curved failure surface will result in a high strain prism with enhanced localized fracturing immediately above the transition zone (Fig. 5.12). The load from the upper part of the RSD (active sub-slab) drives the material located on the lower inclined failure surface in the toe zone (passive sub-slab), creating a prism of high strain in between.

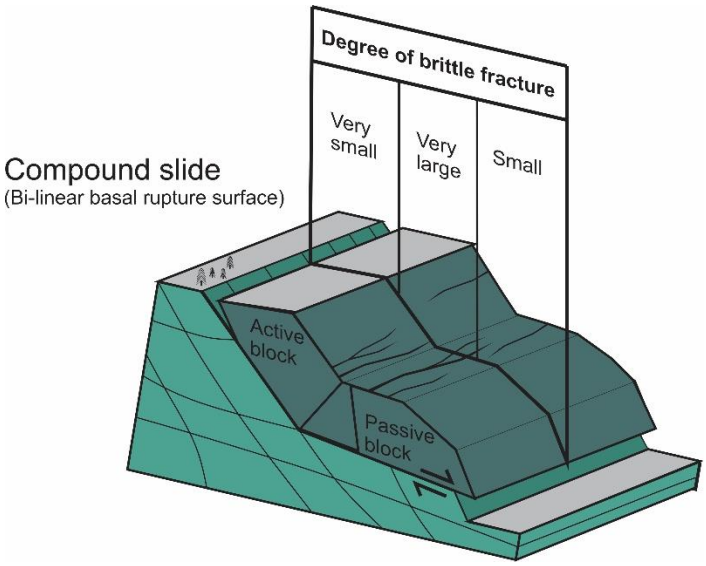

Figure 5.12: Compound slide and separation into an active and passive block. Spatial variations in brittle fracturing on the surface are highlighted. Inspired by Stead & Ebenhardt (2005).

5.2.3 Spatial variations in velocity and secondary structures

The upper section of the RSD is dominated by displacement into the slope, increasing velocities (acceleration), and successively steeper dip (Fig. 5.9a, b & c). All indicate an ongoing extension due to sliding and faulting. Multiple counterscarps have developed as a response to the internal deformation. The discrete antithetic fault planes (normal faults) divide the rock mass into multiple independent blocks and can be recognized as small offsets (e.g., ≈270m along profile A-A') in the combined 2D displacement graph. The highest observed vertical displacement rate on profile A-A' also corresponds to this section with closely spaced counterscarps. After this point, the vertical displacement rate progressively decreases. This small hinge point in the graph, is inferred to represent the approximate location of the intersection point between the structure creating the rear limit and the moderately inclined foliation (Fig. 5.9a & e).

The middle section contains zones of relatively faster and slower rates of displacement, which may indicate alternating stress regimes (Fig. 5.9a). The dip of the displacement is similar to the dip of the slope surface, indicating that there is little or no uplift or subsidence. This pattern changes further down the slide body as the slope surface slopes more steeply while the dip of displacement remains approximately constant. Fig. 5.7 a, c & d, show that an area along the northern edge has higher velocities compared to the main slide body. However, only the small cluster (D1 on Fig. 5.7a) has displacement rates that are significantly greater in magnitude compared to the surrounding area. The higher displacement rate is due to high vertical velocity, possibly related to the proximity to the counterscarps. However, the horizontal displacement is

uniform, which may indicate that this is not a separate slab and that the whole deforming area is moving as a homogenous body.

In the lower section, the displacement rates (both horizontal and vertical) decrease simultaneously as the dip of displacement progressively gets shallower. This indicates a transition to a compressive stress regime. In order to accommodate the high displacement rates from above, the energy must be transferred by other means. This is done by (1) incremental fracturing, which is visible at the surface as higher fracture density and disaggregated rock, and (2) thrust faulting. At least one exposed thrust fault is recognized in the lower section (≈720 m). It is characterized as a sudden drop in combined 2D velocity, and a spike in uplift followed by a marked decrease (less uplift). It is also plausible that another thrust fault outcrop below the transverse ridge (≈850 m). The presence of daylighting streams implies that dominating discontinuities outcrop here, but the lack of InSAR data prevents further interpretations.

6 Results and interpretation Piggtind/Skulvatindane

The chapter describes geomorphological and structural elements on Piggtind/Skulvatindane (6.1.1–6.1.4) and presents the generated 2D InSAR results (6.1.5). In Subchapter 6.2, the results are combined and interpreted, with the aim of characterizing the RSD, recognizing superficial slope processes and periglacial landforms, and describe the kinematic pattern of the rock glacier.

6.1 Results Piggtind/Skulvatindane

6.1.1 Morpho-gravitational analysis

The mountain flank below Piggtind/Skulvatindane contains some structures related to a gravitational deformation. However, the slope is dominated by talus material, which potentially obscures deep structures. This limits the ability to investigate the RSD from a geomorphological perspective.

The backscarp on Piggtind/Skulvatindane is well-expressed and clearly demarcates the upper limit of the RSD (Fig. 6.1). This NNE-SSW striking structure can be traced all the way to Lakselvnesåsen and is in certain places 70 m high. In the southern section, a counterscarp immediately succeeds the backscarp, and together they form a double-crested ridgeline. A large displaced terrace is present below the backscarp. Its width increases progressively towards Lakselvnesåsen and is in certain places segmented by backscarp-parallel trenches. The middle section of the slope contains fewer structures unambiguously related to a gravitational deformation than at a higher elevation. However, especially in the southern part, some trenches and scarps are observed. This area also contains an assemblage of terraces that forms a stepped slope surface. A large NW-SE striking fault is located in the southern part of the locality and appears on the surface as a large gully. Multiple faults are also observed in the toe zone, striking NNE-SSW. The figure also shows lobated features (purple lines on fig. 6.1), which might be attributed to periglacial landforms. Small-scale lobes may correspond to solifluction lobes, while larger lobate-shaped ridges are possibly connected to the rock glacier. It is evident from the figure that small lobes are mainly confined to areas above 400 m a.s.l., while larger lobes are found as low as 300 m a.s.l.

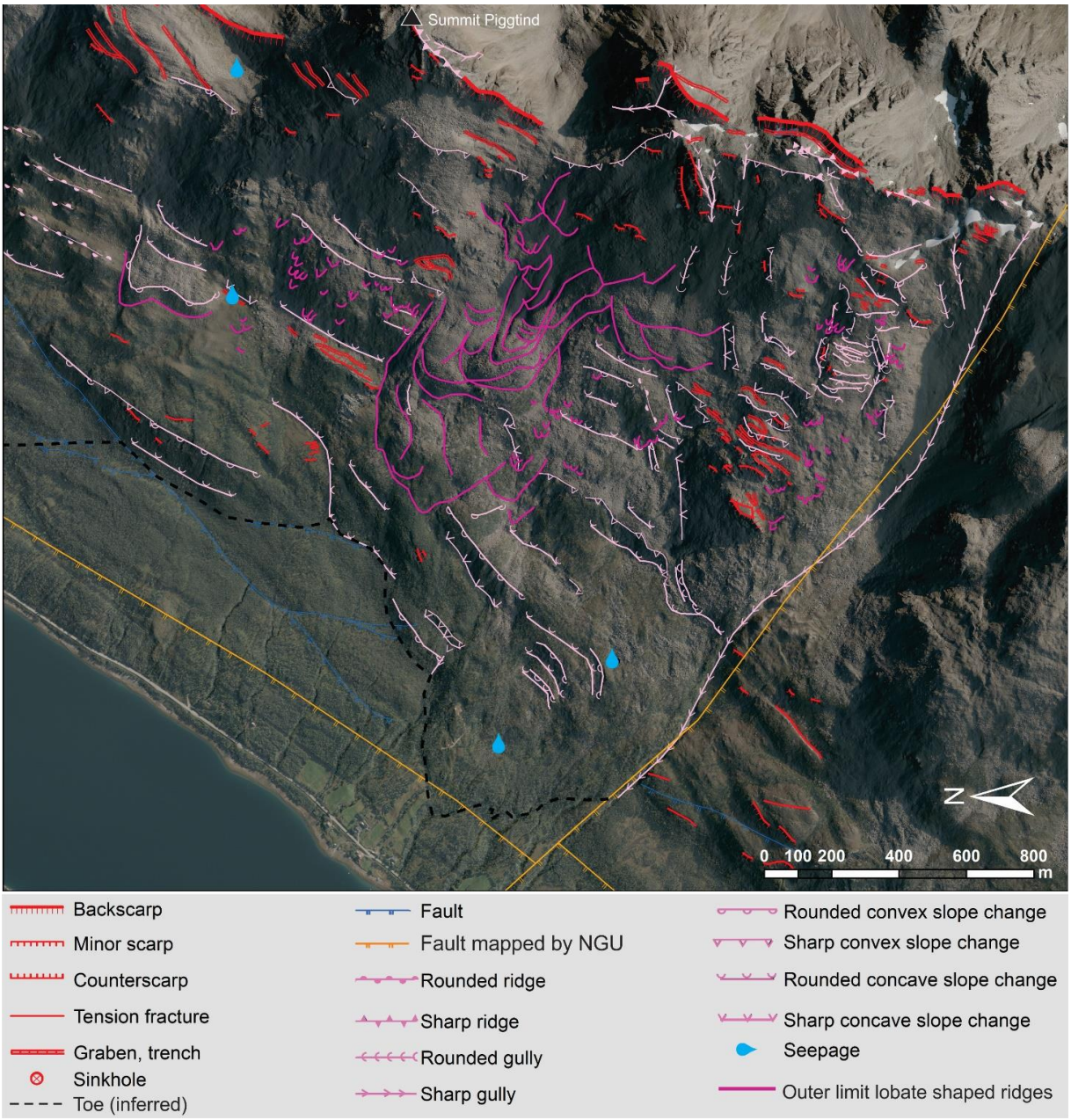

Figure 6.1: Morpho-gravitational map of Piggtind/Skulvatindane. Faults mapped by NGU origin from the National bedrock database (Bedrock (ngu.no) with resolution 1:250 000 (NGU, 2020b). Background: orthophoto 2016 (NMA, 2020c).

6.1.2 Superficial/surficial material categorization

The superficial/surficial material categorization presented in Fig. 6.2 shows that most of the middle- and upper section of the slope is draped with disintegrated rock related to the gravitational deformation. Only small isolated patches of disaggregated rock are observed. However, this latter unit is more frequently mapped in close vicinity to the backscarp, i.e., on the displaced terrace. Soil without dense vegetation is mainly confined to smaller areas in the south, but the spatial extent is greater in the lower section and northern part of the locality

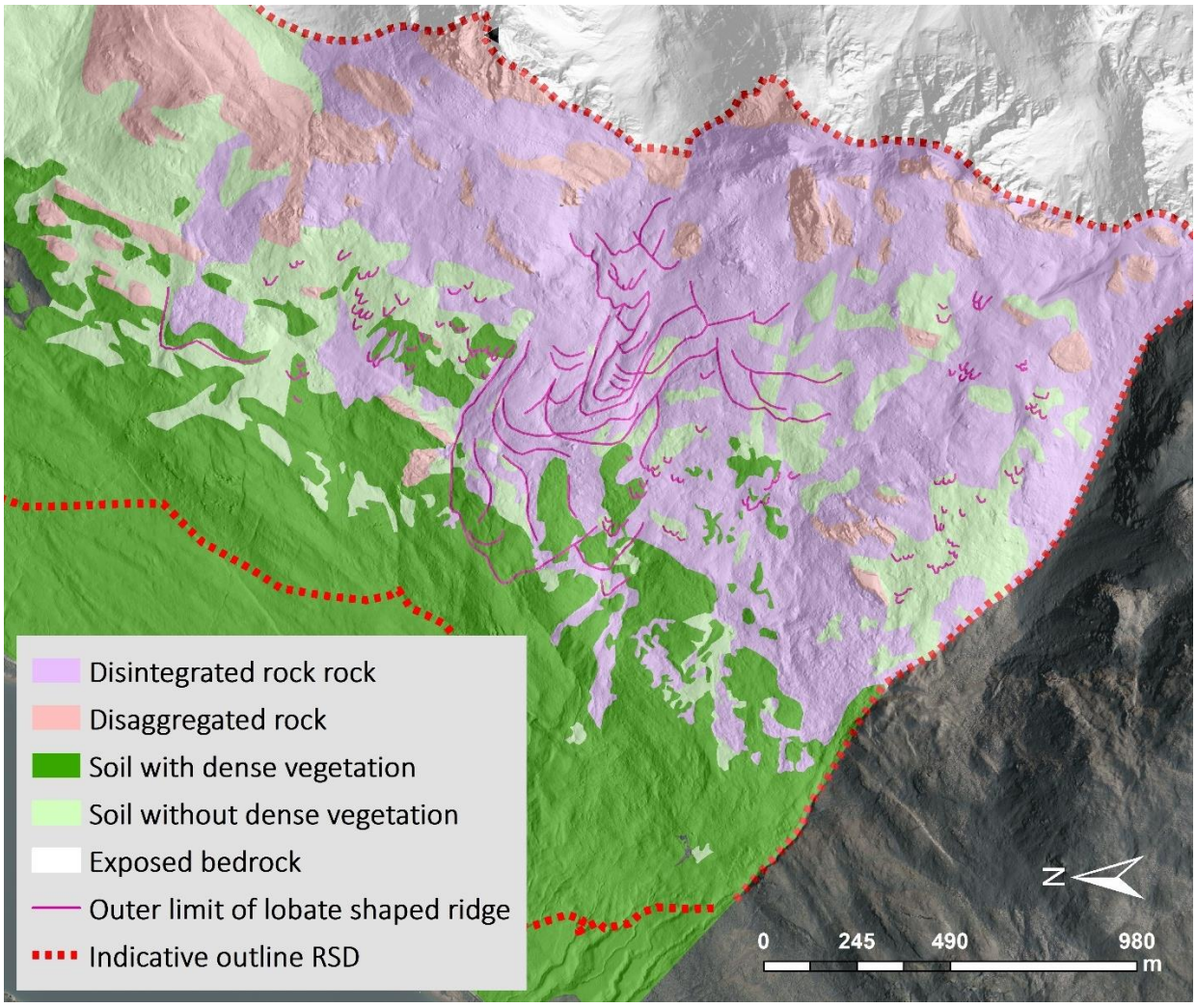

Figure 6.2: Superficial/surficial material categorization of Piggtind/Skulvatindane. Purple lines indicate lobate-shaped features, possibly related to periglacial landforms, i.e., rock glacier and solifluction lobes. The indicative outline of the RSD (red dashed line) is determined by the spatial extent of disintegrated- and disaggregated rock, in addition to observed morpho-gravitational elements (Fig. 6.1).

6.1.3 Structural analysis

The stereographic projection displayed in Fig. 6.3a shows that the average dip and dip direction of the foliation in bedrock with few or no morpho-gravitational elements is 29/288° ± 14°. This means that the foliation is moderately inclined towards the fjord, however steeper than the slope surface (24/294°). Within the inferred deformation area (Fig. 6.3b), the orientation and dip of the foliation exhibit a slightly higher variability. The stereographic projection also shows that multiple measurements indicate a lower inclined foliation (close to origo). The average dip is steeper than in-situ bedrock, but the orientation is similar (40°/290° ± 15°). It should be emphasized that the sampling distribution is uneven, especially in the inferred in-situ bedrock. No exposed bedrock is observed in the toe zone of the locality, and consequently, no orientation measurement was made in this area.

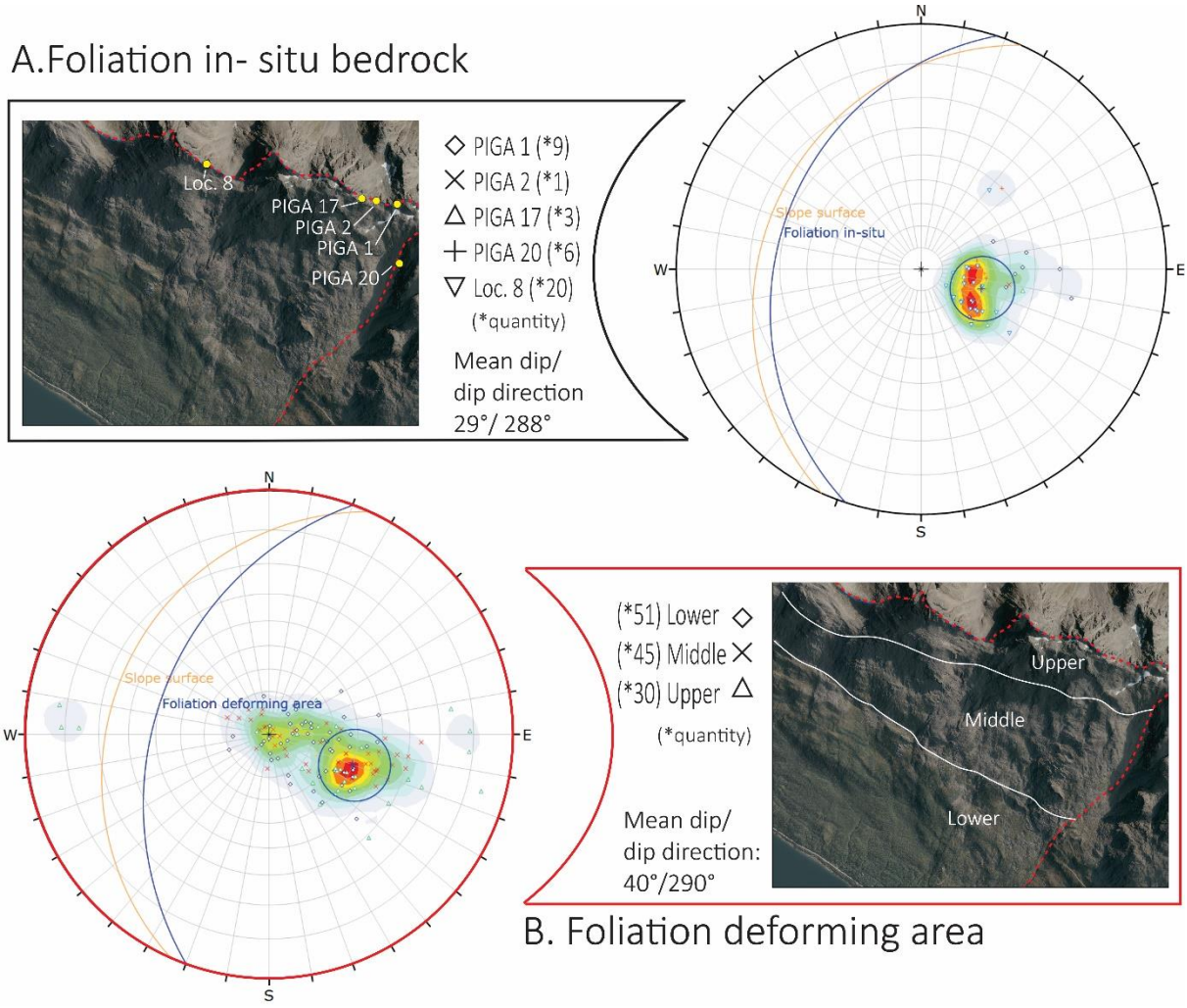

Figure 6.3: Stereographic projection of foliation measurements from (A.) exposed bedrock with rather few or no morpho-gravitational structures (inferred to be stable localities) and (B.) from bedrock in areas with abundant morpho-gravitational structures (inferred to be actively deforming). The average orientation of the slope surface is displayed with orange color (24°/294°). The structural measurements are presented in an equal angle projection of the lower hemisphere. 1 σ variability cone (circle) are displayed with similar color as the mean plane.

The stereographic projections presented in Fig. 6.4 show the orientation of joint planes within the inferred deforming area (B.) and outside the deforming area (A.) From the stereographic projection, we recognize three distinct joint sets, and it seems to be no significant disparity in orientation between joints sets recorded outside and inside the deforming area. However, it should be emphasized that some of the joint sets are less significant in the stereographic projection of in-situ data (low pole density). This is potentially related to a sampling bias since all joint sets are recognized in the field.

JN1 is the most frequently observed set, as demonstrated by the increased pole density on Fig. 6.4 a and b. The average orientation is 50–60° towards ESE, which coincides with many of the

mapped morpho-gravitational structures such as minor scarps and trenches. JN2 and JN3 are both dipping almost vertically. Within the deforming area, JN2 falls towards NNW and JN3 towards SSW. Outside the deforming area, the dip direction is opposite for both sets. However, it should be underlined that the dip direction is ambiguous with dip values close to 90°.

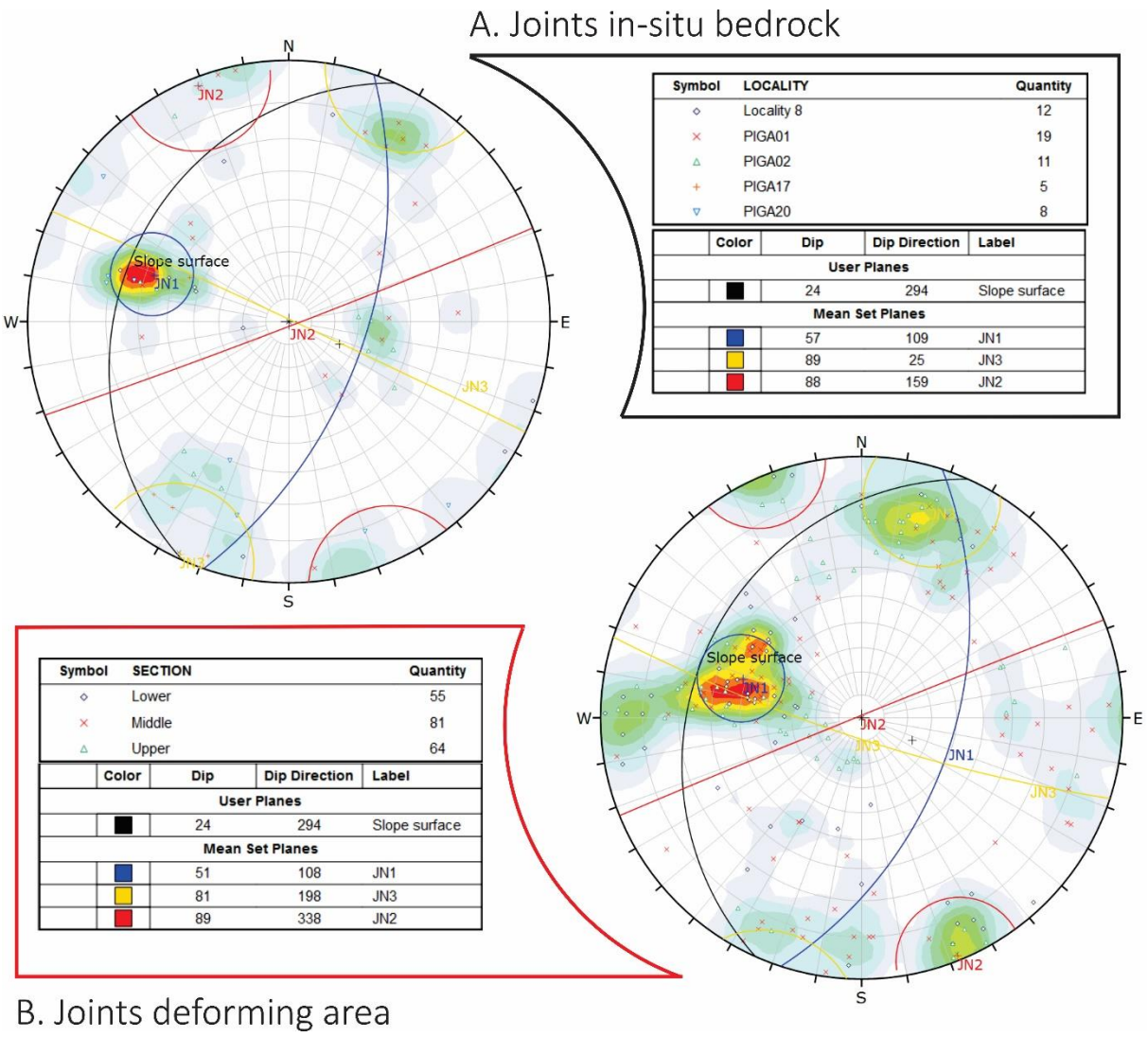

Figure 6.4: Stereographic projection of joint planes from (B.) the inferred deforming area, and (A.) stable in-situ bedrock. The structural measurements are presented in an equal angle projection of the lower hemisphere. The location of the localities/sections is presented in Fig. 6.3. 1 σ variability cone (circles) are displayed with similar color as the mean planes.

6.1.4 Rock slope stability assessment using kinematic analysis

The kinematic analysis on Piggtind/Skulvatindane is performed with 94 orientation measurements from outcrops displaying few or no morpho-gravitational structures, i.e., inferred in-situ bedrock. The same conservative friction angle of 20° and lateral limit presented in Section 4.2.1 is also applied to this locality. The slope properties, i.e., aspect and inclination, are calculated as average values in addition to the standard deviation (24°/294° ± 6°/29°).

The rock slope stability assessment using kinematic analysis reveals a potential for planar sliding and wedge sliding, but flexural toppling is highly unlikely. 6.38% of all foliation measurements fall within the critical zone (Fig. 6.5a). All of which are foliation measurements and thus, indicate that this discontinuity best matches the conditions required for planar sliding. Wedge sliding shows a proportional low score, with only 4.99% critical intersections (percentage of all discontinuities) (Fig. 6.5b). According to the analysis, a wedge slide can potentially develop along the intersection line of the foliation and JN2 (22°/248°) and/or the foliation and JN3 (28°/296°). Failure along foliation-JN3-wedges is considered more likely, as the percentage of critical intersections is 13.11% contra 0.32% for foliation-JN2-wedges. Flexural toppling is regarded as unlikely since none of the collected discontinuity measurements plots is within the critical zone of this mechanism (Fig. 6.5c).

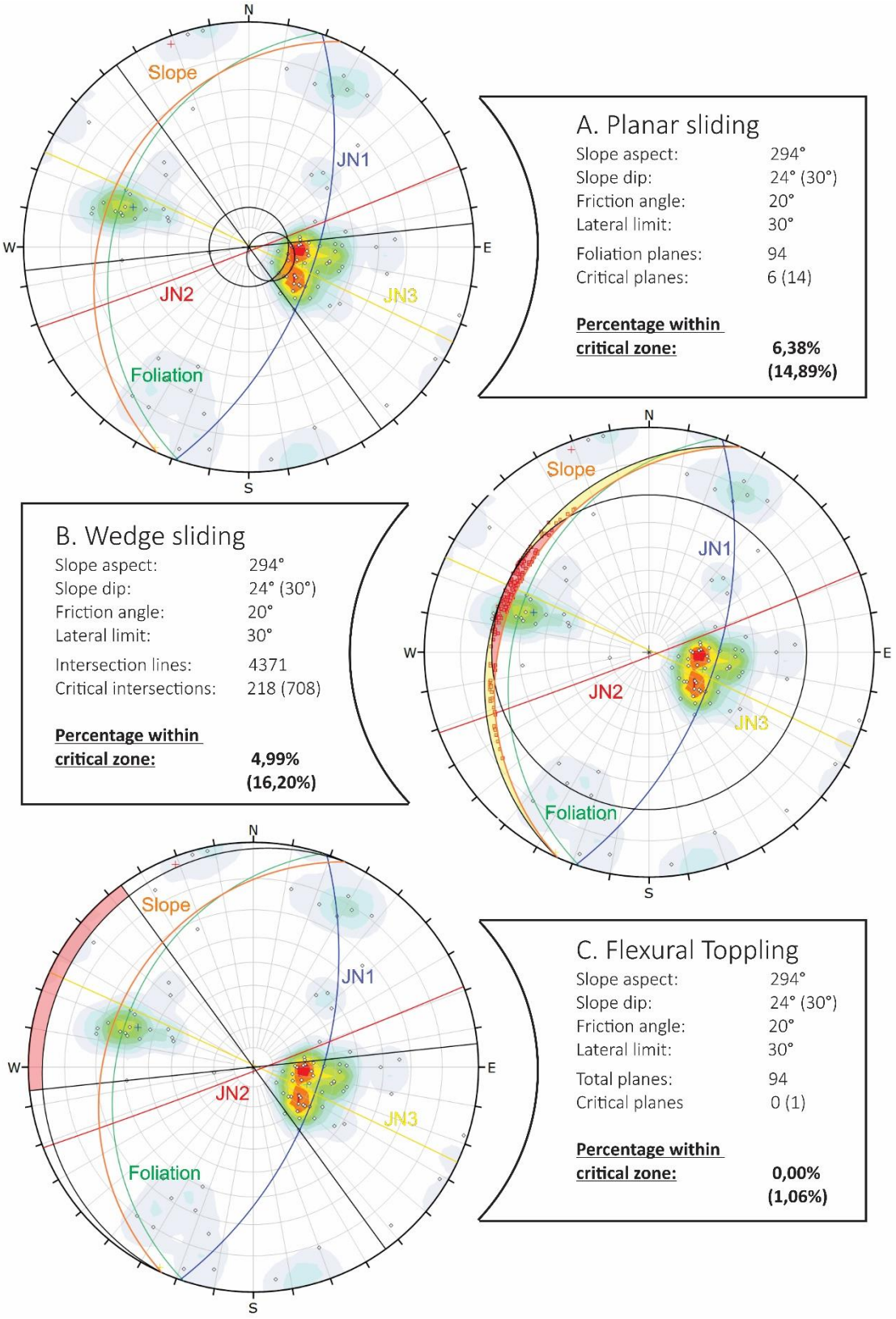

Figure 6.5: Results from the kinematic analysis performed in Dips. The structural measurements are presented in an equal angle projection of the lower hemisphere. The average orientation of the foliation and the three joints sets presented in Section 6.1.3, are also displayed.

6.1.5 2D InSAR kinematics

We see from Fig. 6.6a that the highest combined 2D velocities are found in the area with the mapped lobate-shaped ridges (up to 157 mm/yr) (large red cluster around “B.” on Fig. 6.6a). The velocities are considerably lower in magnitude both south and north of this area. On the northern side, the transition is sharp, going from 5 mm/yr to 40–70 mm/yr. On the southern side, the transition is gentler, and the rates are generally in the order of a few cm/yr. A conspicuous velocity change is observed in the southernmost part of the locality and coincides with the NW-SE striking fault presented in Section 6.1.1 (displayed as a dotted red line on Fig. 6.6).

The dip of the combined 2D velocity vector presented in Fig. 6.6b shows that the steepest dip is mainly confined to the upper section, such as the displaced terrace (45–50°). The dip angle gradually decreases further down the slide body and is on average around 30–45° in the middle section. However, the magnitude of the dip is not entirely uniform. For instance, a steeper dip is observed in the area with mapped morpho-gravitational elements in the southern part (Highlighted with an “A” on Fig. 6.6b). A marked reduction in dip can be observed in the toe zone, where the displacement eventually becomes mostly horizontal with a pronounced upward movement.

Fig. 6.6e shows slope inclination minus the dip of the displacement (in degrees). The slope's upper- and middle sections generally have a downward directed displacement (into the slope). This is opposite of what we observe in the toe zone, where the displacement on average is out of the slope. The figure also reveals that a large fraction of the slope experience dip of displacement parallel to the slope.

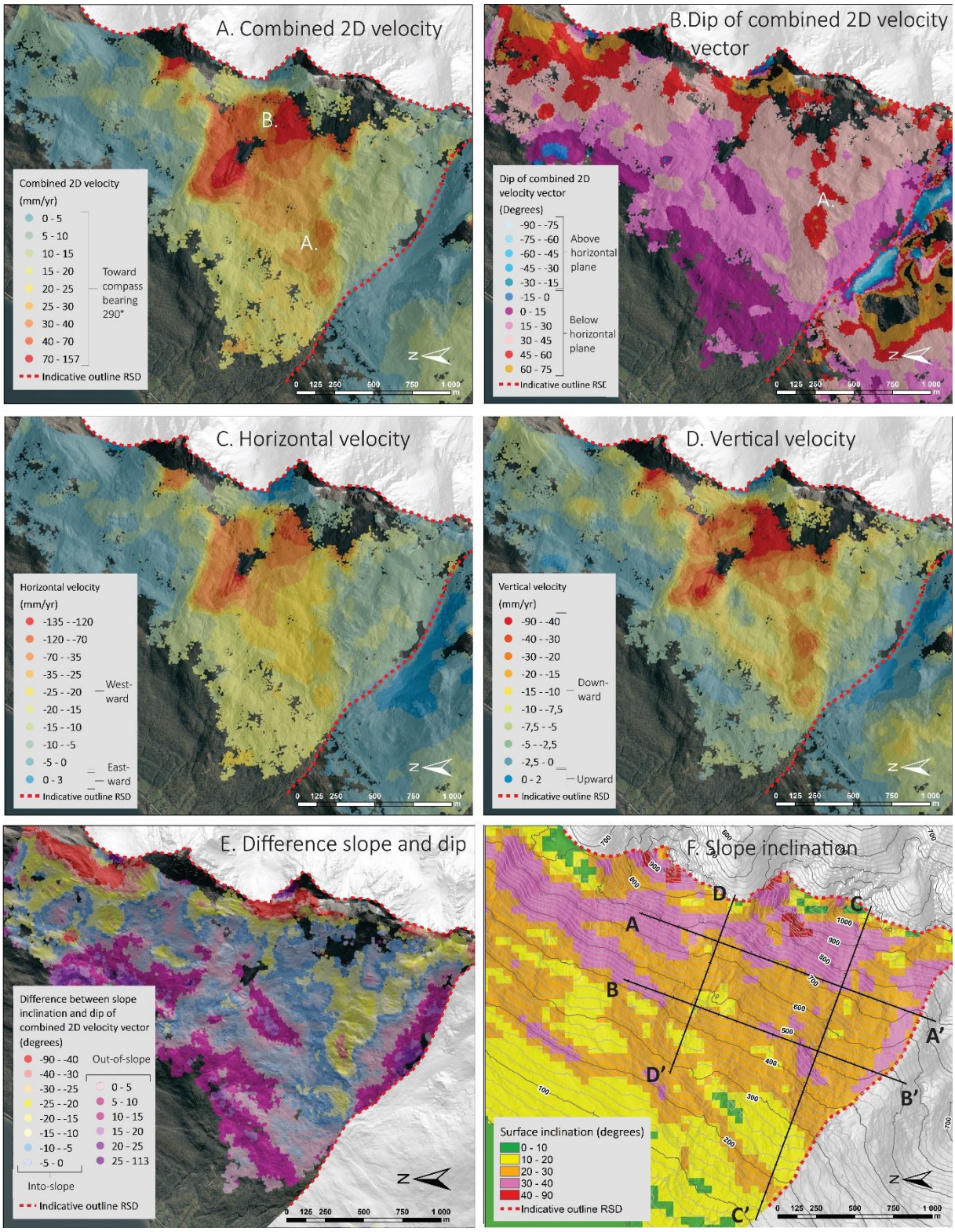

Figure 6.6: 2D displacement maps of Piggtind/Skulvatindane (A, B, C, and D). The difference between the slope inclination and dip of displacement indicates where the combined 2D displacement is into- or out of the slope (E.), and slope inclination map with a 50 m resolution showing the location of profiles used in the interpretation (F.). Results from behind the backscarp are removed to highlight the deforming area.

6.2 Interpretation and discussion Piggtind/Skulvatindane

6.2.1 Identifying and delimit slope processes

Piggtind/Skulvatindane displays a composite morphology due to a complexity of overlapping slope processes, including an RSD, periglacial landforms (rock glaciers and solifluction features), deformation of postglacial deposits from fast-moving landslide processes (Figs. 6.7 and 2.6). All of which leads to ground displacement, however, with different displacement behavior. To evaluate the kinematics of the RSD, the individual slope process must first be recognized and delimitated. Superficial slope processes are in certain areas superimposed on the RSD, meaning that the observed displacement with 2D InSAR potentially reflects two slope processes working simultaneously. Furthermore, the superficial displacement may in certain areas be so extensive that it overprints the kinematics of the RSD. In the following section, I attempt to classify the various slope processes based on the fundamental differences in morphology and kinematics described in Section 4.3.

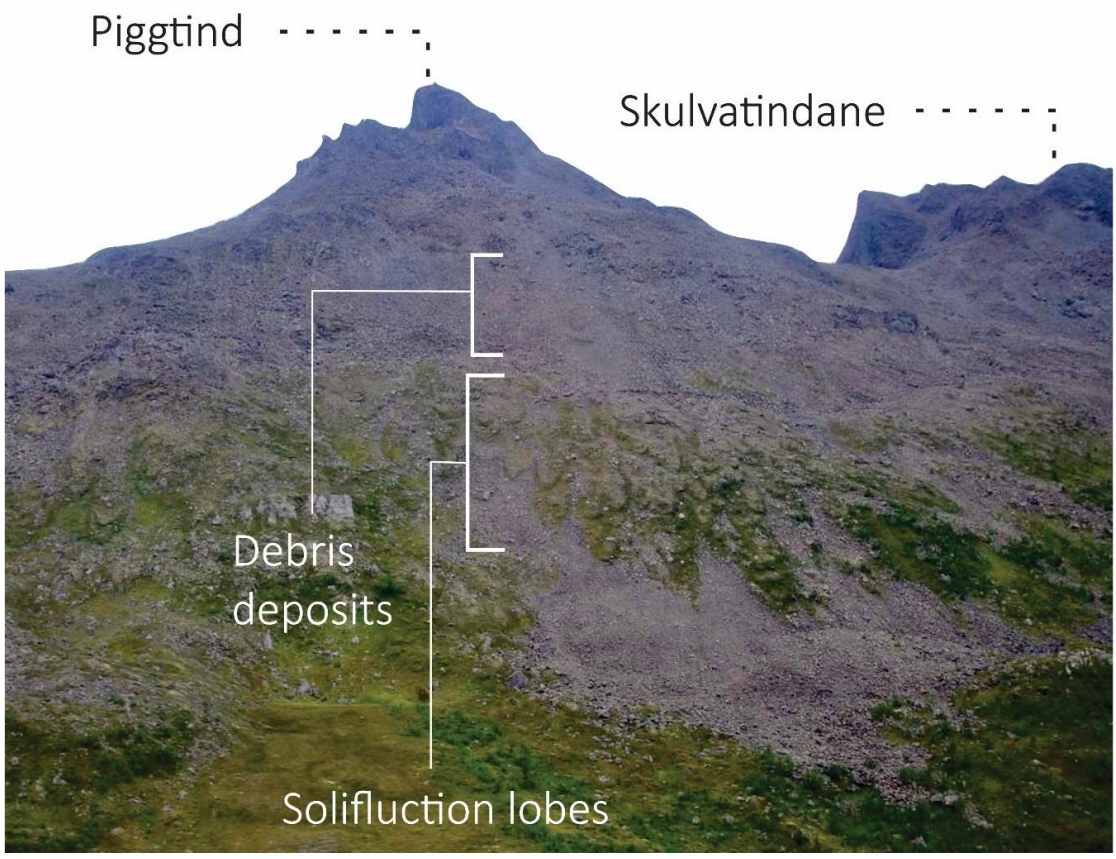

Figure 6.7: Photography showing the slope underneath the summit of Piggtind. The surface is extensively covered with disintegrated rock and soil without dense vegetation that is affected by solifluction. Photo direction: ESE. Photo: Martina Böhme (NGU).

Spatial extent rock glacier and RSD

Active rock glaciers have a characteristic surface expression with flow lines, lobes, ridges, furrows, little vegetation, and steeply dipping fronts (Singh et al., 2011; Wang et al., 2017). All these features are identified underneath Piggtind/Skulvatindane and partly allow the delimitations of the rock glacier complex to be determined. However, the flank contains much talus material, and the site is dominated by rounded morphostructures and lobes potentially developed by various slope processes.

Fig. 6.8, which present two 2D InSAR profiles (A-A' and B-B') that crosscut the approximate location of the rock glacier complex, reveals considerably higher displacement rates in the area with the mapped lobes (Fig. 6.1). The abrupt increase in velocity coincides with mapped geomorphological elements and is therefore inferred to mark the outer limit of the rock glacier complex. Furthermore, the outer limits are in certain areas identified as a sharp change in angle between dip of displacement and slope inclination, indicating a transition from a deep deformation to a superficial slope process.

The backscarp on Piggtind/Skulvatindane is well-expressed (Fig. 6.1) and can be traced to Lakselvnesåsen. This insinuates that the entire flank is, or has been, subject to a rock slope deformation. The superficial/surficial material categorization (Fig. 6.2) also supports this spatial extent, as units related to the RSD (that is, disintegrated- and disaggregated rock) can be observed in the upper and middle section of the slope all the way to Lakselvnesåsen. The southern lateral limit of the RSD was identified from the 2D InSAR results as an abrupt decrease in velocity (Fig. 6.6). This limit corresponds to an NW-SE striking fault, which is believed to have formed during the rifting of the Norwegian margin (Bergh et al., 2007). The toe of the RSD is recognizable on hillshades and expressed as sudden bulges (60 m a.s.l. in the south and 180 m a.s.l. further north). Multiple NNE-SSW and N-S striking faults segment the toe zone but disappears when intersecting with the RSD-related bulges (Fig. 6.1).

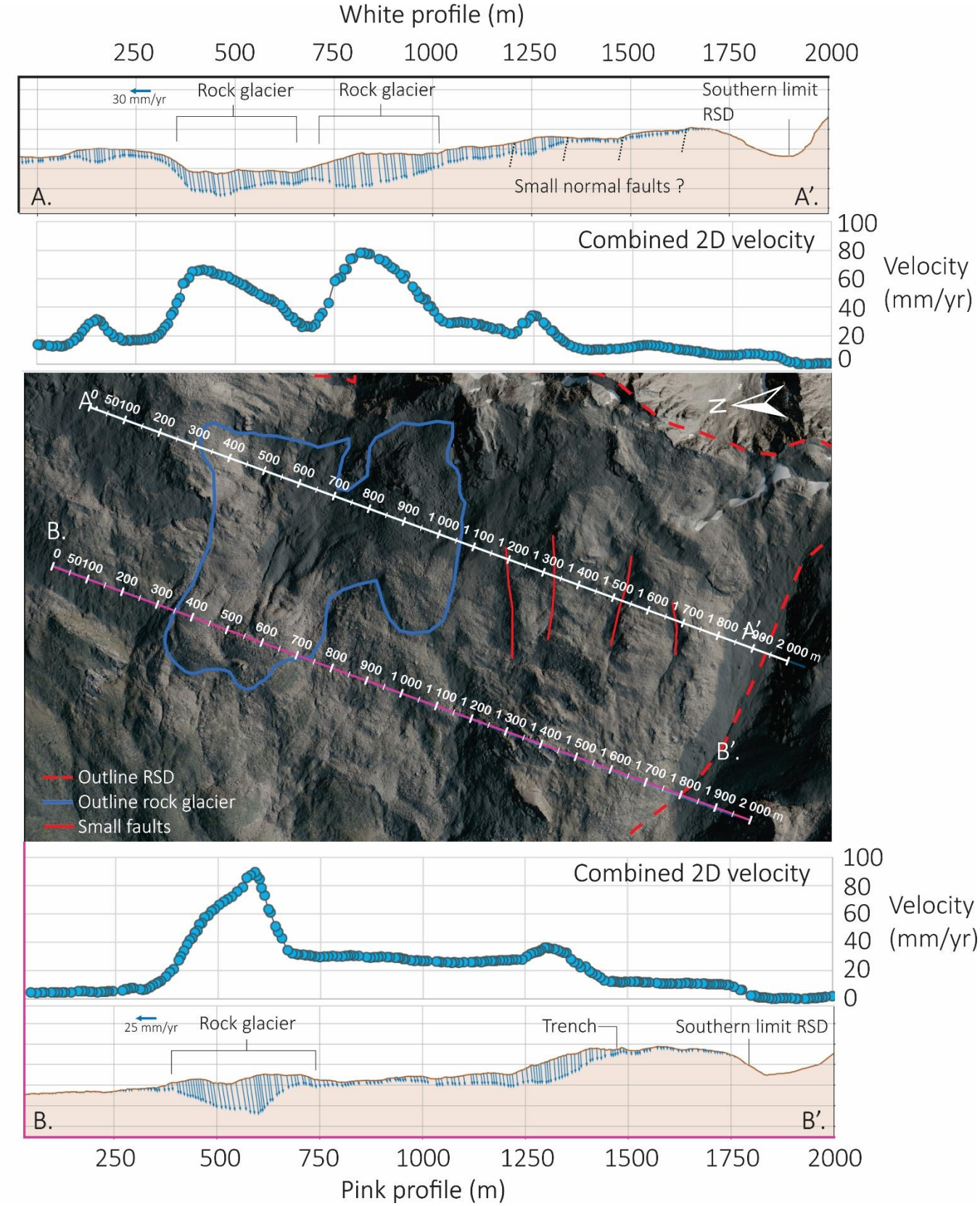

Figure 6.8: 2D InSAR profiles and geological interpretation. Both profiles (Profile A-A' displayed in white and B-B' displayed in pink) are attributed a topographic cross-section and a scatterplot showing the variations in combined 2D velocity.

Identifying superficial displacement

The scatter plot of the disaggregated unit (Fig. 6.9d) shows that the displacement predominantly is downward and west. The magnitude of the displacement is generally around 10 mm/yr; however, some areas display horizontal- and vertical velocities in the order of 30 mm/yr (A and B on Fig. 6.6a). There seems to be little or no correlation with slope inclination, which suggests that deeper structures control the displacement. This is further evidenced by the fact that the dip of the displacement on average is much steeper than the slope surface (Fig. 6.9e).

The scatter plot of the rock glacier complex shows that the displacement rates within this unit are considerably greater in magnitude compared to the three other units. The highest velocities are found in the center of the main lobe (500 m along profile B-B') and further upslope close to the edge of the terrace. The largest vertical velocities (B1 on Fig. 6.9b) are located in the latter area, where the slope inclination is at its steepest within this unit. In the main lobe, the horizontal velocities are close to 140 mm/yr (B2 on Fig. 6.9b). The scatter plot further reveals that very few CSD points have a vertical- or horizontal component smaller than 10mm/yr. This is an interesting observation because most of the disaggregated unit shows velocities in the order of 10mm/yr. This might insinuate that the rock glacier is superimposed on the RSD. Hence, the lowest displacement rates within this unit can be no less than the velocity of the RSD. This interpretation is also supported by the results from the morpho-gravitational analysis, which revealed that morpho-structures related to the RSD, existed at both higher and lower elevations with regards to the rock glacier. The boxplot, which shows the difference between the dip of displacement and slope inclination, reveals that the angle generally is small (average ≈-5°). This may imply that the displacement mostly follows the surface topography.

Disintegrated rock, soil without dense vegetation, and disaggregated rock show a similar displacement pattern with approximately comparable rates (Fig. 6.9a, c, and d), which potentially could indicate that the displacement rates represent the underlying slope deformation. However, the boxplots in fig. 6.9e reveals that the angle between the dip of the 2D velocity vector and slope inclination on average is small in the soil- and disintegrated units, which could indicate that the displacement is controlled to some extent by the surface topography. This is also evidenced by the high presence of lobes and individual 2D InSAR points that exhibit significantly higher velocities. Because the disaggregated unit is underrepresented in the middle- and lower part of the slope, it would be of great benefit to identify and separate 2D InSAR results from the two units that can be attributed to the RSD.

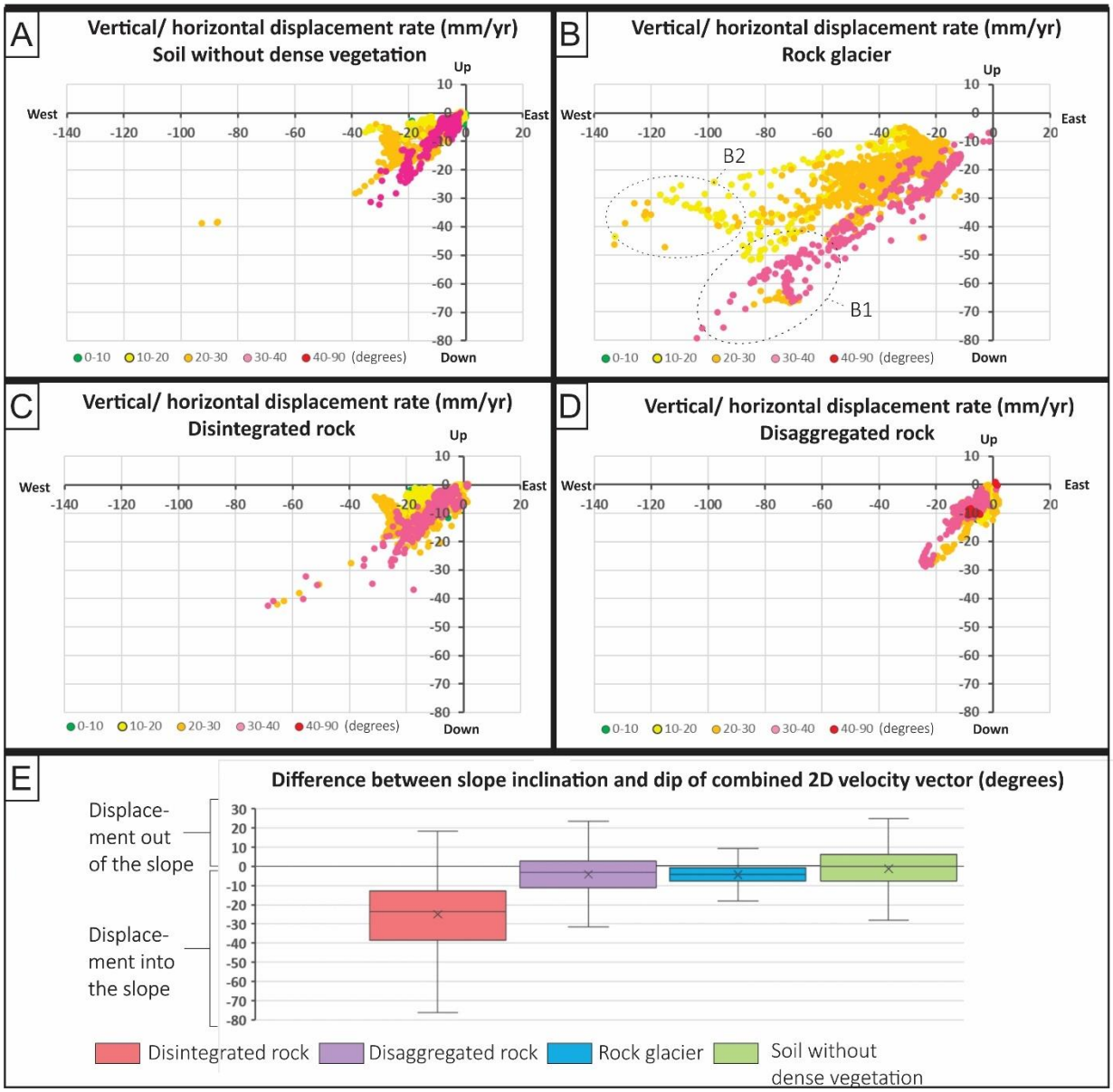

Figure 6.9: Scatter plots showing vertical and horizontal velocity for 2000 randomly chosen pixels for four geomorphological classes (A-D). The difference between slope inclination and the dip of the combined 2D velocity vector (in degrees) (E.). A random selection of points has been considered necessary because of the large size of the original data sets.

The disintegrated unit, which represents all areas covered with loose unconsolidated debris, is susceptible to superficial deformation. The dip of the displacement is then expected to be approximately similar to the surface inclination, however, naturally exhibiting some variability. Determining this variability is arduous, and little literature exists on this topic. Furthermore, considering that the locality potentially consists of composite processes, the observed kinematic pattern may be difficult to predict. However, a conservative threshold of >-5° and <5° is applied and thought to segregate areas/2D InSAR results dominated by superficial displacement. An

exception is made for areas with obvious morpho-gravitational structures (Vick et al., 2020) and low slope inclination (<15°), i.e., terraces, since these areas are thought to reflect the kinematics of the RSD.

The unit soil without dense vegetation is susceptible to solifluction and can therefore not be included without further examination in the analysis of the RSD. The difference between dip of displacement and slope inclination in mapped solifluction lobes is on average 0.5° (Appendix 4b), indicating that the displacement follows the surface. The combined 2D velocities in these features are on average higher than the observed displacement in disaggregated rock, suggesting an additional contribution in displacement from the solifluction features (Appendix 4a and 5). Because of these two observations, all mapped lobes are excluded from the analysis of the RSD. Furthermore, areas without visible lobes may also be affected by solifluction since they can operate in sheets where the topography is more uniform (Matsuoka et al., 2001). Suppose that the observed difference between dip of displacement and slope inclination in the mapped solifluction lobes are representative for unidentified features, 6,7 to -4,5° (minimum and maximum value for solifluction lobes) (Appendix 4b) can be used as a threshold for identifying other areas influenced by solifluction.

The superficial/surficial material categorization separated areas with soil by the density of vegetation. This was done to identify areas especially susceptible to solifluction and potentially explain the absence of displacement information. However, areas mapped with dense vegetation do not necessarily correspond to areas without displacement information, e.g., as seen in the gently inclined toe zone (<350 m a.s.l.) (Fig. 6.6). There, the presence of vegetation is high; however, considerable amounts of 2D InSAR points exist between clusters of shrubs/threes. The area was mapped as densely vegetated to emphasize that solifluction features most likely do not exist there, or the displacement related to solifluction is minimal. This is because vegetation tends to reduce the freeze-thaw frequency by acting as a thermal insulator and additionally has a binding effect near the surface (Matsuoka et al., 2001). Hence, most of the 2D InSAR points can be regarded to represent the RSD in this unit.

Fig. 6.10 shows all 2D InSAR points from Piggtind/Skulvatindane categorized after the source of the displacement: Superficial displacement (solifluction and deformation of debris deposits) rock glacier, and rock slope deformation.

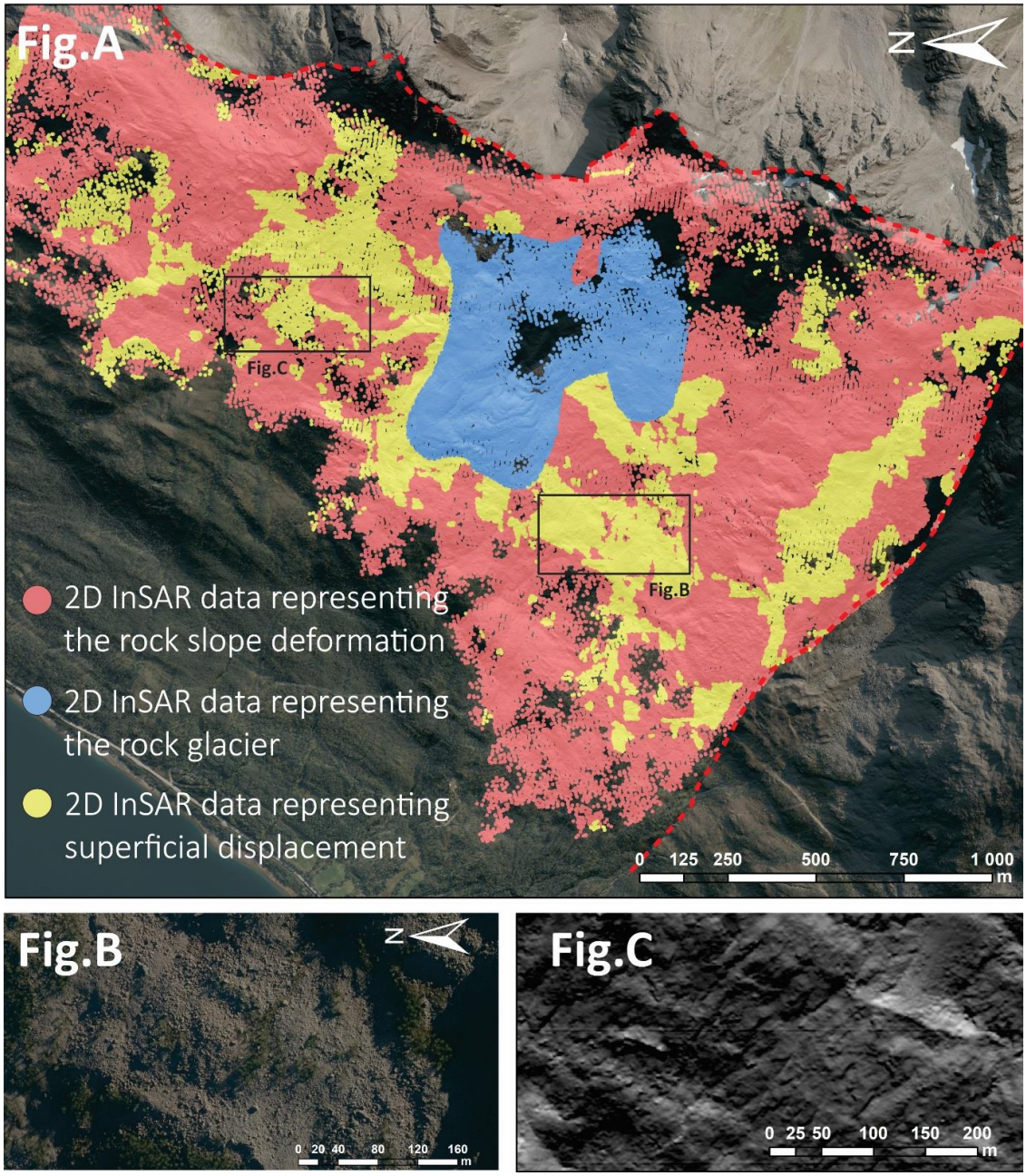

Figure 6.10: 2D InSAR results considered to represent the rock glacier (blue), RSD (red), and superficial movement (yellow). Fig. B orthophoto displaying an area dominated by loose unconsolidated/disintegrated rock. Fig. C Hillshade showing an area with solifluction lobes.

6.2.2 Kinematics of the RSD and spatial variations in displacement

2D InSAR results inferred to represent the kinematics of the RSD (red color in Fig. 6.10), are primarily considered in the further analysis of the RSD. However, they are not used exclusively. The following two sections aim to explain spatial variations in displacement and interpret the geometry of the basal rupture surface of the RSD.

Latitudinal variations in kinematics

The whole mountain flank stretching from the fault in the south to Lakselvnesåsen in the north shows both kinematic and geomorphological evidence of being deforming. However, the deformation does not seem to be completely uniform. The height of the backscarp is low in the southern part of the locality but progressively increases towards the summit of Piggtind. From there, it decreases again towards Lakselvnesåsen. This suggests that the area underneath- and just south of Piggtind is at a more evolved stage in the deformation process. 2D InSAR results reveal that this latter area also is most active at the present date. Especially one area above the rock glacier reveals increased combined 2D velocities (12–15 mm/yr).

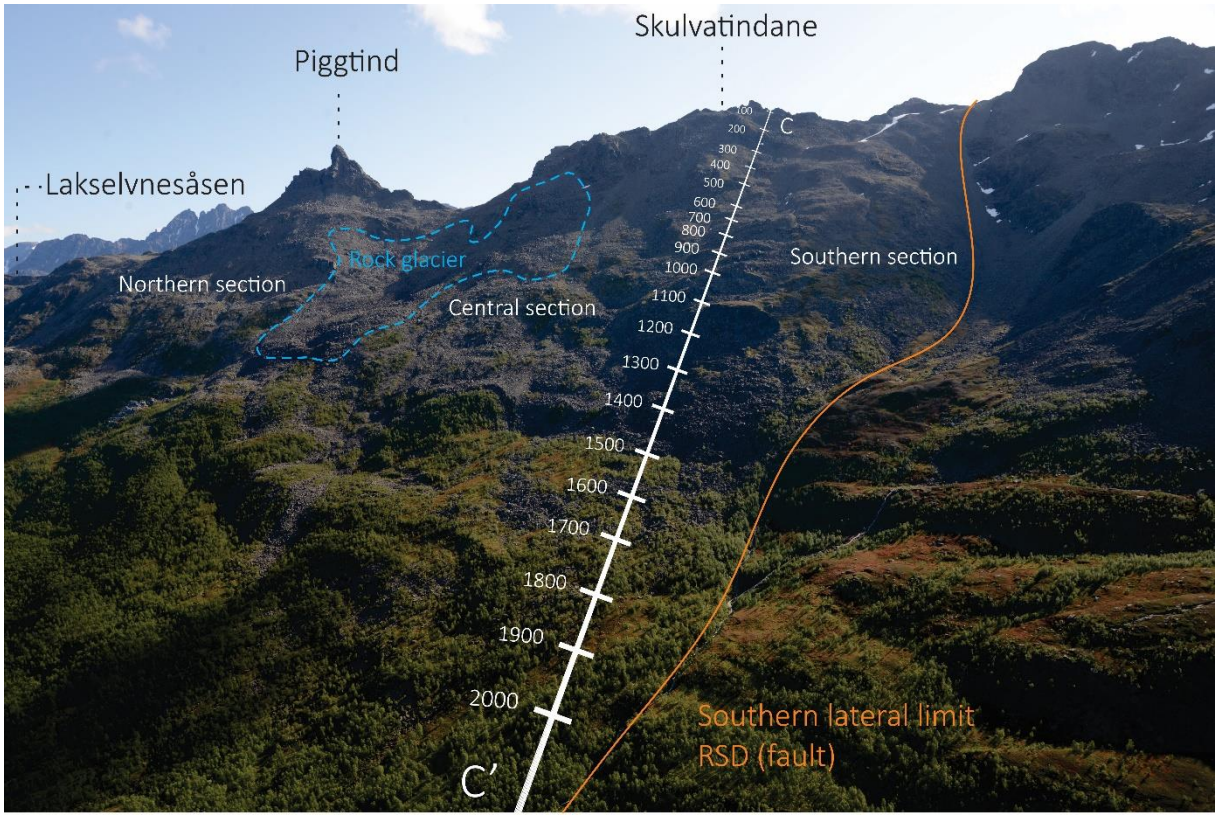

Figure 6.11: Overview of Piggtind/Skulvatindane. The inferred outline of the rock glacier is displayed with a blue dotted line, while profile C-C' is presented as with line. Photo direction: East. Photo: Martina Böhme (NGU).

The area at immediate vicinity to the fault creating the southern lateral margin protrudes from the surroundings with its convex-shaped topography (Fig. 6.11). The surface cover is mainly disintegrated rock and soil without dense vegetation (Fig. 6.2), which is similar to the area north. However, the higher presence of morpho-gravitational structures (Fig. 6.1) suggests that this is a thin cover obscuring disaggregated rock. This area is believed to be in an earlier phase of development. An abrupt change in velocity and dip of displacement is notable along a series

of ENE-WSW striking convex-concave slope changes (red lines on Fig. 6.8). These structures are inferred to be JN2 controlled normal faults that potentially delimit this area from the more actively deforming central section. However, the abrupt change in velocity is in certain areas influenced by superficial displacement (Fig. 6.10). Hence, the difference in velocity between the southern- and central section is not necessarily that substantial. This is also supported by 2D InSAR results from the terrace, which reveals only a slight increase in velocity.

The northern area is greatly affected by superficial slope processes. Much of the observed displacement is inferred to represent displacement in solifluction features and debris deposits (Figs. 6.10 and 6.7). However, small patches of disaggregated rock on the terrace are believed to be valid reflectors representing the displacement in the RSD. They reveal an average combined 2D velocity of approximately 9 mm/yr. This testifies that also this section is deforming at the present date but with relatively low rates.

Longitudinal variations in kinematics and geometry of the sliding surface

Fig. 6.12a-d shows 2D InSAR results with a tentative interpretation along profile C-C'. The geomorphological interpretations presented previously in this chapter have been compared with 2D InSAR results to analyze the RSD's kinematics. The location of the profile (highlighted in Figs. 6.11 and 6.6f) was determined based on the finding in Section 6.2.1, which suggested that superficial processes least influenced the southern area. The rock slope stability assessment using kinematic analysis did not provide any concluding evidence about the failure mechanism or discontinuity (or plural) creating the basal rupture surface. However, it revealed a weak potential for planar sliding. In addition, the extensive coverage of disintegrated rock prevents the application of structural indicators such as extensional fractures or matching paleic surfaces. Consequently, it is difficult to precisely determine the main direction of movement of the RSD. Therefore, it is presumed that the displacement is controlled by the foliation (dip direction 290°) (as witnessed on Njunnás).

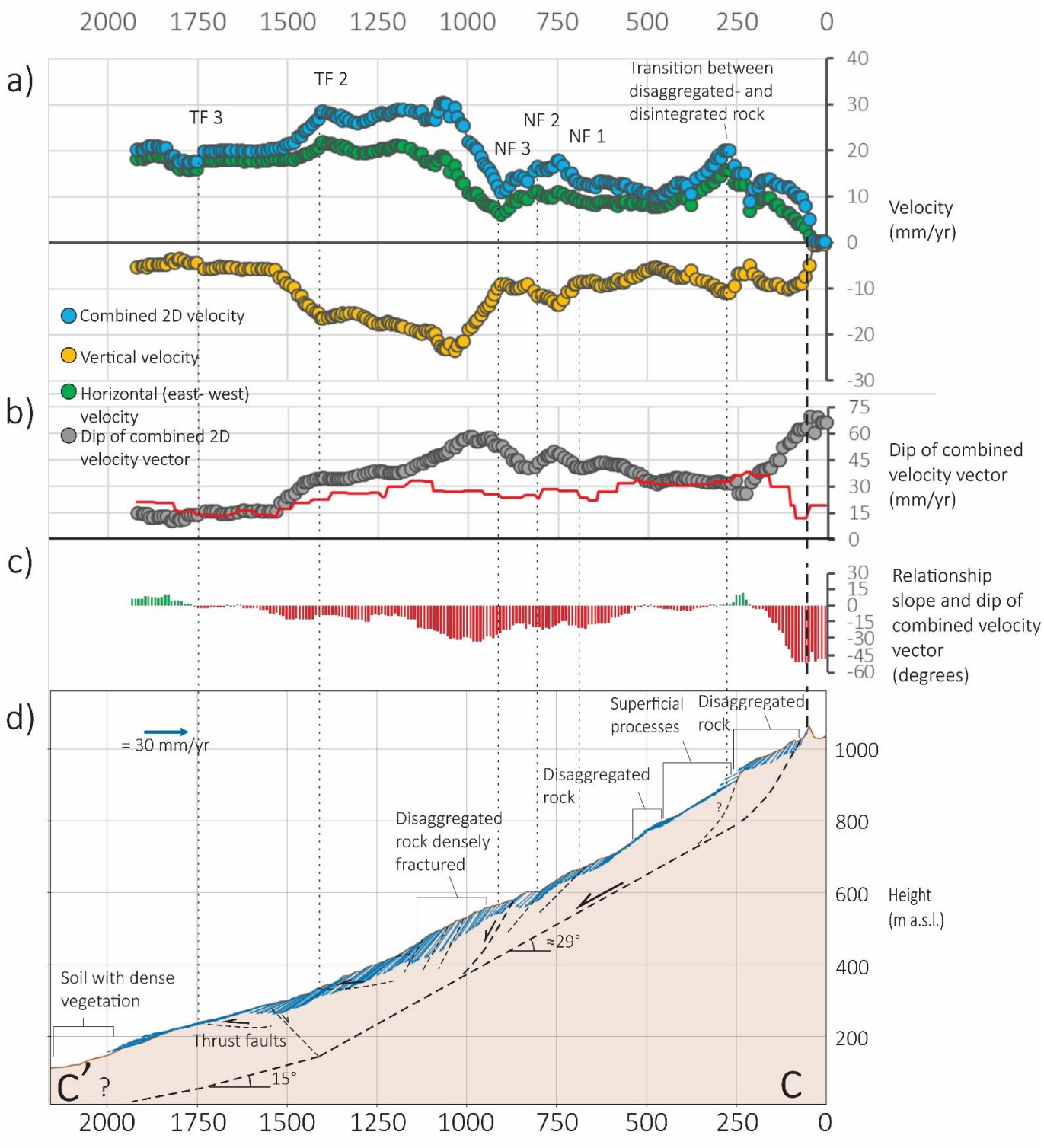

Figure 6.12: 2D InSAR results (a and b) and geological interpretation (d) along cross-section C-C'. The abbreviations NF and TF highlight the position of inferred normal faults and thrust faults, respectively. Inspired by Eriksen et al. (2017).

The basal rupture surface on Piggtind/Skulvatindane is inferred to be approximately planar in the slope's upper- and middle section. From 0–900 m along profile C-C', the vertical- and horizontal displacement rate distribution show some variability but is generally in the order of -7 to -10 mm/yr (Fig. 6.12a). The areas showing diverging velocities are considered to be affected by superficial deformation and/or displacement along structures dissecting the RSD. The latter clearly affects the observed kinematic behavior between 500–1150 m along profile C-C', as the dip progressively increases, reaching its maximum at 60° (Fig. 6.12b). This area corresponds to a section with abundant morpho-gravitational structures and abrupt convex-concave changes in slope morphology, creating a stepped slope profile (Fig. 6.11). These changes in morphology may represent an assemblage of dislocated/rafted terraces, segmented by faults, and may therefore serve as a reasonable explanation of the localized increases in dip of displacement.

The areas before (250–500 m) and after (1175–1475 m) this section with abundant morpho-gravitational elements show a somewhat constant dip in the order of 30–37° (Fig. 6.12b). This supports the hypothesis that the failure surface is approximately planar but also suggests that the foliation potentially is the discontinuity creating the basal rupture surface (average foliation in-situ 29° ± 11°). Alternatively, the slightly steeper dip could suggest that the basal rupture surface propagates by forming new structures, e.g., combining the foliation and steeper dipping joint planes. It should be emphasized that the displacement rates between 250–500 m are inferred to be predominantly affected by superficial processes (yellow in Fig. 6.10), as evidenced by the significant increase in horizontal velocity coinciding with the transfer zone between disintegrated and disaggregated rock. However, two minor disaggregated outcrops located 250–260 m and 475–500 m allows the kinematic pattern of the RSD to be identified and evaluated.

At approximately 1400–1550 m along profile C-C', a decrease in dip of displacement and vertical displacement is observed. This sudden spatial change in kinematics is thought to represent a transition into a lower inclined basal rupture surface (similar as witnessed on Njunnás). After the transition, the horizontal component greatly exceeds the vertical component, indicating that the displacement transpires along a low inclined structure. The observed pattern is similar to Frattini et al., (2018)’s simple sketch of displacement rate distribution for a slide with a bilinear failure surface (Fig. 6.13). The location of this transition zone can further be traced northward as an abrupt decrease in dip of displacement (350–375 m

a.s.l.) on Fig. 6.6b. North of the rock glacier, this transition zone corresponds to a 250 m long counterscarp (Fig. 6.1), which is thought to have developed as a response to the decreased dip angle of the basal rupture surface, i.e., formation of a normal fault (Fig. 6.13a).

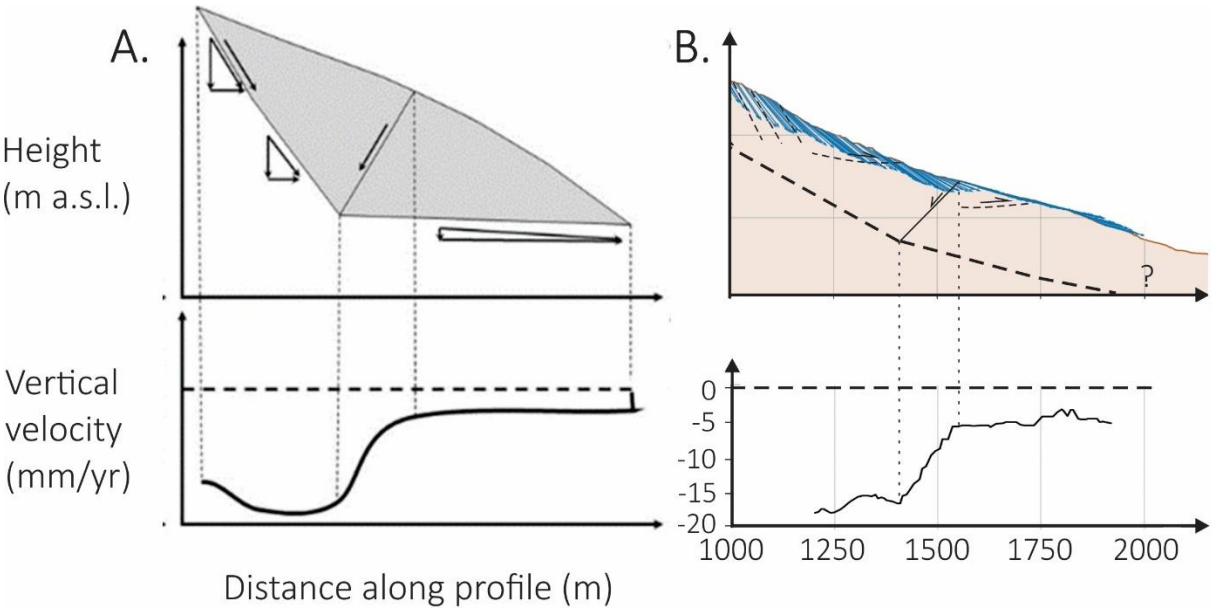

Figure 6.13: Simple sketch of displacement rate distribution in a slide with bilinear failure surface (A.) and the lower section of cross-section C-C' with interpreted failure surface and vertical displacement rate distribution along the profile (B.). Negative values indicate displacement into the slope (down). Figure A. is modified from Frattini et al. (2018).

An abrupt and significant increase in velocity is notable at ≈900 m along profile C-C' (Fig. 6.12a) and corresponds to a NE-SW striking pair of trenches. These structures potentially delimit a secondary instability. The trenches and the concave-convex slope changes in this area are inferred as the surface expressions of debris obscured normal faults. This interpretation is based on the observed increase in velocity and dip of displacement on the downslope facing sides of the structures.

6.2.3 Kinematics of the rock glacier complex

Fig. 6.14 a–d, shows 2D InSAR results with a tentative interpretation along profile D-D'. The mean aspect of the rock glacier and the surrounding area (290° ± 30°) is thought to represent the dominating displacement direction. This direction is approximately parallel to furrows and ridges in the rock glacier and thus supports the proposed movement direction (Haeberli et al., 2006).

The upper altitudinal limit of the rock glacier is inferred to be located at approximately 200 m along profile D-D' (700 m a.s.l.). This corresponds to a small break in the slope, which according to Humlum et al., (1998) is a characteristic feature representing the initial line of talus-derived rock glaciers. Furthermore, this transition is expressed as an abrupt increase in velocity and decrease in dip of displacement (Figs. 6.14 a and b). After this point, the angle between the dip of the displacement and slope inclination is mostly ± 10°, which may indicate that the surface topography dominantly controls the displacement. The lower altitudinal limit of the active rock glacier is inferred to be at approximately 400 m a.s.l. (875 m on profile D-D') and expressed by its steeply dipping front, a reduction in velocity, and abrupt presence of vegetation. As highlighted by Wang et al., (2017), Sattler et al., (2016), and Humlum et al., (1998), this line may represent the lower altitudinal limit of discontinuous/sporadic permafrost and thus provide information about the state of the permafrost in this area. The area immediately below this limit displays similar surface characteristics observed on the active rock glacier, i.e., furrows and ridges. However, the lower displacement rates combined with higher presence of vegetation imply that this is an inactive lobe (C. on Fig. 6.15).

Profile D-D' reveals that the displacement rates generally are higher in the center- and frontal section of the rock glacier and gradually decreases towards the outer limits. A similar conclusion can also be drawn from morphological features such as ridges and furrows. In the center of the glacier, these structures are oriented approximately perpendicular to the postulated movement direction. Towards the margins, they gradually rotate and ultimately culminates as longitudinal features. This rotation is likely due to a progressive decrease in velocity towards the lateral margins (Kääb and Weber, 2004).

Within the delimitations of the rock glacier, an overall trend with increasing combined 2D velocities can be observed from the initiation line to approximately 750 m along profile D-D'. From there, the rates progressively decrease again. The area displaying decreasing velocities is consequently subjected to compressive stress, and the surface morphology is characterized by convex features inferred to be bulges. The compressive flow forces material to heave, resulting in the development of bulges (Kääb and Weber, 2004). This distinct pattern with displacement out of slope on/immediately in front of topographic highs (bulges and lobes) is frequently accompanied by displacement into slope immediately behind (Fig. 6.14c).

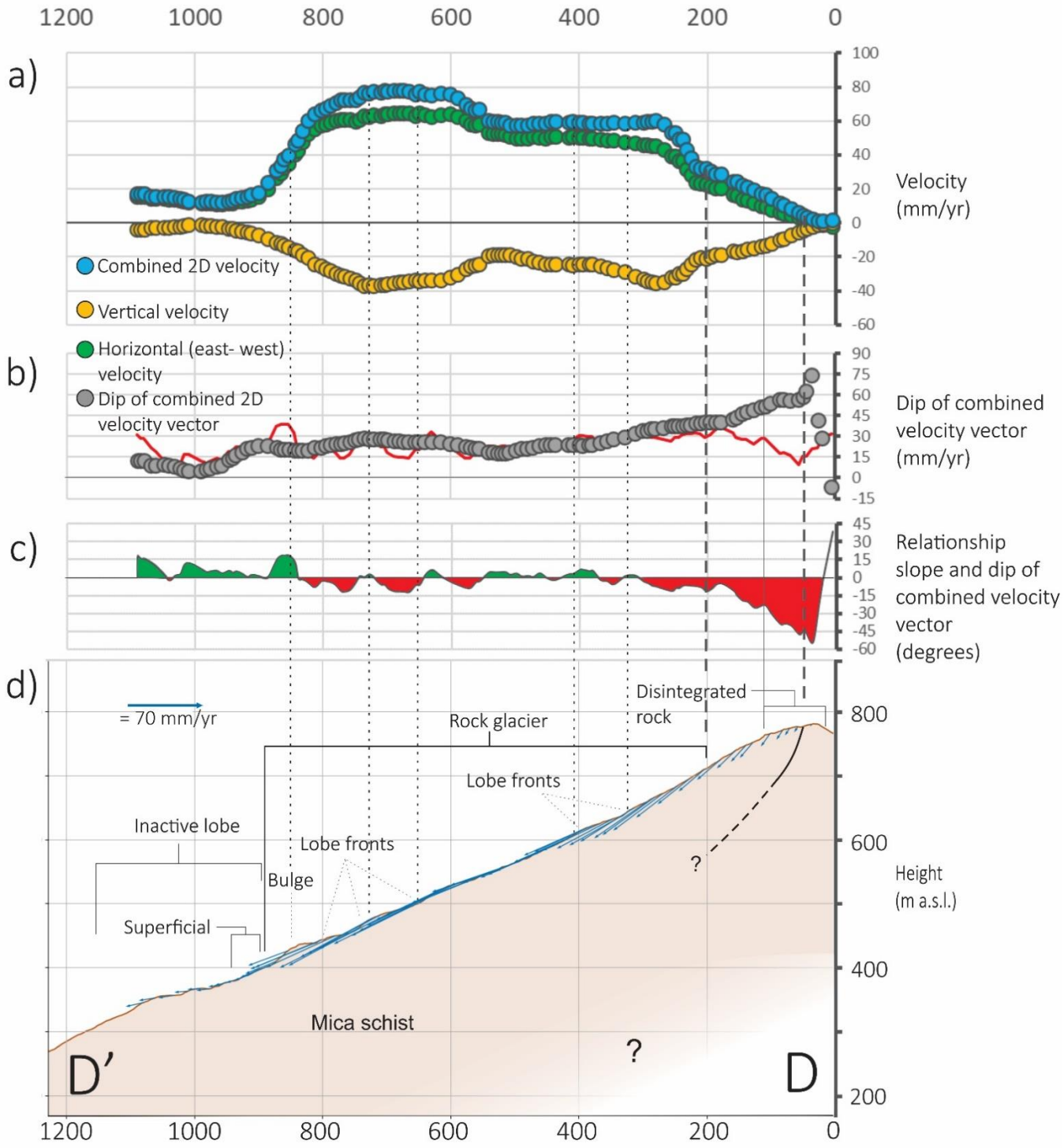

Figure 6.14: 2D InSAR results and geological interpretation along cross-section D-D'. The 2D InSAR results are produced by combining three ascending geometries and three descending geometries. A search radius of 10 m is applied for better precision on the rock glacier. Consequently, this also results in fewer 2D InSAR points in areas with scattered ascending and descending data. A slope raster with a resolution of 10 m is applied for constructing the "into- out of slope" graph (c). Inspired by Eriksen et al. (2017).

We can from Fig. 6.15 see that two areas within the postulated limits of the rock glacier show increased velocities (marked A and B on Fig. 6.15). If these two areas represent two distinct units or not is difficult to evaluate since the center of the landform lacks displacement information, possibly due to phase ambiguity (too high velocities). However, considering that the rock glacier contains multiple lobes with different kinematic statuses (inactive and active) embedded into each other, the rock glacier can be classified as a multi-lobed complex (Jones et al., 2019).

The proposed rock glacier immediately underneath the summit of Piggtind has been dedicated little attention (D. on Fig. 6.15). Field observations suggest that the area consists of loose rock with fraction size generally smaller than elsewhere on the locality. The obvious cluster showing increased velocity may potentially be attributed to the deformation of a rock glacier. However, the lack of obvious geomorphological features characteristic for rock glaciers hinders the interpretability and can therefore not confirm this conjecture. Alternatively, the increased velocity may correspond to superficial deformation of the loose debris deposits. This is not unlikely, considering the steepness of the slope in combination with the highly disintegrated texture.

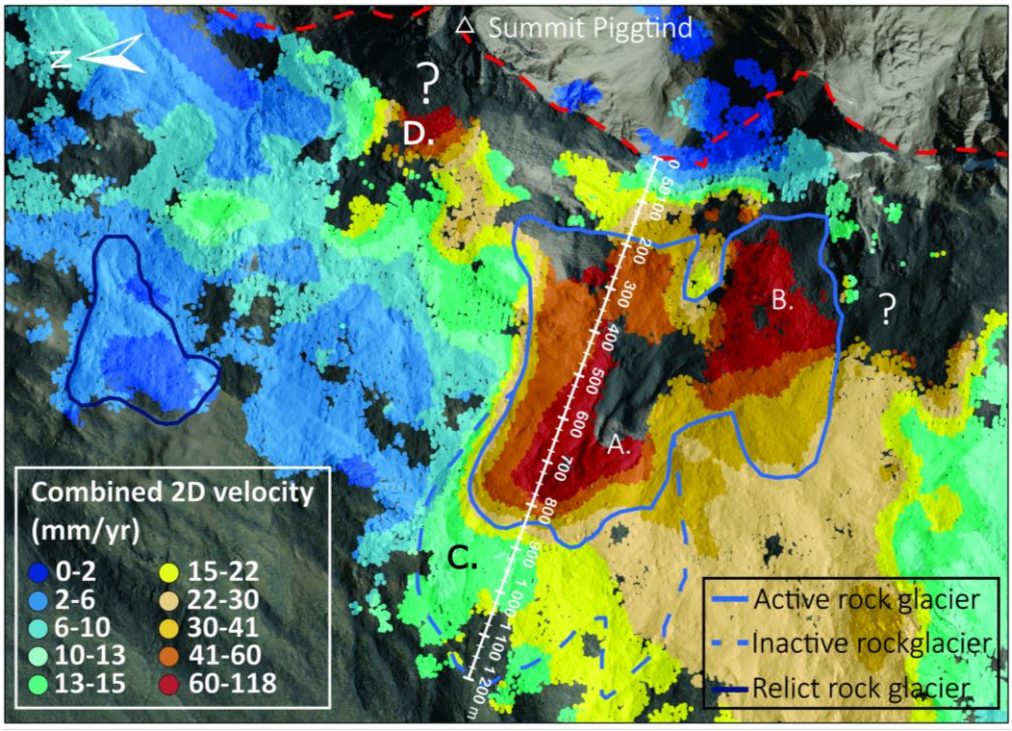

Figure 6.15: Combined 2D velocities from the area containing the rock glaciers. The standard classification method "natural breaks" is used to define the range of the classes, i.e., classes are based on natural grouping inherent in the data set. This is done to highlight spatial changes in velocity. Certain areas are missing displacement information, which can be related to multiple reasons (vegetation, phase ambiguity, shadow, and layover), or the fact that the rock glacier displays a nonlinear displacement behavior.

7 Synthesis and discussion

The following chapter aims to synthesize the results of the two localities and evaluate limitations and challenges regarding the interpretation and utilized methods. In addition, the relevance and transferability of the findings and proposed methods are discussed.

7.1 2D InSAR method

In this thesis, the newly developed 2D InSAR tool has been exploited for evaluating kinematic patterns of various slope processes in Piggtind, Troms. By decomposing the combined 2D displacement into a horizontal- and vertical component, better visualization of the kinematic patterns could be achieved.

The 2D InSAR results utilized in this thesis have not been validated against other measuring techniques. However, a detailed comparison of 2D InSAR results and GNSS (Global Navigation Satellite System) station network data was completed in a study on Jettan (37 km NE) and revealed a satisfying correlation (Eriksen et al., 2017).

7.1.1 Comparison InSAR and 2D InSAR

As highlighted in Section 4.1.2, exploiting single geometry LOS InSAR for evaluating surface displacement in mountainous regions can be problematic and require knowledge regarding the surface displacement direction with respect to the satellite LOS. The 2D InSAR method applied in this study successfully mitigates this LOS ambiguity in the E-W plane. This can be demonstrated by comparing displacement rates obtained from individual InSAR datasets and the 2D InSAR results created in this thesis. From Table 7.1 one can observe that the individual InSAR datasets obtain very different velocities for Piggtind/Skulvatindane and Njunnás. The variability is related to different LOS orientations (azimuth- and incidence angle) compared to the direction of the surface displacement. The measured velocity with 2D InSAR is higher than what proposed by single geometry LOS InSAR at both locations, suggesting that the 2D InSAR method is able to capture more of the three-dimensional surface displacement. However, the difference is small, indicating that the LOS orientation is generally favorable, especially for the descending geometry. The fact that much of the displacement is inferred to be predominantly westward, and very little of the slope aspect is north- or south-facing (Fig. 7.1), is one of the major advantages of the localities. One can expect that a large portion of the three-dimensional surface displacement is detected. Hence, the presented rates in this thesis are likely representative.

Table 7.1: Properties of the different InSAR Norway datasets (ascending and descending geometries) and the constructed 2D InSAR results. Values are extracted from within the postulated deforming areas of Njunnás and Piggtind/Skulvatindane.

Dataset	**Njunnás**			
	Count	**Average velocity (mm/yr)**	**Average nearest neighbor (m)**	**LOS orientation (Azimuth-/incidence angle)**
Ascending 1	1144	-0.3	5.3	76/35°
Ascending 2	1456	-0.3	4.7	77/40°
Ascending 3	2280	0.1	3.3	80/44°
Descending 1	1345	-2.8	4.2	285/33°
Descending 2	1523	-2.3	3.5	283/38°
Descending 3	1331	-3.1	3.8	281/42°
2D InSAR	**8549**	**2.9**	**1.88**	
	Piggtind/Skulvatindane			
Ascending 1	17627	-0.2	5.9	76/35°
Ascending 2	21773	2.1	5.1	77/40°
Ascending 3	28834	2.5	4.1	80/44°
Descending 1	35052	-17.3	2.9	285/33°
Descending 2	46835	-14.8	2.3	283/38°
Descending 3	34574	-17.6	2.9	281/42°
2D InSAR	**176977**	**18.8**	**1.7**	

The 2D InSAR results, which are created by combining 6 InSAR Norway datasets, also reveal better spatial coverage and higher density of persistent scatterer points than each individual InSAR dataset. This is favorable when evaluating the spatial extent and kinematic patterns of the landforms. Indeed, the number of computed CSD points are approximately four times higher than the InSAR Norway dataset with the most persistent scatterers (Table 7.1), and the average distance between two individual scatters is reduced (25% and 40% reduction in the average distance between neighbor scatters for Piggtind/Skulvatindane and Njunnás, respectively). Furthermore, by utilizing multiple InSAR Norway datasets for creating the CSD points, one can more successfully identify potential outliers.

7.1.2 Encountered constraints with InSAR

As discussed in Section 7.1.1, the 2D InSAR method mitigates some of the limitations and ambiguities experienced with single geometry InSAR. However, constraints due to temporal decorrelation and geometrical effects will affect the spatial resolution of the 2D InSAR results. This is evident when viewing Figs. 5.7 and 6.6, where displacement information is missing, especially from the toe and along the backscarp of the RSD at Piggtind/Skulvatindane. Fig. 7.1 highlights areas on Piggtind where InSAR theoretically fails and provides plausible explanations of most of the missing data.

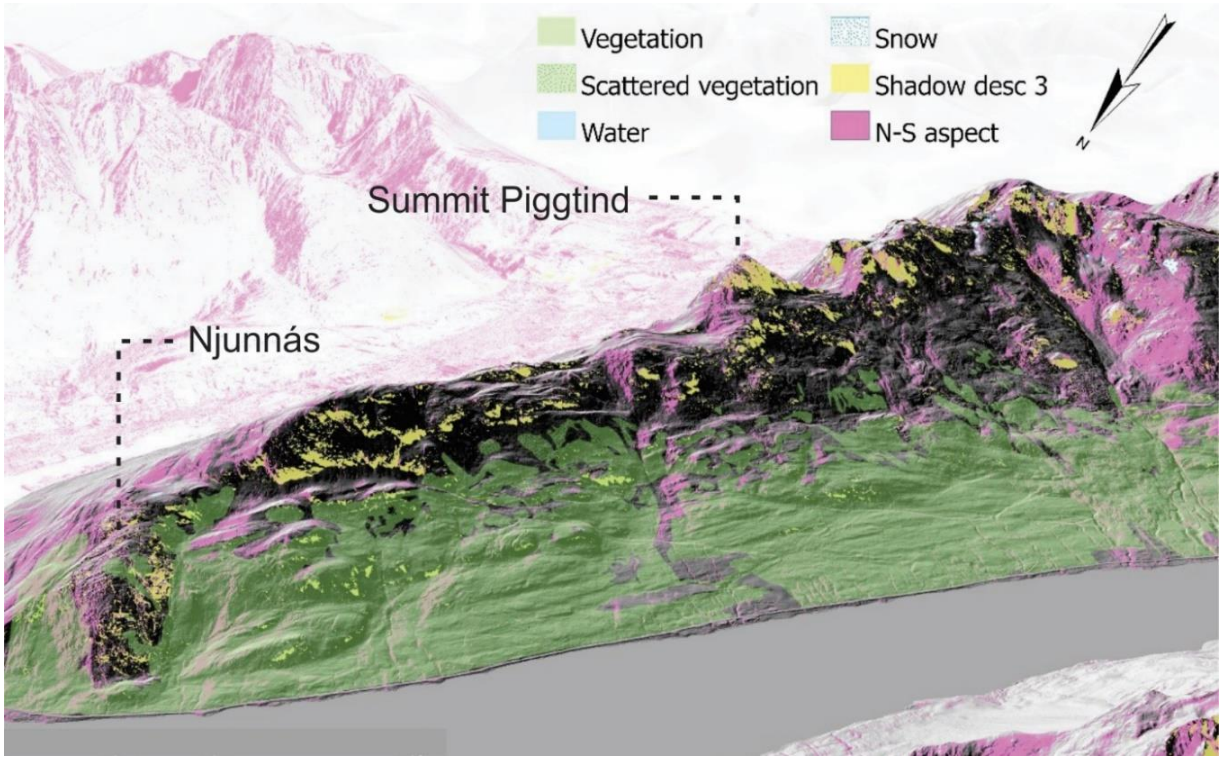

Figure 7. 1: The figure highlights areas where displacement information may be problematic to obtain with InSAR due to temporal decorrelation and geometric effects. A shadow mask is calculated for descending 3 (yellow color) and highlights areas where displacement-information theoretically is impossible to acquire with that dataset. Pink mask (N-S mask) represents areas on the slope with aspect between 335.5–22.5° and 202.5–157.5° (thresholds according to Rouyet et al., 2019). These areas are not affected by decorrelation. However, superficial displacement in these sections is expected to have a larger N-S component. Considering the low sensibility of the SAR instrument in the N-S plane, these areas may have underestimated rates.

7.2 Slope process classification

Both Njunnás and Piggtind/Skulvatindane involve a comprehensive rock slope deformation affecting the entire slopes. The RSD at Njunnás is mainly composed of disaggregated quartzite with little soil and disintegrated rock. This is a beneficial environment, allowing displacement information attributed to the RSD to be easily detected with InSAR. Piggtind/Skulvatindane shows a more complex morphology involving multiple slope processes, all leading to surface displacement. Hence, to evaluate the kinematics of the RSD and the rock glacier on Piggtind/Skulvatindane, it was critical first to identify and delimit the distinct landforms.

As highlighted in Section 6.2.1, a large rock glacier complex superimposed on the RSD at Piggtind/Skulvatindane, has been more precisely delineated (refined to 0.38 km^2 from the original size of 0.5 km^2 proposed by Rouyet et al., (under review)). I applied a multi-disciplinary approach investigating both the morphostructural characteristics typical for rock glaciers and the 2D displacement rates. The combination of these two approaches is valuable since they can be used to supplement each other. Furthermore, an obvious correlation between lobate-shaped ridges and increased velocity is in certain areas observed, resulting in a robust interpretation. Exclusively utilizing disparities in velocity for evaluating the limits would be indeed difficult. The two processes show some overlap in rates, and the method will, therefore, at best, only identify the most prominent and active part of the rock glacier.

The high presence of soil and disintegrated rock on Piggtind/Skulvatindane made it problematic to identify persistent scatters representative of the kinematics of the RSD. Only 10% of the surface cover was disaggregated rock. Hence, it was imperative to try identifying other CSD points representative of the RSD kinematics although location in other units. I proposed to go into that direction by investigating the relationship between the slope inclination and the dip of the combined 2D velocity vector.

In total, 43% of the CSD points from “soil without dense vegetation” and 31% of the “disintegrated” unit were considered to primarily represent superficial displacement (solifluction and superficial deformation of debris deposits) based on the similarity between dip of displacement and surface inclination. This is a significant proportion, however not unexpected considering the spatial coverage of these units (19% of the deforming area is classified as soil without dense vegetation and 39% as disintegrated rock).

In order to verify the classification, a visual inspection has been carried out. We can from comparing Figs. 6.10 and 6.2 observe that CSD points classified as superficial often coincide with mapped solifluction lobes and areas with highly disintegrated rock. In addition, as displayed in Fig. 7.2, points with considerably greater velocity than the disaggregated unit are masked out (Fig. 6.9d). However, verifying the classification on visual inspections may be imprecise. An alternative approach investigating the relationship between slope inclination and combined 2D velocity is therefore evaluated as beneficial. Since superficial slope processes are thought to be controlled by the terrain, there should be a correlation between the steepness of the slope and velocity, i.e., steeper slope inclination will produce faster displacement rates. However, a simple correlation test ("=CORREL" in excel) reveals no correlation for the CSD points classified as superficial (actually, negative correlation -0.14). The inconclusive relationship between the velocity of the superficial displacement and slope inclination is suspicious and potentially undermines the classification. It is, therefore, reasonable to assume that more of the CSD points represent RSD than suggested by the classification.

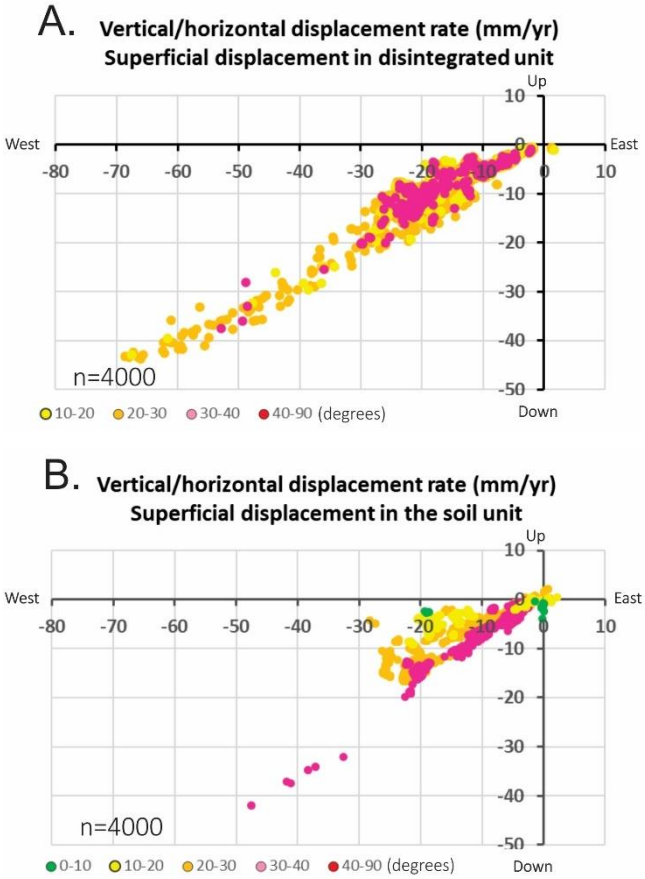

Figure 7.2: Scatter plots of 2D InSAR results assumed to represent superficial displacement in the disaggregated unit (A.) and soil without dense vegetation unit (B.). The scatter plots of the two units consists of 4000 randomly chosen pixels. A random selection has been carried out because of the large size of the data set.

A plausible explanation for why the classification method based on the relationship between dip of displacement and slope inclination partially fails is that similarities may also represent displacement along a deeper structure that is oriented parallel to the slope surface. This scenario is not unlikely as the shape of the mountains often reflects the structures in the rock. When viewing profile C-C' (Fig. 6.12) from Piggtind/Skulvatindane, it is evident that the inclination

of the basal rupture surface in places coincides with the slope inclination of the surface (parallel orientation). If the dip of the 2D velocity vectors is approximately equal to the slope inclination in these areas, it may suggest superficial displacement or displacement developing along a deeper structure (RSD). This ambiguity could potentially be resolved by examining displacement rates. One could hypothetically assume that if these areas truly represent displacement along the deeper structures, the displacement rates will be in the approximately same order as observed in the head domain or in disaggregated rock in close vicinity. However, this conjecture is only valid if the displacement in the RSD is uniform. The limited spatial coverage of the disaggregated rock hinders such evaluation, and further assessments are therefore impossible at this stage.

Based on the highlighted limitations, the method does not successfully allow for differentiation deep and superficial displacements. There are too many uncertainties, and it is challenging to validate the result precisely. However, with that said, the method does disclose what areas have surface displacement likely reflecting the deeper structure (large deviation between slope inclination and dip of combined 2D velocity vector). However, one must then acknowledge that the displacement rate potentially includes a small additional superficial component that is not significant enough to affect the dip of the combined 2D velocity vector. Hence, to obtain precise evaluations of the RSD kinematics, the CSD points should predominantly origin from the disaggregated unit.

7.3 Kinematics of the rock slope deformations

The deformation rates of the RSDs at Njunnás and Piggtind/Skulvatindane have been evaluated in this thesis. The detected displacement rates with 2D InSAR have been low in general. On Njunnás, the velocity was in the order of a couple of mm/yr, and thus highlight the high sensitivity of InSAR (and the PSI processing methods) to detect small ground displacements. One could argue that the RSD on Njunnás could be classified as inactive or subfossil RSD because of the low displacement rates. However, such a classification requires accurate displacement measurements from the entire deforming area. Dense vegetation has prohibited full coverage, and thus, assigning “inactive” to the RSD would be indeed bold.

7.3.1 The geometry of the basal rupture surface

The geometry of the basal rupture surface and subsequently the kinematic behavior was compiled using the rock slope stability assessment using kinematic analysis (Dips8 software)

and surface displacement information. Two methods utilizing 2D displacement information were used for determining the basal rupture surface: Investigating spatial variations in horizontal and vertical velocity (as demonstrated by Frattini et al., (2018)), and investigating the dip of the combined 2D velocity vector (as demonstrated by Intrieri et al., (2020), Böhme et al., (2016), and Eriksen et al., (2017)). By exploiting multiple approaches, result validation was possible to implement, ensuring a more robust interpretation.

The rock slope stability assessment using kinematic analysis was only partially successful for both localities. As discussed in Section 4.2.1, the method tests only three simple failure modes, which means that more complex modes of slope deformation are not considered. Furthermore, the kinematic analysis is a simplistic method initially developed for small outcrops such as highway road cuts (Stead and Wolter, 2015). It depends on multiple assumptions, such as uniform slope properties (aspect and slope inclination) and friction angle, and even spatial distribution of orientation measurements (Park et al., 2016). The degree of uncertainty regarding these assumptions increases when this method is applied on a large natural mountain slope. This limitation becomes evident when investigating Njunnás. There, the analysis showed that both planar and wedge sliding were kinematically possible, with a relatively high percentage of discontinuity poles within the critical zones of the two failure modes. However, fitting a planar basal rupture surface between the active major scarp and the expected toe zone was impossible (Fig. 7.3). In contrast, the VIM method suggests that the basal rupture surface was bi-planar or becomes listric with depth, implying that it is a composite landslide. This postulated failure mechanism could not be verified with the kinematic analysis. Which structure utilized as this low-angled failure surface is not determined. However, foliation underneath Lakselvnesåsen was observed to progressively decrease in inclination (Appendix 6). One can therefore speculate that a similar spatial change in inclination occurs underneath Njunnás.

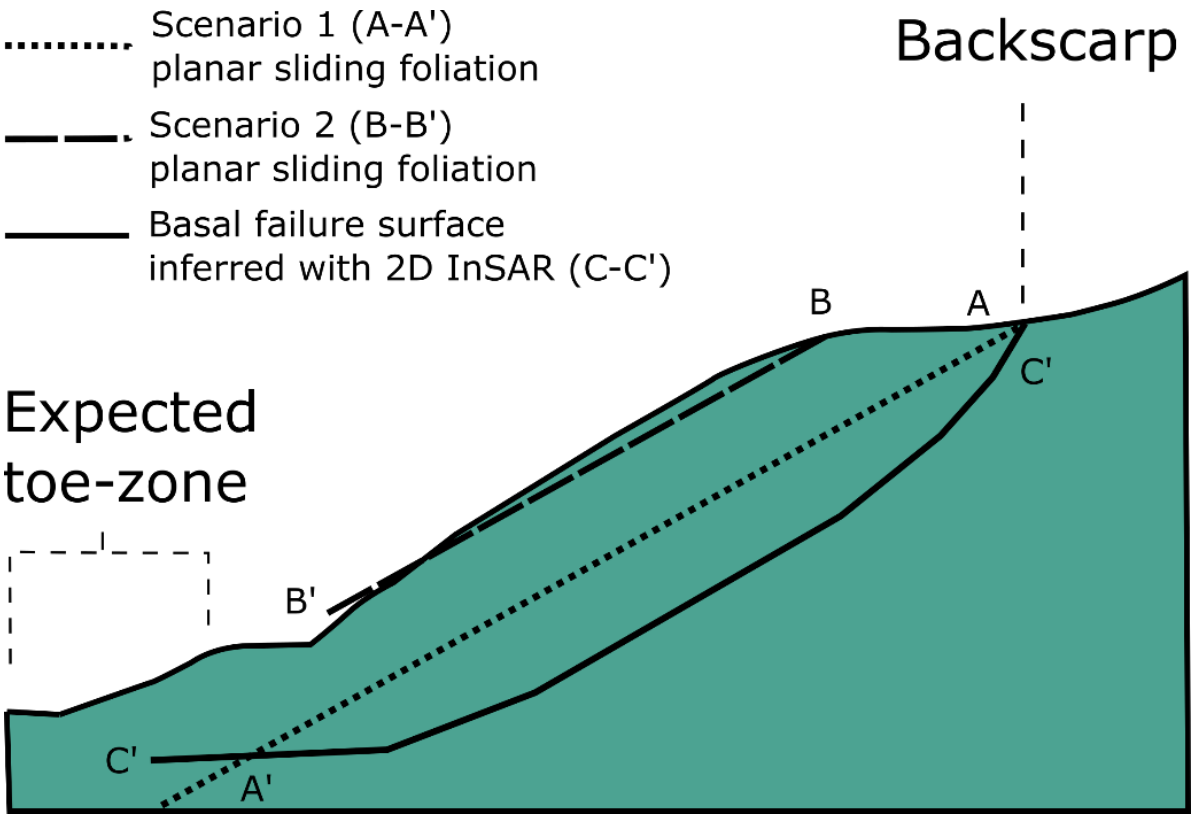

Figure 7.3: The inferred basal rupture surface on Njunnás based on VIM (black solid line C-C') is sub-horizontal in the lower section of the slope (bi-planar). Plane A-A' and B-B' represent planar sliding on the foliation (31°). Planar sliding is theoretically possible, as highlighted by B-B,' but this confines the RSD to be shallow and not intersect with the inferred backscarp. When fitting the planar plane from the backscarp, it prevents daylighting in the expected toe-zone.

On Piggtind/Skulvatindane, the rock slope assessment using kinematic analysis showed that the three tested failure mechanisms were kinematically feasible, however unlikely. In the analysis, the gap between the slope angle and friction angle (i.e., daylight envelope) was very small (only 4°). All input parameters were selected conservative, e.g., friction angle 20° after recommendations from Hermanns et al., (2012). Indeed, a more realistic value for the friction angle would be >20° and possibly as high as 27–29° (Wyllie & Mah, 2004; Barton, 1973). This could potentially yield no intersection at all, meaning that the analysis would conclude that planar- and wedge sliding is impossible. Investigations of spatial variations in velocity and the VIM, suggested a feasible explanation for this inconclusive result. The basal rupture surface is, as observed on Njunnás, likely bi-planar or curved with depth. The fact that both RSDs are likely compound slides is not unexpected considering that most RSDs in the region are (Vick et al., 2020). Furthermore, as highlighted by Zangerl et al., (2019), such style of deformation is quite common in antistrophic rock such as mica schist.

Although the kinematic analysis produced weak and inconclusive results regarding the failure mechanisms, it contributed to increasing the understanding of the structure used as the basal rupture surface. Subsequently, it also helped to identify the main displacement direction of the RSD on Njunnás. The inconclusive results also highlight the importance of including complimentary methods to evaluate the failure mechanism. As shown in this thesis, investigations of the spatial variations of 2D displacement along longitudinal swaths provide relevant hypotheses regarding the geometry and depth of the basal rupture surface.

The depth of the basal rupture surface, which was evaluated by the vector inclination method (VIM), proved to be a robust and valuable tool. However, since the method is graphical, it is difficult to precisely determine the margin of error. It is expected that the lack of a clear demarcated toe (on Njunnás) and the high presence of vegetation in the lower section of both RSDs, have adversely affected the precision of the rupture surface estimation.

The approach investigating the geometry of the basal rupture surface by evaluating variations in horizontal- and vertical velocity along longitudinal swaths produced matching results as the VIM, and hence supported the interpretation. The simplified finite element model of Frattini et al., (2018) proved valuable to classify the failure mechanism more accurately. Possible errors in relation to this method are mainly related to the accuracy of the InSAR data and the influence of structures or heterogeneous material properties affecting the evolution of the RSD (Section 2.2.1).

7.4 Kinematic of the rock glacier complex

The rock glacier complex located between the summits of Piggtind and Skulvatindane is interpreted to be superimposed on the RSD. This agrees with Rouyet et al., (under review)'s suggested classification (landslide-connected). Furthermore, based on spatial variations in morphology and velocity, the rock glacier comprises multiple disparate lobes with different kinematic status.

Contrary to the RSDs, the rock glacier revealed high velocities, up to 157 mm/yr. The highest rates are detected in the immediate vicinity to areas lacking displacement information. The lack of information cannot be explained by any of the highlighted limitations in Fig. 7.1, and thus, likely are related to phase decorrelation or non-linear displacement behavior. The former is plausible, as 157 mm/yr is close to the theoretical maximum detection capacity of the Sentinel-

1 satellite (170 mm/yr) (Table 4.1). Nonetheless, this may indicate that the surface velocity of the rock glacier is higher than what was proposed in this thesis, and highlights InSAR's (and the PSI processing methods) limitations to evaluate fast-moving landforms. For the purpose of evaluating fast-moving landforms, another multi-interferogram technique, such as Short-baseline interferometry (SBAS), may be more favorable.

The lower altitudinal limit of the active part of the rock glacier complex is postulated at 400 m a.s.l. As suggested, this limit potentially concurs with the lower altitudinal limit of sporadic/discontinues permafrost on Piggtind. This interpretation is, however, in disagreement with Farbrot et al., (2013)'s postulated LALP at 800–900 m a.s.l. Nevertheless, as highlighted by Magnin et al., (2019), considerable variations are observed in Troms, closely related to disparities in, e.g., sun exposure. LALP has been detected as low as 50 m a.s.l. in west-facing slopes between 69°N and 70°N (Magnin et al., 2019), thus supporting the possibility of a local LALP at 400 m a.s.l.

7.5 Suggestions to future work and the transferability of the study

Further work on Piggtind should focus on the RSD located between Njunnás and Piggtind/Skulvatindane, which shows obvious morphostructures typical for RSDs (Appendix 7). The locality was originally in the scope of this thesis. However, little displacement information was possible to obtain from the middle- and lower sections of the slope. Therefore, the focus was shifted from this area to the neighboring areas. In addition, a hazard analysis could be conducted on Njunnás and Piggtind/Skulvatindane, considering the proximity to settlements and infrastructure. The findings in this thesis would be a valuable resource for such evaluations. Preventive risk management for residents along the fjord should be preceded by a hazard analysis of the large slope according to methods developed by NGU (Hermanns et al., 2012).

As the 2D InSAR methodology and proposed approaches show great promise, they could be incorporated in larger studies, potentially encompassing regions. Furthermore, the NGU-initiated national campaign, which aims to systematically map and characterize RSDs, would benefit from exploiting the 2D InSAR. The inventory could potentially be updated with failure mechanism proposed from 2D kinematics. This would assist estimations of volume and subsequently improve run-out calculations, which are imperative in hazard management.

Indeed, such an approach has been conducted in two regional studies in Italy (Crippa et al., (2021) and Frattini et al., (2018)) and shows promising results.

2D InSAR could also be exploited in other case studies of localities showing the same complexity as Piggtind/Skulvatindane. Njávávarri, which recently experienced increased activity (higher frequency of rockfalls), would be a favorable choice. As this study encountered difficulties regarding the identification and delimitation of superficial slope processes, one could additionally implement 2D InSAR time series. As demonstrated by Dini et al., (2019a), evaluating temporal variations in displacement, may serve as a prominent tool for identifying slope processes in mountainous regions.

8 Conclusion

2D InSAR has been exploited to produce comprehensible presentations of the surface displacement patterns at Njunnás and Piggtind/Skulvatindane. In combination with a structural and geomorphological analysis, two-dimensional displacement information has provided valuable information for characterizing the RSDs. Furthermore, the multidisciplinary approach proved advantageous for identifying, delineating, and describing the kinematic patterns of the rock glacier complex.

The exploited approach has resulted in the following conclusions:

- Longitudinal variations in velocity and dip of combined 2D velocity vectors, combined with substantial disintegration of rock in the lower section, suggest a bi-planar or curved basal rupture surface on Njunnás. Sliding potentially follows pre-existing foliation planes, dipping 30° towards 290°. The RSD is characterized by low (a few mm/yr) uniform displacement rates and thus believed to deform as a coherent mass. The rear delineation, which potentially utilizes a fault plane, is well expressed on the produced 2D deformation map as a sudden change in velocity and corresponds to mapped trenches.

- The RSD at Piggtind/Skulvatindane is classified as a compound bi-planar/curved slide. Latitudinal variations in velocity and morphological complexity imply some variations in maturity. The central section is likely at a more evolved stage in the deformation process than the northern- and southern sections. The RSD comprises nested sectors with increased displacement, suggesting some internal segmentation. However, most of the clusters with increased displacement can be attributed to deformation of superficial slope processes.

- The contrasting surface properties between the two RSD, and the extensive influence of superficial and periglacial slope processes on Piggtind/Skulvatindane, have highlighted the capabilities and constraints with 2D InSAR for assessing RSD kinematics. The need for complementing 2D InSAR with geomorphological mapping is highlighted on Piggtind/Skulvatindane, where multiple slope processes overlap. The surficial/superficial mapping was essential for identifying reflectors representing the

displacement of the RSD. However, the high presence of superficial slope processes has likely adversely affected the reliability of the interpretation.

- The identification and delineation of the rock glacier complex were assessed by investigating morphological characteristics and spatial variations in velocity. An obvious correlation between lobate-shaped ridges and increased velocity is observed in certain sectors. The original size of the inventoried rock glacier is refined and highlights the importance of combining morphostructural characteristics with 2D InSAR for higher accuracy.

  The rock glacier complex is classified as a landslide-connected, multi-lobate complex comprising active and inactive lobes. The lower altitudinal limit of the active rock glacier is postulated at 400 m a.s.l. and thus, provides valuable information regarding the local altitudinal limit of permafrost. The PSI-based 2D InSAR method proved helpful for detailed assessments of the rock glacier kinematics. However, it was not possible to detect the highest velocities due to phase decorrelation and/or non-linear displacement behavior.

- Identifying solifluction features and superficial deformation of mass-wasting deposits by examining kinematic characteristics proved indeed difficult. The most reliable approach for accurately identify and delineate superficial slope processes is to map superficial deposits and landforms based on in-field observations and orthophotos.

References

Agliardi, F., Crosta, G. B., & Frattini, P. (2012). Slow rock-slope deformation. *Landslides: Types, Mechanisms and Modeling*, 207–221.

Agliardi, F., Crosta, G., & Zanchi, A. (2001). Structural constraints on deep-seated slope deformation kinematics. *Engineering Geology*, *59*(1–2), 83–102. https://doi.org/10.1016/S0013-7952(00)00066-1

Andresen, A., & Bergh, S. (1985). Stratigraphy and tectonometamorphic evolution of the Ordovician-Silurian Balsfjord Group, Lyngen Nappe, north Norwegian Caledonides. *GEE, D. G. & STURT, BA (eds) The Caledonide*, 579-592.

Barboux, C., Delaloye, R., & Lambiel, C. (2014). Inventorying slope movements in an Alpine environment using DInSAR. *Earth Surface Processes and Landforms*, *39*(15), 2087–2099. https://doi.org/10.1002/esp.3603

Barboux, C., Strozzi, T., Delaloye, R., Wegmüller, U., & Collet, C. (2015). Mapping slope movements in Alpine environments using TerraSAR-X interferometric methods. *ISPRS Journal of Photogrammetry and Remote Sensing*, *109*, 178–192. https://doi.org/10.1016/j.isprsjprs.2015.09.010

Barton, N. (1973). Review of a new shear strength criterion for rock joints. *Engineering Geology*, *7*(4), 287–332. https://doi.org/10.1016/0013-7952(73)90013-6

Benedict, J. B. (1976). Frost creep and gelifluction features: A review. *Quaternary Research*, *6*(1), 55–76. https://doi.org/10.1016/0033-5894(76)90040-5

Bergh, S. G., & Andresen, A. (1985). Tectonometamorphic evolution of the allochthonous Caledonian rocks between Malangen and Balsfjord, Troms, north Norway. *Norges Geologiske Undersøkelse*, *401*(January), 1–34.

Bergh, S. G., Eig, K., Kløvjan, O. S., Henningsen, T., Olesen, O., & Hansen, J. A. (2007). The Lofoten-Vesterålen continental margin: A multiphase Mesozoic-Palaeogene rifted shelf as shown by offshore-onshore brittle fault-fracture analysis. *Norsk Geologisk Tidsskrift*, *87*(1–2), 29–58.

Böhme, M., Bunkholt, H. S. S., Oppikofer, T., Dehls, J. F., Hermanns, R. L., Eriksen, H., Lauknes, T. R., & Eiken, T. (2016). Using 2D InSAR, dGNSS and structural field data to understand the deformation mechanism of the unstable rock slope Gamanjunni 3, northern Norway. *Landslides and Engineered Slopes. Experience, Theory and Practice*, *2*(October 2017), 443–449. https://doi.org/10.1201/b21520-45

Böhme, M., Hermanns, R. L., Oppikofer, T., Fischer, L., Bunkholt, H. S. S., Eiken, T., Pedrazzini, A., Derron, M. H., Jaboyedoff, M., Blikra, L. H., & Nilsen, B. (2013). Analyzing complex rock slope deformation at Stampa, western Norway, by integrating geomorphology, kinematics and numerical modeling. *Engineering Geology*, *154*(February), 116–130. https://doi.org/10.1016/j.enggeo.2012.11.016

Braathen, A., Blikra, L. H., Berg, S. S., & Karlsen, F. (2004). Rock-slope failures in Norway; type, geometry, deformation mechanisms and stability. *Norsk Geologisk Tidsskrift*, *84*(1), 67–88.

Bunkholt, H., Nordahl, B., Hermanns, R. L., Oppikofer, T., Fischer, L., Blikra, L. H., Anda, E., Dahle, H., & Sætre, S. (2013a). Database of Unstable Rock Slopes of Norway. *Landslide Science and Practice*, *January*. https://doi.org/10.1007/978-3-642-31310-3

Bunkholt, H., Otterå, S., Yugsi Molina, F. X., Hermanns, R. L., Dehls, J., Osmundsen, P. T., Redfield, T., Eiken, T., & Böhme, M. (2013b). *Undersøkelser av ustabile fjellpartier i Troms – status og planer etter feltarbeid 2011 og 2012*. (NGU Rapport - 2013.021).

Norges geologiske undersøkelse. https://www.ngu.no/publikasjon/unders-kelser-av-ustabile-fjellpartier-i-troms-status-og-planer-etter-feltarbeid-2011-og

Bunkholt, H., Redfield, T., Osmundsen, P. T., Oppikofer, T., Hermanns, R. L., & Dehls, J. (2013c). The Role of Inherited Structures in Deep Seated Slope Failures in Kåfjorden, Norway. *Landslide Science and Practice, March 2016*. https://doi.org/10.1007/978-3-642-31325-7

Carter, M., & Bentley, S. P. (1985). The geometry of slip surfaces beneath landslides: predictions from surface measurements. *Canadian Geotechnical Journal*, *22*(2), 234-238.

Crippa, C., Valbuzzi, E., Frattini, P., Crosta, G. B., Spreafico, M. C., & Agliardi, F. (2021). Semi-automated regional classification of the style of activity of slow rock-slope deformations using PS InSAR and SqueeSAR velocity data. *Landslides, September 2020*. https://doi.org/10.1007/s10346-021-01654-0

Crosta, G. B., di Prisco, C., Frattini, P., Frigerio, G., Castellanza, R., & Agliardi, F. (2014). Chasing a complete understanding of the triggering mechanisms of a large rapidly evolving rockslide. Landslides, 11(5), 747–764. https://doi.org/10.1007/s10346-013-0433-1

Crosta, G. B., Frattini, P., & Agliardi, F. (2013). Deep seated gravitational slope deformations in the European Alps. *Tectonophysics*, *605*, 13–33. https://doi.org/10.1016/j.tecto.2013.04.028

Cruden, D. M., & Varnes, D. J. (1996). Landslide types and processes. *Turner AK, Schuster RL (Eds) Landslides Investigation and Mitigation. Transportation Research Board, US National Research Council. Special Report 247, January*, 36–75.

Dehls, J. F., Larsen, Y., Marinkovic, P., Lauknes, T. R., Stødle, D., & Moldestad, D. A. (2019). INSAR. No: A National Insar Deformation Mapping/Monitoring Service In Norway--From Concept To Operations. In *IGARSS 2019-2019 IEEE International Geoscience and Remote Sensing Symposium* (pp. 5461-5464). IEEE.

Dini, B., Daout, S., Manconi, A., & Loew, S. (2019a). Classification of slope processes based on multitemporal DInSAR analyses in the Himalaya of NW Bhutan. *Remote Sensing of Environment*, *233*(September), 111408. https://doi.org/10.1016/j.rse.2019.111408

Dini, B., Manconi, A., & Loew, S. (2019b). Investigation of slope instabilities in NW Bhutan as derived from systematic DInSAR analyses. *Engineering Geology*, *259*(May), 105111. https://doi.org/10.1016/j.enggeo.2019.04.008

Dyrrdal, A. V., Isaksen, K., Jacobsen, J. K., & Nilsen, I. B. (2020). Present and future changes in winter climate indices relevant for access disruptions in Troms, northern Norway. *Natural Hazards and Earth System Sciences*, *20*(6), 1847–1865. https://doi.org/10.5194/nhess-20-1847-2020

Eckerstorfer, M., Eriksen, H. Ø., Rouyet, L., Christiansen, H. H., Lauknes, T. R., & Blikra, L. H. (2018). Comparison of geomorphological field mapping and 2D-InSAR mapping of periglacial landscape activity at Nordnesfjellet, northern Norway. *Earth Surface Processes and Landforms*, *43*(10), 2147–2156. https://doi.org/10.1002/esp.4380

Eriksen, H. Ø. (2013). Slope displacement patterns observed using satellite InSAR data in the Storfjord-Kåfjord-Lyngen region, Troms, Master thesis, University of Tromsø, Tromsø, Norway. *Master Thesis, UiT-The Arctic University of Norway*, May, 138. http://hdl.handle.net/10037/5240Strozzi, T., Caduff, R., Jones, N., Barboux, C., Delaloye, R., Bodin, X., Kääb, A., Mätzler, E., & Schrott, L. (2020). Monitoring rock glacier kinematics with satellite synthetic aperture radar. *Remote Sensing*, *12*(3), 1–24. https://doi.org/10.3390/rs12030559

Eriksen, H. Ø. (2017). Combining Satellite and Terrestrial Interferometric Radar Data to Investigate Surface Displacement in the Storfjord and Kåfjord Area, Northern Norway.

PhD Dissertation, UiT-The Arctic University of Norway, April, 138. https://doi.org/http://hdl.handle.net/10037/5240

Eriksen, H. Ø., Lauknes, T. R., Larsen, Y., Corner, G. D., Bergh, S. G., Dehls, J., & Kierulf, H. P. (2017). Visualizing and interpreting surface displacement patterns on unstable slopes using multi-geometry satellite SAR interferometry (2D InSAR). *Remote Sensing of Environment*, *191*, 297–312. https://doi.org/10.1016/j.rse.2016.12.024

Eriksen, H., Rouyet, L., Lauknes, T. R., Berthling, I., Isaksen, K., Hindberg, H., Larsen, Y., & Corner, G. D. (2018). Recent Acceleration of a Rock Glacier Complex, Ádjet, Norway, Documented by 62 Years of Remote Sensing Observations. *Geophysical Research Letters*, *45*(16), 8314–8323. https://doi.org/10.1029/2018GL077605

Faber, C. (2017). Mountain building processes in the northern Norwegian Caledonides. *PhD Dissertation, UiT-The Arctic University of Norway*, *November*.

Farbrot, H., Isaksen, K., Etzelmüller, B., & Gisnås, K. (2013). Ground thermal regime and permafrost distribution under a changing climate in Northern Norway. *Permafrost and Periglacial Processes*, *24*(1), 20–38. https://doi.org/10.1002/ppp.1763

Ferretti, A. (2014). *Satellite InSAR data: reservoir monitoring from space*. EAGE publications.

Ferretti, A., Prati, C., & Rocca, F. (2001). Permanent scatterers in SAR interferometry. *IEEE Transactions on Geoscience and Remote Sensing*, *39*(1), 8–20. https://doi.org/10.1109/36.898661

Fossen, H., & Gabrielsen, R. H. (2005). *Strukturgeologi*. Fagbokforlaget.

Frattini, P., Crosta, G. B., Rossini, M., & Allievi, J. (2018). Activity and kinematic behaviour of deep-seated landslides from PS-InSAR displacement rate measurements. *Landslides*, *15*(6), 1053–1070. https://doi.org/10.1007/s10346-017-0940-6

French, H. M. (2007). *The Periglacial Environment* (third edition). John Willey & Sons. https://doi.org/10.2307/1550550

Gischig, V., Amann, F., Moore, J. R., Loew, S., Eisenbeiss, H., & Stempfhuber, W. (2011). Composite rock slope kinematics at the current Randa instability, Switzerland, based on remote sensing and numerical modeling. *Engineering Geology*, *118*(1–2), 37–53. https://doi.org/10.1016/j.enggeo.2010.11.006

Gisnås, K., Etzelmüller, B., Lussana, C., Hjort, J., Sannel, A. B. K., Isaksen, K., Westermann, S., Kuhry, P., Christiansen, H. H., Frampton, A., & Åkerman, J. (2017). Permafrost Map for Norway, Sweden and Finland. *Permafrost and Periglacial Processes*, *28*(2), 359–378. https://doi.org/10.1002/ppp.1922

Grahn, J., Lauknes, T. R., Larsen, Y., & Rouyet, L. (2019). *Algorithmic consolidation report*. NORCE report, Mapping and characterization of unstable slopes withSentinel-1 multi-geometry InSAR, 4000125274/18/I-NB. Norwegian Research Centre.

Haeberli, W., Hallet, B., Arenson, L., Elconin, R., Humlum, O., Kääb, A., Kaufmann, V., Ladanyi, B., Matsuoka, N., Springman, S., & Muhll, D. (2006). Remote sensing of rermafrost-related problems and hazards. *Permafrost and Periglacial Processes*, *136*(January), 107–136. https://doi.org/10.1002/ppp

Harris, C., Kern-Luetschg, M., Christiansen, H. H., & Smith, F. (2011). The Role of Interannual Climate Variability in Controlling Solifluction Processes, Endalen, Svalbard. *Permafrost and Periglacial Processes*, *22*(3), 239–253. https://doi.org/10.1002/ppp.727

Harris, C., Kern-Luetschg, M., Fraser, S., & Isaksen, K. (2008). Solifluction Processes in an Area of Seasonal Ground Freezing, Dovrefjell, Norway. *Permafrost and Periglacial Processes*, *136*(January), 107–136. https://doi.org/10.1002/ppp

Henderson, I. H. C., Lauknes, T. R., Osmundsen, P. T., Dehls, J., Larsen, Y., & Redfield, T. F. (2011). A structural, geomorphological and InSAR study of an active rock slope failure development. *Geological Society, London, Special Publication*, *351*, 185–199. https://doi.org/10.1144/SP351.10

Henderson, I. H. C., Osmundsen, P. T., & Redfield, T. (2007). *ROS Fjellskred i Troms: Statusrapport 2007*. (NGU Rapport - 2008.025). https://www.ngu.no/publikasjon/ros-fjellskred-i-troms-statusrapport-2007

Hermanns, R. L., & Longva, O. (2012). Rapid rock-slope failures. *Landslides: Types, Mechanisms and Modeling*, *December 2015*, 59–70. https://doi.org/10.1017/cbo9780511740367.007

Hermanns, R. L., Blikra, L. H., Anda, E., Saintot, A., Dahle, H., Oppikofer, T., Fischer, L., Bunkholt, H., Dehls, J. F., Lauknes, T. R., & Redfield, T. F. (2013). Systematic Mapping of Large Unstable Rock Slopes in Norway. *Landslide Science and Practice*, *August 2015*. https://doi.org/10.1007/978-3-642-31325-7

Hermanns, R. L., Oppikofer, T., Anda, E., Blikra, L. H., Böhme, M., Bunkholt, H., Crosta, G. B., Dahle, H., Devoli, G., Fischer, L., Jaboyedoff, M., Loew, S., Sætre, S., & Molina, F. X. Y. (2012). *Recommended hazard and risk classification system for large unstable rock slopes in Norway* (NGU Rapport - 2012.029). http://www.ngu.no/no/hm/Publikasjoner/Rapporter/2012/2012-029/

Hermanns, R. L., Schleier, M., Böhme, M., Blikra, L. H., Gosse, J., Ivy-ochs, S., & Hilger, P. (2017). Rock-Avalanche Activity in W and S Norway Peaks After the Retreat of the Scandinavian Ice Sheet. *Advancing Culture of Living with Landslides*, *October*. https://doi.org/10.1007/978-3-319-53483-1

Hestad, H. W. (2019). Oppdatert kartlegging av permafrostrelaterte landformer i Troms, Nord-Norge , ved bruk av NGU InSAR. *Maser Thesis, UiO*, 1–20.

Hjort, J., Ujanen, J., Parviainen, M., Tolgensbakk, J., & Etzelmüller, B. (2014). Transferability of geomorphological distribution models: Evaluation using solifluction features in subarctic and Arctic regions. *Geomorphology*, *204*, 165–176. https://doi.org/10.1016/j.geomorph.2013.08.002

Hughes, A. L. C., Gyllencreutz, R., Lohne, Ø. S., Mangerud, J., & Svendsen, J. I. (2016). The last Eurasian ice sheets - a chronological database and time-slice reconstruction, DATED-1. *Boreas*, *45*(1), 1–45. https://doi.org/10.1111/bor.12142

Humlum, O. (1998). The climatic significance of rock glaciers. *Permafrost and Periglacial Processes*, *9*(4), 375–395. https://doi.org/10.1002/(SICI)1099-1530(199810/12)9:4<375::AID-PPP301>3.0.CO;2-0

Hungr, O., Leroueil, S., & Picarelli, L. (2014). The Varnes classification of landslide types, an update. *Landslides*, *11*(2), 167–194. https://doi.org/10.1007/s10346-013-0436-y

Imaizumi, F., Nishiguchi, T., Matsuoka, N., Trappmann, D., & Stoffel, M. (2018). Interpretation of recent alpine landscape system evolution using geomorphic mapping and L-band InSAR analyses. *Geomorphology*, *310*, 125–137. https://doi.org/10.1016/j.geomorph.2018.03.013

Indrevær, K., & Bergh, S. G. (2014). Linking onshore-offshore basement rock architecture and brittle faults on the submerged strandflat along the SW Barents Sea margin, using high-resolution (5 × 5 m) bathymetry data. *Norsk Geologisk Tidsskrift*, *94*(1), 1–34.

Intrieri, E., Frodella, W., Raspini, F., Bardi, F., & Tofani, V. (2020). Using satellite interferometry to infer landslide sliding surface depth and geometry. *Remote Sensing*, *12*(9). https://doi.org/10.3390/RS12091462

IPA. (2020). Towards standard guidelines for inventorying rock glaciers, Baseline concepts, Version 4.1. IPA Action Group Rock glacier inventories and kinematics, https://www3.unifr.ch/geo/geomorphology/en/research/ipa-action-group-rock-glacier/

Jones, D. B., Harrison, S., Anderson, K., & Whalley, W. B. (2019). Rock glaciers and mountain hydrology: A review. *Earth-Science Reviews*, *193*(October 2018), 66–90. https://doi.org/10.1016/j.earscirev.2019.04.001

Kääb, A. (2005). Remote Sensing of Mountain Glaciers and Permafrost Creep. *Geograph. Inst. d. Univ.*, *48*, 266. http://scholar.google.com/scholar?hl=en&btnG=Search&q=intitle:Remote+Sensing+of+Mountain+Glaciers+and+Permafrost+Creep#0

Kääb, A., & Weber, M. (2004). Development of transverse ridges on rock glaciers: Field measurements and laboratory experiments. *Permafrost and Periglacial Processes*, *15*(4), 379–391. https://doi.org/10.1002/ppp.506

Kääb, A., Frauenfelder, R., & Roer, I. (2007). On the response of rock glacier creep to surface temperature increase. *Global and Planetary Change*, *56*(1–2), 172–187. https://doi.org/10.1016/j.gloplacha.2006.07.005

Lauknes, T. R. (2010). Rockslide Mapping in Norway by Means of Interferometric SAR Time Series Analysis. *PhD Dissertation, University of Tromsø, December*, 124 pages. internal-pdf://217.109.5.182/thesisTRL2010.pdf

Lauknes, T. R., Piyush Shanker, A., Dehls, J. F., Zebker, H. A., Henderson, I. H. C., & Larsen, Y. (2010). Detailed rockslide mapping in northern Norway with small baseline and persistent scatterer interferometric SAR time series methods. *Remote Sensing of Environment*, *114*(9), 2097–2109. https://doi.org/10.1016/j.rse.2010.04.015

Lilleøren, K. S., & Etzelmüller, B. (2011). A regional inventory of rock glaciers and ice-cored moraines in Norway. *Geografiska Annaler: Series A, Physical Geography*, *93*(3), 175–191. https://doi.org/10.1111/j.1468-0459.2011.00430.x

Liu, L., Millar, C. I., Westfall, R. D., & Zebker, H. A. (2013). Surface motion of active rock glaciers in the Sierra Nevada, California, USA: Inventory and a case study using InSAR. *Cryosphere*, *7*(4), 1109–1119. https://doi.org/10.5194/tc-7-1109-2013

Magnin, F., Etzelmüller, B., Westermann, S., Isaksen, K., Hilger, P., & Hermanns, R. L. (2019). Permafrost distribution in steep slopes in Norway: measurements, statistical modelling and geomorphological implication. *Earth Surface Dynamics*, 1–35. https://doi.org/10.5194/esurf-2018-90

Massonnet, D., Rossi, M., Carmona, C., Adragna, F., Peltzer, G., Feigl, K., & Rabaute, T. (1993). The displacement field of the Landers earthquake mapped by radar interferometry. *Nature*, *364*(6433), 138–142. https://doi.org/10.1038/364138a0

Matsuoka, N. (2001). Solifluction rates, processes and landforms: a global review. *Earth-Science Reviews*, *55*, 107–134.

Meteorologisk Institutt, Norges vassdrags- og energidirektorat NVE, Norwegian Research Center AS NORCE, and Bjerknes Center for Climate Research. (2021). *Norsk Klimaservicesenter. Norwegian Climate Service Center.* Retrieved November 2020 from https://seklima.met.no/observations/

NGU. (2020a). *Unstable Rock Slopes – National Database for Unstable Rock Slopes*. Norges Geologiske Undersøkelser www.ngu.no. Retrieved September 2020 from https://geo.ngu.no/kart/ustabilefjellparti_mobil/?lang=eng

NGU. (2020b). *Bedrock – National bedrock database, Bedrock N250*. Norges Geologiske Undersøkelser www.ngu.no. Retrieved November 2020 from https://geo.ngu.no/kart/berggrunn_mobil/

NGU. (2020c). *Superficial deposits – National database*. Norges Geologiske Undersøkelser www.ngu.no. Retrieved November 2020 from http://geo.ngu.no/kart/losmasse_mobil/?lang=eng

NGU. (2020d). *About the Mapping Service – InSAR Norge*. Norges Geologiske Undersøkelse www.ngu.no. Retrieved from https://www.ngu.no/en/topic/about-mapping-service

NMA. (2020a). *Topografisk Norgeskart 4 WMS*. Norwegian Mapping Authority. Retrieved September 2020 from https://kartkatalog.geonorge.no/

NMA. (2020b). *DTM 1, 10 & 50 m Terrengmodell (UTM33).* Norwegian Mapping Authority. Retrieved September 2020 from https://hoydedata.no/LaserInnsyn/

NMA. (2020c). *Norge I Bilder WMS (Euref89 UTM33), Troms 2016 and Troms 2006*. Norwegian Mapping Authority. Retrieved September 2020 from https://www.norgeibilder.no/

Pánek, T., & Klimeš, J. (2016). Temporal behavior of deep-seated gravitational slope deformations: A review. *Earth-Science Reviews*, *156*, 14–38. https://doi.org/10.1016/j.earscirev.2016.02.007

Park, H. J., Lee, J. H., Kim, K. M., & Um, J. G. (2016). Assessment of rock slope stability using GIS-based probabilistic kinematic analysis. *Engineering Geology*, *203*, 56–69. https://doi.org/10.1016/j.enggeo.2015.08.021

Ramberg, I. B., Bryhni, I., & Nøttvedt, A. (2007). Landet blir til: Norges geologi. *Norsk geologisk forening*.

Rasmussen, E. (2011). Fjellskred i Laksvatnfjellet, Balsfjord, Troms: indre struktur, morfologi og skredmekanismer, Master Thesis, UiT-The Arctic University of Norway, Tromsø, Norway, (in norwegian). *Master Thesis, UiT-The Arctic University of Norway*, 142.

Rocscience. (2021). *Dips Tutorials*. Rocscience.com. Retrieved January 2021 from https://www.rocscience.com/help/dips/tutorials/dips_tutorials.htm

Rouyet, L., Lilleøren, K., Böhme M., Delaloye, R., Vick, L., Larsen, Y., Lauknes, T. R., Etzelmüller, B., & Blikra, L. H. (under review). Regional InSAR inventory of slope movement in Lyngen-Kåfjord area, Northern Norway. *Frontier in Earth Science: Cryospheric Sciences.*

Rouyet, L., Lilleøren, K., Böhme, M., Vick, L. M., Delaloye, R., Etzelmüller, B.,; Lauknes, T. R., Larsen, Y., Blikra, L. H. (2021): Kinematic and morphological inventories of slope movement in Northern Norway. *PANGAEA*, https://doi.pangaea.de/10.1594/PANGAEA.930856 (DOI registration in progress)

Rouyet, L., Lauknes, T. R., Christiansen, H. H., Strand, S. M., & Larsen, Y. (2019). Seasonal dynamics of a permafrost landscape, Adventdalen, Svalbard, investigated by InSAR. *Remote Sensing of Environment*, *231*(June), 111236. https://doi.org/10.1016/j.rse.2019.111236

Rouyet, L., Lauknes, T. R., Høgda, K. A. (2015). *Satellittbasert radarinterferometri (InSAR) for naturfare, skred og infrastruktur*. https://nve.brage.unit.no/nve-xmlui/handle/11250/2498497

Samsonov, S., Dille, A., Dewitte, O., Kervyn, F., & d'Oreye, N. (2020). Satellite interferometry for mapping surface deformation time series in one, two and three dimensions: A new method illustrated on a slow-moving landslide. *Engineering Geology*, *266*(December 2019), 105471. https://doi.org/10.1016/j.enggeo.2019.105471

Sattler, K., Anderson, B., Mackintosh, A., Norton, K., & de Róiste, M. (2016). Estimating permafrost distribution in the maritime southern alps, New Zealand, based on climatic conditions at rock glacier sites. *Frontiers in Earth Science*, *4*(February), 1–17. https://doi.org/10.3389/feart.2016.00004

Setså, K. (2021, 19. January). *Satellittdata avslører nye skredtrusler*. Geoforskning. https://www.geoforskning.no/nyheter/geofarer/2438-satellittdata-avslorer-nye-skredtrusler

Shur, Y., Hinkel, K. M., & Nelson, F. E. (2005). The transient layer: Implications for geocryology and climate-change science. *Permafrost and Periglacial Processes*, *16*(1), 5–17. https://doi.org/10.1002/ppp.518

Singh, V., Singh, P., & Haritashya, U. K. (2011). Encyclopedia of Snow, Ice and Glaciers. In *Encyclopedia of Earth Sciences Series*.

Songbo, W. U., Yongyao, L. E., Lei, Z., & Xiaoli, D. (2020). Multi-temporal InSAR for Urban Deformation Monitoring : *Journal of Radars*, *9*. https://doi.org/10.12000/JR20037.Document

SSB. (2020). *04317: Befolkning, etter grunnkrets, statistikkvariabler og år: Sjøvassbotn (54013305) og Lakselvbukt (54013303)*. Statistisk sentralbyrå. Retrieved October 2020 from https://www.ssb.no/statbank/table/04317/tableViewLayout1/

Stead, D., & Eberhardt, E. (2013). Understanding the mechanics of large landslides. *Italian Journal of Engineering Geology and Environ*, *6*, 245–254. https://doi.org/10.4408/IJEGE.2013-06.B-07

Stead, D., & Wolter, A. (2015). A critical review of rock slope failure mechanisms: The importance of structural geology. *Journal of Structural Geology*, *74*(October), 1–23. https://doi.org/10.1016/j.jsg.2015.02.002

Stead, D., Eberhardt, E., & Coggan, J. S. (2005). Developments in the characterization of complex rock slope deformation and failure using numerical modelling techniques. *Engineering Geology*, *83*(1–3), 217–235. https://doi.org/10.1016/j.enggeo.2005.06.033

Strozzi, T., Farina, P., Corsini, A., Ambrosi, C., Thüring, M., Zilger, J., Wiesmann, A., Wegmüller, U., & Werner, C. (2005). Survey and monitoring of landslide displacements by means of L-band satellite SAR interferometry. *Landslides*, *2*(3), 193–201. https://doi.org/10.1007/s10346-005-0003-2

Strozzi, T., Caduff, R., Jones, N., Barboux, C., Delaloye, R., Bodin, X., Kääb, A., Mätzler, E., & Schrott, L. (2020). Monitoring rock glacier kinematics with satellite synthetic aperture radar. *Remote Sensing*, *12*(3), 1–24. https://doi.org/10.3390/rs12030559

Vick, L. M., Böhme, M., Rouyet, L., Bergh, S. G., Corner, G. D., & Lauknes, T. R. (2020). Structurally controlled rock slope deformation in northern Norway. *Landslides*, *17*(8), 1745–1776. https://doi.org/10.1007/s10346-020-01421-7

Wang, X., Liu, L., Zhao, L., Wu, T., Li, Z., & Liu, G. (2017). Mapping and inventorying active rock glaciers in the northern Tien Shan of China using satellite SAR interferometry. *Cryosphere*, *11*(2), 997–1014. https://doi.org/10.5194/tc-11-997-2017

Wright, T. J., Parsons, B. E., & Lu, Z. (2004). Toward mapping surface deformation in three dimensions using InSAR. *Geophysical Research Letters*, *31*(1). https://doi.org/10.1029/2003GL018827

Wyllie, D. C., & Mah, C. W. (2004). Rock slope engineering: Civil and mining, 4th edition. In *CRP Press*. https://doi.org/10.1201/9781315274980

Zangerl, C., Fey, C., & Prager, C. (2019). Deformation characteristics and multi-slab formation of a deep-seated rock slide in a high alpine environment (Bliggspitze, Austria). *Bulletin of Engineering Geology and the Environment*, *78*(8), 6111–6130. https://doi.org/10.1007/s10064-019-01516-z

Zhang, X. P., Wong, L. N. Y., Wang, S. J., & Han, G. Y. (2011). Engineering properties of quartz mica schist. *Engineering Geology*, *121*(3–4), 135–149. https://doi.org/10.1016/j.enggeo.2011.04.020

Appendix

Appendix 1: Data resources applied in the thesis.

External data resources	Resolution	Source
Digital elevation models (DEM)	1 m, 10 m, and 50 m	www.hoydedata.no
Orthophoto imagery 2016 and 2006	0,25 m and 0,5 m	www.norgeibilder.no
Satellite images world imagery		Esri /Arc map online
Aerial images		NGU
Geological map	1:250 000	Bedrock (ngu.no)
Quaternary map	1:250 000	Superficial deposits (ngu.no)
InSAR displacement information		InSAR Norway (ngu.no)
Structural measurements		NGU Geo-3135 2020 course
RSD inventory Norway		Unstable Rock Slopes (ngu.no)
Inventory periglacial landforms Troms		

Appendix2: Software's utilized in the thesis.

Software for Geographically Projection	ArcMap (10.6.1)	WGS 1984 UTM Zone 33 & ETRS 1989 UTM Zone 33
	ArcGIS Pro	
	Dips 8 Rocscience	
Software for creating illustrations	Corel draw technical suit 2017	
	Inkscape 1.0	

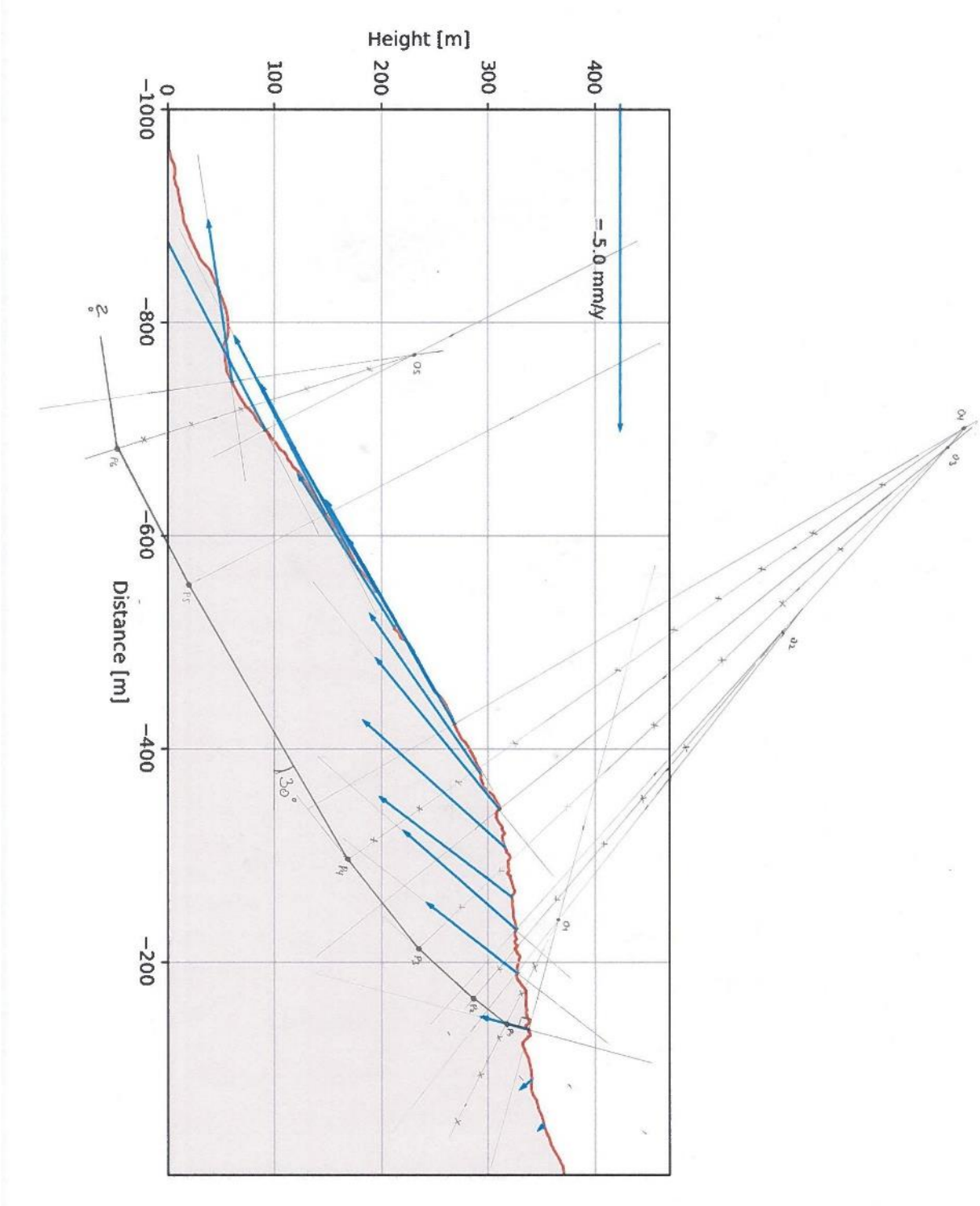

Appendix 3: Geometry of the basal rupture surface interpreted with the graphical Vector Inclination Method on Njunnás.

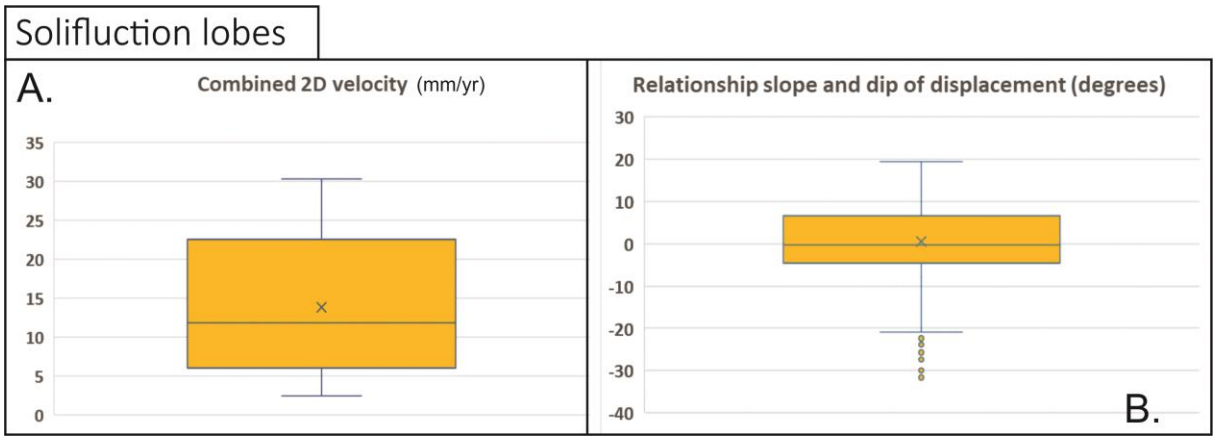

Appendix 4: Combined 2D velocity in mapped solifluction lobes (A.) and relationship between slope inclination and dip of displacement in solifluction (B.). Data from Piggtind/Skulvatindane.

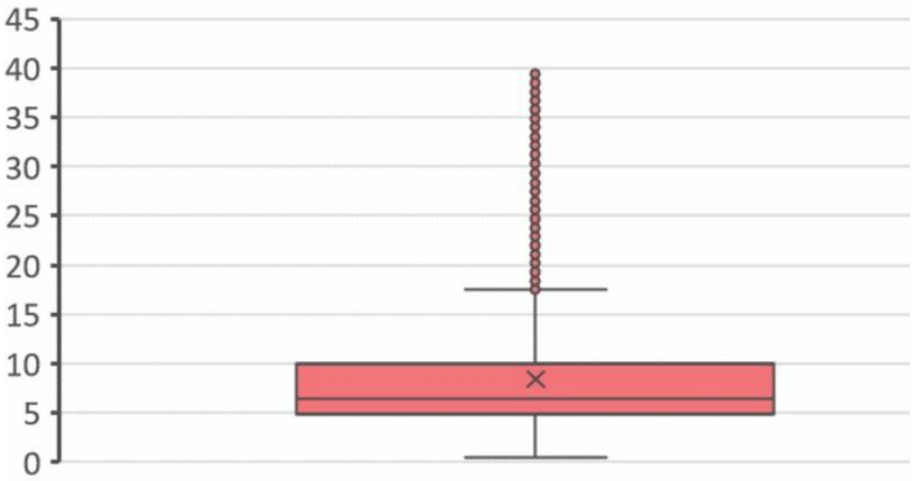

Appendix 5: Boxplots showing the combined 2D velocities in the disaggregated unit on Piggtind/Skulvatindane (n=19383)

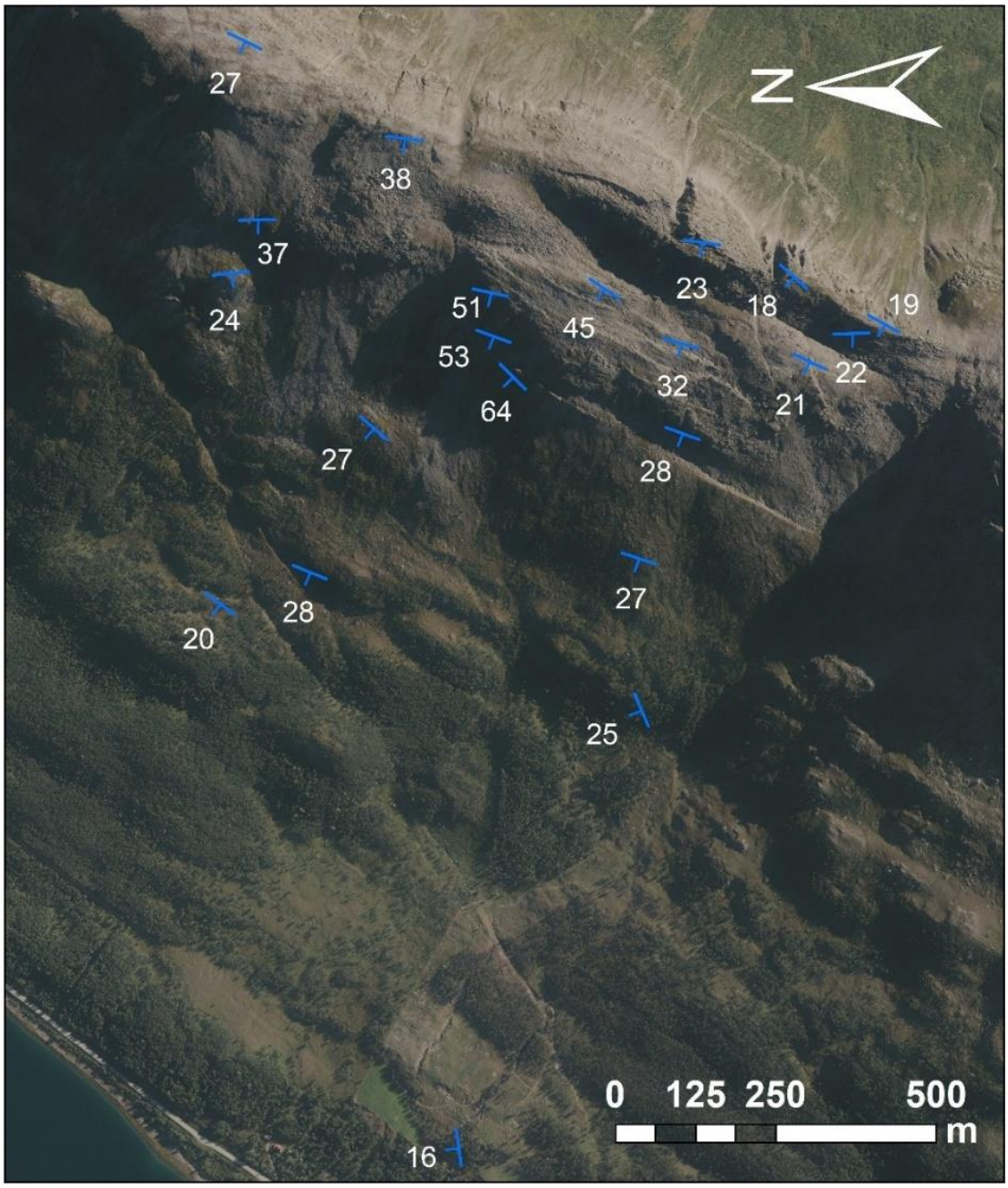

Appendix 6: Orientation measurements of foliation on Lakselvnesåsen. The figure displays the average dip and dip direction for each locality.

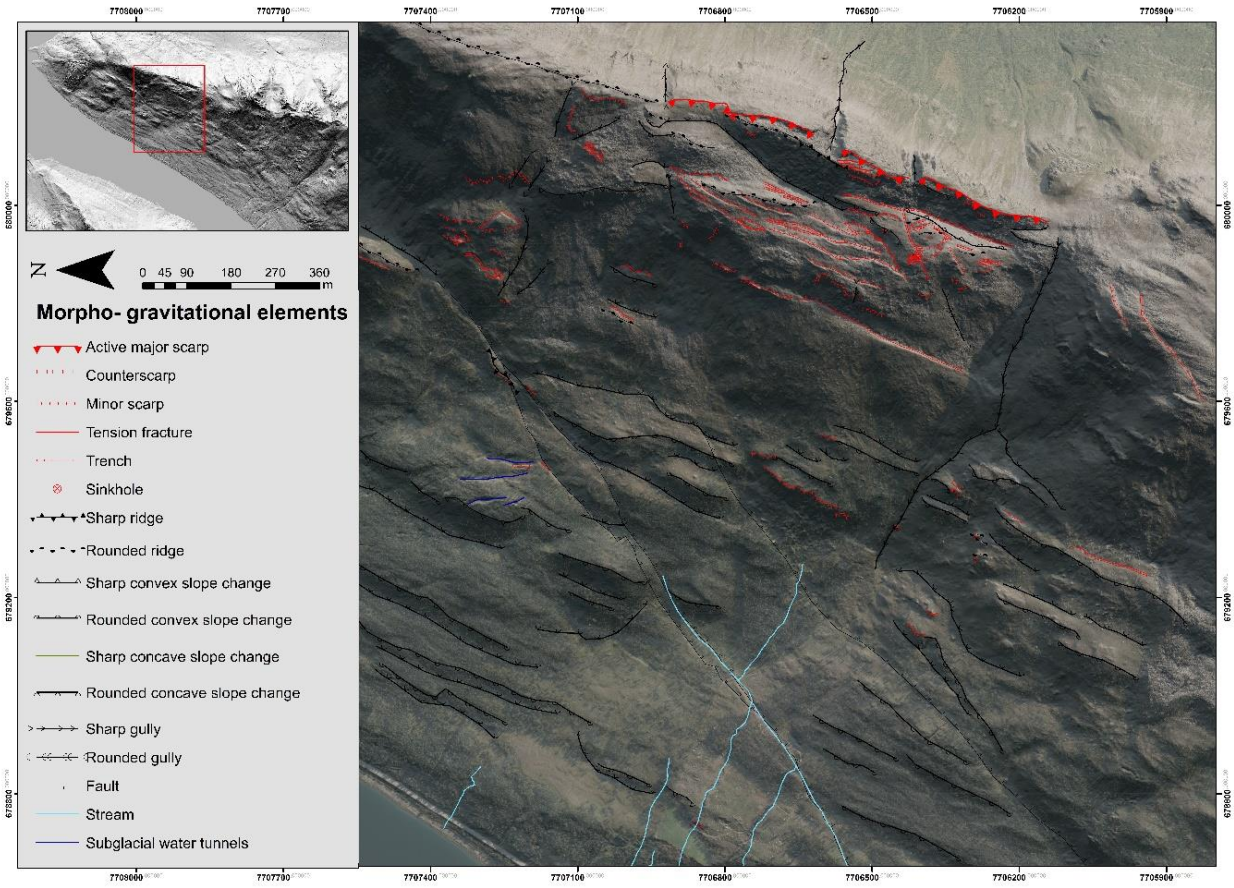

Appendix 7: Mapped morpho-gravitational structures on Lakselvnesåsen.

Table of Figures

Chapter 2: Theoretical background

Chapter 3: Study area

Chapter 4: Data and methods

Chapter 5: Results and interpretation Njunnás

Chapter 6: Results and interpretation Piggtind/Skulvatindane

Chapter 7: Synthesis and discussion